On Improvement of Frequency Stability of Power System with Grid Following Converters

A thesis submitted

in partial fulfillment for the award of the degree of

Doctor of Philosophy

by

Rachakonda Shri Rama Akshay

SC18D028

Department of Avionics

Indian Institute of Space Science and Technology

Thiruvananthapuram, India

December 2023

Certificate

This is to certify that the thesis titled ***On Improvement of Frequency Stability of Power System with Grid Following Converters*** submitted by **Rachakonda Shri Rama Akshay**, to the Indian Institute of Space Science and Technology, Thiruvananthapuram, in partial fulfillment for the award of the degree of **Doctor of Philosophy** in **Power System Stability Control**, is a bonafide record of the original work carried out by him under my supervision. The contents of this report, in full or in parts, have not been submitted to any other Institute or University for the award of any degree or diploma.

Dr. Rajesh Joseph Abraham
Associate Professor
Dept. of Avionics

Dr. N.Selvaganesan
Professor and Head
Dept. of Avionics

Place: Thiruvananthapuram
Date: 2023

Declaration

I declare that this thesis titled ***On Improvement of Frequency Stability of Power System with Grid Following Converters*** submitted in partial fulfillment for the award of the degree of **Doctor of Philosophy** is a record of the original work carried out by me under the supervision of Dr. **Rajesh Joseph Abraham**, and has not formed the basis for the award of any degree, diploma, associateship, fellowship, or other titles in this or any other Institution or University of higher learning. In keeping with the ethical practice in reporting scientific information, due acknowledgments have been made wherever the findings of others have been cited.

Place: Thiruvananthapuram
Date: December 2023

Rachakonda Shri Rama Akshay
(SC18D028)

This thesis is dedicated to my parents . . .

Acknowledgements

For their unconditional love, support, and motivation throughout my life, I owe my deepest gratitude to my parents R. Sai Prasad and R. Jai Laxmi. I would also express my appreciation to my brother, R. Shridhar for taking the responsibility of our family in my absence and also my sister-in-law R. Akanksha, and nephew R. Hridhaan. I am extremely thankful to my Ph.D. supervisor Dr. Rajesh Joseph Abraham, for the guidance, moral support and encouragement that I received from him during this Ph.D. programme as his student. I am very lucky to have him as my mentor, and as a guide, without his support this work wouldn't have possible. I express my gratitude to Dr. R. Sudharshan Kaarthik, Dr. Anindya Dasgupta, Dr. Rajeevan P.P, Dr. Chris Prema, Dr. E. Natarajan, the members of my doctoral committee for their continuous assessment in the progress of this work. I am indebted to Dr. Harsha Simha for his mentorship and guidance. I'd like to express my deepest gratitude to Dr. B.S. Manoj, Head of the Avionics department [2017-2020], who welcomed me into the PhD program and provided invaluable guidance during its early stages. My sincere thanks to Dr. Deepak Mishra, HoD, [2020-2022] who played crucial role in encouraging and supporting the research work. I'm incredibly indebted to Dr. N. Selvaganesan, HoD of Avionics, at present, for their insightful suggestions and support in the revision and submission stage of the thesis.

I am extremely fortunate for the stimulating fellowship I received from my colleagues, particularly Mr. Jyotirmoy Dey, Mr. P. Guru Krishna, Mr. Pramod Martha, Mr. Avinash Ch., Mr. Debabrata D. fellow researchers of Department of Astronomy and Astrophysics, Department of Avionics. I acknowledge the invariable support from the M.Tech students and the office staff especially Ms. Archana Sanal and Abhilash. I would like to thank the Department of Space, Government of India, for not only providing the financial support and the research facilities to undertake this work, but also giving me the opportunity to attend the conferences to meet motivating people.

Rachakonda Shri Rama Akshay

Abstract

The fundamental advantage of electrical energy over other forms of energy is its ability to transmit and distribute over a large system instantly. The demand for electrical energy varies dynamically in the vast system. The ever-changing demand leads to an imbalance between generation and demand. The system frequency deviates from its nominal operating point with the imbalance between power demand and generation. The ancillary service that maintains the equilibrium between the load demand and power generation is known as Load Frequency Control (LFC). The power plants with high ramp rate such as the gas turbine power plants and the hydro power plants have been assigned for LFC, while, the low ramp rate power plants have shared base loads and do not participate in LFC. With development of semiconductor based power switches, power converters have been used to interface energy sources such as Solar PV, Battery Energy Storage System, Super Magnetic Energy Storage, etc. to the grid. In an interconnected system, the control areas are linked through tie lines. LFC of a control area has to adjust the generation of its own control area and neighbouring control areas while maintaining the generation of each power plant at optimal economic value. Automatic Generation Control (AGC) accomplishes these objectives through minimizing the Area Control Error.

This thesis aims to investigate AGC in a conventional regulated power system and a deregulated power system with the integration of Solar PV, Battery Energy Storage System (BESS), Super magnetic Energy Storage (SMES) and Static Synchronous Compensator (STATCOM). The linear time invariant models of Solar PV, BESS, SMES and STATCOM have been implemented in a two area power system for improving transient stability of the system. The average switching models of the active and reactive power devices have been presented to highlight the output current and power dynamics of the devices. A non linear model of the power system is considered with 10 % p.u. MW/s Generation Rate Constraint (GRC). With the availability of the active and reactive power compensation devices, the study extends to the optimal location and sizing of the devices which has not been attempted so far. The major area of interest for LFC is the application of the recently developed algorithm and its performance comparison. The area controller gains have been optimized using

Genetic Algorithm (GA) to show improvement in the frequency and tie line power profile with the addition of the STATCOM, SMES, BESS and solar PV.
The improved line loadings and Bus voltages by optimal sizing and location of active and reactive power devices have been reported for IEEE sample systems i.e. IEEE 9-Bus and IEEE 57-Bus systems. The objective of optimal sizing of the active and the reactive power compensating devices is to maintain the line overloadings and the Bus voltages within the nominal range during line outages and provide power security.

Contents

List of Figures

List of Tables

Abbreviations

ACE	Area Control Error
AGC	Automatic Generation Control
DFIG	Doubly Fed Induction Generator
LFC	Load Frequency Control
PFC	Primary Frequency Control
FACTS	Flexible AC Transmission System
RoCoF	Rate of Change of Frequency
SMES	Super Magnetic Energy Storage
BESS	Battery Energy Storage System
PV	Photovoltaic
STATCOM	Static Synchronous Compensator
SVC	Static VAR Compensator
GENCO	Generation Company
TRANSCO	Transmission Company
DISCO	Distribution Company
ISO	Independent System Operator
DPM	DISCO Participation Matrix
cpf	Contract Participation Factor
apf	Area Participation Factor
SSSC	Static Series Compensator
TCSC	Thyristor Controlled Series Compensator
TCPS	Thyristor Controlled Phase Shifter
GA	Genetic Algorithm
PSO	Particle Swarm Optimization
GSA	Gravitational Search Algorithm
CSA	Crow Search Algorithm
PID	Proportional Integral Derivative

LQR	Linear Quadratic Regulator
ISE	Integral Square Error
HVDC	High Voltage DC
VSC	Voltage Source Converter
GTO	Gate Turn Off Thyristor
PWM	Pulse Width Modulation

Nomenclature

f	nominal frequency (Hz)
Δf	Frequency deviations (Hz)
B_i	Area Frequency Bias factor ($p.u.MW/Hz$)
R_i	Governor speed regulation($Hz/p.u.MW$)
T_g	Time constant of Governor (sec)
T_{RHi}	Reheat turbine time constants (sec)
K_p	Power system Gain
T_p	Power system time constant (sec)
T_{12}	Synchronizing coefficient ($p.u.MW/rad$)
a_{12}	Area size ratio
apf_i	Area Participation Factor
ΔP_{Ti}	Turbine power output deviations ($p.u.MW$)
ΔP_{Gi}	Deviations in power generated ($p.u.MW$)
P_{RHi}	Reheat power input deviations ($p.u.MW$)
ΔP_{Di}	Power Disturbance ($p.u.MW$)
$\Delta P_{Tie_{12}}$	Tie line Power Deviation ($p.u.MW$)
K_{SMES}	SMES gain
K_{PV}	Solar PV gain
K_{BESS}	BESS gain
$K_{STATCOM}$	STATCOM gain
T_{SMES}	SMES time constant
T_{BESS}	BESS time constant
T_{PV}	Solar PV time constant
$T_{STATCOM}$	STATCOM time constant

Chapter 1

Introduction

Electrical power finds applications in modern-day industries, communications, automobiles, healthcare, and entertainment. The bulk of this power can be generated, transmitted, and controlled with higher reliability in the form of electrical energy. Power system comprises a network of generators, transmission lines/cables, protection devices (fuses, relays, circuit breakers), metering devices, and loads. The networks are interconnected to improve the economy of electric power transfer and secure power delivery to the loads. The interconnected network results in an extensive power system complex to design, operate and control.

International Energy Agency predicts that electrical energy share in the total energy consumption will increase to 24 % by 2040 [10]. This growing consumption, challenges the power system to use the available infrastructure and operate within stable margins economically. Power system stability is defined as the ability of the power system to regain the state of operating equilibrium with most of the system variables bounded when subjected to physical disturbances [1]. Power system stability is classified by the critical phenomena that drives the power system to instability. Power system stability is classified as rotor angle stability, voltage stability, frequency stability, resonance stability, and converter-driven stability. The control actions taken for achieving stability follow control hierarchy based on the timescale of the various phenomena. The electromagnetic phenomena have faster dynamics than the electromechanical dynamics. Thus, the small disturbances in voltage and current affects the rotor dynamics for a brief period and settle down before the disturbance affects the rotor. However, small disturbances in the rotor impacts the electromagnetic phenomena. A hierarchy of control based on timescale is presented in Fig. 1.1. The stability studies can be segregated based on timescale of the impact of the control dynamics. The synchronous machine ability to restore the synchronism

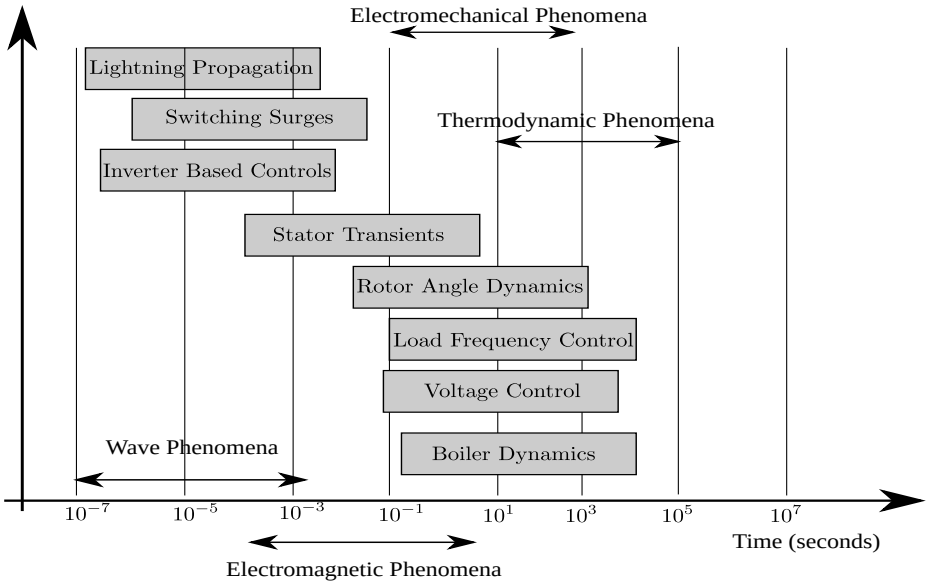

Figure 1.1: Timescale of various phenomena in power system [1]

after a small or large disturbance is termed as rotor angle stability [11]. The voltage stability is defined as the ability to maintain the steady-state voltage at the nominal voltage after a disturbance [11]. Resonance is a phenomenon that occurs due to the periodic exchange of energy in an oscillatory manner [1]. Due to insufficient damping, the magnitude of the physical quantities (voltage, current, torque) may increase beyond the stable margin. The converter-driven stability is classified based on converter dynamics interacting with the power system elements. Instability due to resonance induced between passive network elements and fast inner control loops of converter classified as fast interaction converter driven instability, while the interaction between slow control loops (power, voltage, phase lock loop) and other system components at low frequency is classified as Slow interaction converter driven instability.

Frequency control is becoming more critical with restructuring of the power system. Diverse energy sources like Wind energy sources, Solar PV, Energy Storages etc. are being integrated into the power system and the changes in the power system structure from conventional to deregulated results in changes in the coordinated control of generation and transmission. Few published research considers the uncertain power demand [12] and practical control structure that can be implemented in real-time for frequency control [13]. Also, applying modern control strategies may have difficulties in implementing them in existing aging power system. The inability of the

power system to regulate frequency within the specified limits is termed frequency instability [14]. The known frequency control methods are usually based on tuning control parameters either using classical methods or from experience gained from trial and error. These methods cannot provide desired performance due to changes in operating conditions. The frequency control is dependent on the active power control at the generating and the transmission side of the utility. As the change in active power demand is compensated by the conventional sources and the renewable energy sources in tandem, a control must be implemented to allocate the demand to the conventional and renewable energy sources. In addition to the frequency control, the tie-line power schedule of the interconnected areas is also to be maintained. The common term used for such control is Load Frequency Control.

1.1 Load Frequency Control

According to the Indian Electricity Grid Code (IEGC) [15], a control area is a territory bounded by interconnections (tie lines) with other control areas. Each site controls its generation and load to maintain its interchange schedule with other control areas and contributes to frequency regulation of the synchronously operating system [16]. For stable and good power quality, the load demand must match the power generation. The generation and load demand imbalance results in significant frequency deviations that degrade power plant auxiliaries performance as they require constant speed drives such as feed water pump, fuel pump, and combustion air pump. At the transmission and distribution level, high magnetizing currents are demanded by transformers and induction motors for significant frequency deviations [17]. Severe frequency deviations lead to cascaded tripping of frequency relays and, subsequently, an unstable condition for the power grid [18].
From the historical blackouts for example, the North East American blackout (November 8, 1965) [19]; South Australian blackout (2016) [20]; the Sweden-Denmark blackout (September 23, 2003) [21]; Indian blackout (2012, 2014) [22]; Italy blackout (September 28, 2003) [23], [24] the challenges for effective frequency regulation are prevalent. Large frequency deviations resulting from poor coordination and information exchange between control areas have also been reported as part of the root cause of the recent blackouts [25]. The blackouts have shown that a novel system model incorporating power contract data and more efficient control strategies is required to ensure improved system security, reliability, and power quality in the new

environment. Initially, the synchronous generator compensates for the imbalance using the inertia of the rotor [26]—eventually, the angular velocity of the synchronous generator increases or decreases. Consequently, there is a corresponding decrease or increase in frequency as the angular speed of the generator is proportional to system frequency. All the dynamic states settle down to the new operating states for a stable system. If the frequency exceeds a nominal band (∓ 0.5 Hz), Primary Frequency Control (PFC) is implemented. Thus, continuous control is required to maintain the system in equilibrium [2]. The setpoints of the local governors are controlled using droop characteristics proportional to frequency deviation in PFC. The droop characteristics allow generators to adjust their outputs and collectively share the load such that the frequency of the grid is constant. As PFC is a proportional controller, an offset error is present in the frequency deviation. Hence a secondary integral control action is required to remove the steady-state error in frequency. The secondary frequency control is known as load frequency control (LFC).

In a multi-area system, the secondary frequency control is the function of biased frequency deviation and tile line power deviation within each control area. The frequency deviation is added to the tie-line power deviation between control areas, known as Area Control Error (ACE). The optimal secondary frequency controller considering the rate of tie-line power deviation to eliminate steady-state frequency deviation error has been presented in [27]. If LFC is implemented while maintaining each unit's generation in the control area at their respective economic values, the control is known as Automatic Generation Control (AGC) [28].

In the past, the power system was vertically integrated. Within a control area, a central utility monopoly on the generation, transmission, and distribution of the power and ancillary services such as LFC and voltage control. The central utility regulated the tariff and policies, and the consumers were obligated to follow them. The main task of the tie-lines between control areas was to provide mutual reserve power and not for bulk inter-area power. The uncertainties in load variations and other disturbances were small, power flow patterns were highly predictable, and electric utilities could satisfactorily control their large power plants.

In a deregulated power system, the monopoly of central utility has been abolished, and various services have been unbundled. New entities have emerged, such as Generation Companies (GENCOs), Transmission Companies (TRANSCOs), Distribution Companies (DISCOs), Independent System Operators (ISOs). The consumer has the independence to choose service from these entities depending on their power quality

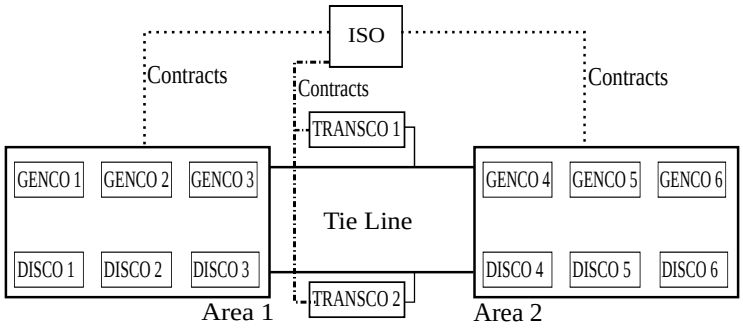

Figure 1.2: Schematic diagram of Deregulated Power System

and tariff. Although the consumer has been benefited from the deregulation of the power system, it has created new operational challenges [29]. The power generation is decomposed into several private GENCOs each operating its power station, and competing with each other and with GENCOs in neighboring control areas to sell power; distribution is divided into many distribution companies DISCOs each owning and operating the different sections of the distribution network, and competing to sell power to consumers. A DISCO can purchase electrical power from any GENCO in its area and across control areas. The transmission network within a control area is owned by a transmission company TRANSCO. An independent entity is known as an Independent System Operator ISO schedules the contracted power flow between market participants GENCOs and DISCOs in neighboring control and monitors contracted ancillary power transactions. In a deregulated power system, AGC changes governor setpoints based on load demand of the same and other control areas by DISCO Participation Matrix (DPM). The rows of a DPM matrix correspond to GENCOs, and the columns of DPM corresponds to a DISCOs [30]. The voltage stability, frequency stability, and line loading studies between control areas were carried out considering conventional power systems have become obsolete. These are now regarded as ancillary services that an independent ISO must regulate. The schematic diagram of deregulated power system is shown in Fig. 1.2.

The increasing electrical loads have pushed the transmission system to operate at its stability limits. Maintaining the power quality and power supply reliability has become more complex with the integration of grid interfaced converters. Increasing penetration of power electronic converters in the power system has reduced the inertia of the power system. The rate of change of frequency (RoCoF) is slow for power system with high inertia while for lower inertia power system the frequency changes instantly. However, the decrease in inertia increases RoCoF levels (>0.5 Hz/s) lead-

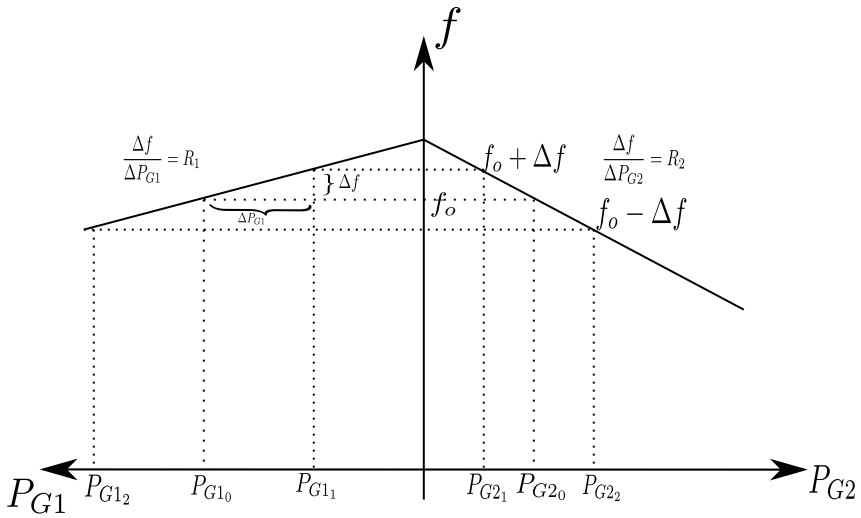

Figure 1.3: Droop characteristic [2]

ing to load shedding, blackout or islanding [31]. Thus the primary and the secondary frequency controllers have to be faster to compensate for the loss of inertia. The modeling and analysis of the power system have to be updated to design suitable control systems, as the random load fluctuations cause dynamic phenomena which occur at different timescales.

1.1.1 Insight on Load Frequency Control

At nominal operating conditions, the system frequency is f_0. Increasing load demand at the nominal operating condition, there is a corresponding decrease in angular speed of synchronous generating units (and thus grid frequency Δf). Consequently, the governor in each generating unit senses the change in rotational speed and adjusts the input valve to change the mechanical input power to the turbine, preventing the grid frequency from declining further. Assume that there is more than one generating unit in the control area, with the governor in each unit sensing the speed of the change of their prime mover and compensating for the speed change. In such a scenario, the generating units end up at different rotating speeds as the governor's response to the speed change is not identical.

A feedback loop based on droop logic is applied to the governor input to maintain synchronous speed across the control area. The droop characteristic of two generating units delivering P_{G1_0}, P_{G2_0} is linear over the range of load variations, as shown

in Fig. 1.3. The frequency settles at a new value $f_0 - \Delta f$ after the intervention of the droop mechanism; this corresponds to a total generation $P_{G1} = P_{G1_0} + \Delta P_{G1} = P_{G1_2}$. Similarly, when load is withdrawn from the network generating units speed-up and droop mechanisms increase the frequency to $f_0 + \Delta f$ and total generation as $P_{G1} = P_{G10} - \Delta P_{G1}$. The droop mechanism regulates the power generation along a fixed load reference setting to intercept a sudden rise or dip in grid frequency and stabilize the frequency at a constant value. However, an error offset of Δf is present in the system. To restore grid frequency to the nominal value, the load reference setting of a turbine governor has to be changed by a secondary control known as LFC [2].

1.2 Research Motivation and Scope

The power flow in interconnected networks is guided by physical network laws and may not flow according to contract paths. Currently, power grids are being operated with reduced security margins due to poor coordination existing between control areas and, with significant restructuring of the power system [32], the increasing penetration of the converter-based loads and sources [33], and the economic constraints which creates large-frequency oscillations in the deregulated power system [34]. The converter-driven instability may arise due to many different reasons, such as grid connected converter controls, operating conditions, power transfer limits, and other similar factors. For example, the fast control dynamics of the grid connected converter may result in rapid voltage, current or frequency changes, which may lead to the maloperation of protection relays fitted to the inverters and cause system tripping [35]. LFC problem in today's power system has further been reinforced by the high penetration of renewable energy sources (RES) with no inertial support, whose contribution to power demands cannot be precisely predicted.

Modern methods are emerging for frequency regulation in low inertia power systems. The existing methods for frequency regulation is inertia emulation by the energy storages. Energy storage devices such as Super Magnetic Energy Storage (SMES) [36],[37], Battery Energy Storage (BESS) [38], Pumped Hydro Storage [39], Flywheel Energy Storages [40], plug-in electric vehicles [41] etc. can absorb a large volume of energy, which can be utilized when a sudden demand appears thereby providing vital support services to the power system. The drawback of energy storage is that they have reduced the inertia of the power system compared to inertial power generators.

The energy storages are controlled to absorb or release the energy that emulates the rotor of the synchronous generator [42]. Recently, the DC link capacitors are showing improvement in stresses due to high-RoCoF levels and low-frequency nadir. DC link voltage and capacitance play similar roles as the frequency ω_r and moment of inertia J , respectively. This results in the proposal of a simple frequency controller, which proportionally relates the grid frequency to the dc-link voltages of grid-connected power converters for generating the emulated inertia or known as the virtual inertia [43]. When the inertia emulated by dc-link capacitors is insufficient other frequency support functions are required, and for that energy storages can further be employed. Amongst the energy storages battery energy storage has highest energy density, quickest response when applied to frequency control [44], [45].

The enhanced frequency response control scheme requires suppliers to respond to under-frequency events instantly within 1 s and maintain the outputs for at least 15 min [46]. Although battery energy storages have been used to emulate inertia this technique has a great potential for providing an additional inertia control in the future [47]. In recent years, power flow in the network has become more flexible with the development of Flexible AC Transmission System (FACTS). FACTS devices help regulate the power flow in a transmission line. The resonance stability issues are mainly caused by the effects of FACTS or high-voltage direct current transmission systems (HVDC) on torsional aspects (i.e., torsional resonance), and the effects of doubly fed induction generator (DFIG) controls on electrical aspects (i.e., electrical resonance), which encompass the subsynchronous resonance (SSR). The causes of resonance stability have been identified and the solutions have also been proposed accordingly. Series FACTS devices such as Thyristor Controlled Phase Shifter (TCPS) [48], [49], Static Synchronous Series Compensator (SSSC) [50], [51] are used to improve the dynamic stability and frequency support in the transmission line [52]. Static var compensators can be used to damp torsional resonance, and supplemental controllers in DFIG control can help to damp the electrical resonance. Static Synchronous Compensator (STATCOM) [53] is interfaced in parallel with the grid for improving bus voltage stability and damping power oscillations but not for frequency stabilization.

In literature the application of different FACTs devices such as SSSC, TCSC, SVC etc. for frequency regulation has been reported in [25], [54], [55],[56] but STATCOM is not reported. As STATCOM is preferred over series compensating devices such as SSSC, TCSC etc. [57], [58], [53] it is popular compared to the series FACTS devices.

The damping of power oscillations is a good measure of small-signal stability of the power system. Faster the power oscillations are damped out, the more stable the system is [59],[60]. A comparison between SSSC and STATCOM for power oscillation damping shows that STATCOM damps larger load variations more effectively than SSSC [61].
Several works have been published on the LFC issue. These works have adopted control strategies ranging from standard classical control techniques to modern control strategies such as optimal linear quadratic regulator (LQR) [62], robust control [63], [64] and intelligent control methods. Various search-based algorithms tuned the gain settings of AGC controllers in the literature. A sine-cosine based stochastic algorithm was implemented in [65],[66], while in [67], fractional-order PI (proportional-integral) and PID (proportional integral derivative) controller was tuned by crow search algorithm. Gravitational Search Algorithm (GSA) tuned sliding mode control gain settings were implemented in [68]. A model predictive controller-based frequency regulation was presented in [69]. Fuzzy based load frequency control using PID controllers implemented in [70]. Compared to GA, the above-implemented algorithms have a few drawbacks. Sine cosine algorithm is reported to be faster but more inaccurate than GA. GSA stuck to the local optima solution and became inactive compared to the GA, which is better in searching global optima. To implement model predictive control, the system model has to be accurate. Crow search algorithm has better performance than GA, but the iteration time is longer [71]. Nonetheless, most of the works were focused on the vertically integrated power system structure. Some publications have considered LFC in a deregulated environment. Still, the strategies have yielded a very high-order controller and neglected practical system constraints.

1.3 Proposed Work

Given the drawbacks in the current literature, this thesis considers the development of the novel model of LFC schemes and aims to :

- develop small-signal model of SMES, STATCOM, BESS, Solar PV for the regulated and deregulated power system for participating in LFC,
- optimize the integral controller gains of the multi-area regulated LFC model with Solar PV and Battery Energy Storage to improve stability of the system,

- improve ancillary service such as Load following with STATCOM SMES in a deregulated power system that effectively captures the various power transaction contracts,
- optimally place and design the energy storage and the FACTS devices.

1.4 Outline of the Thesis

- Load Frequency Regulation with Solar PV and BESS is presented in chapter 2.
- Chapter 3 highlights the frequency regulation in a deregulated power system with STATCOM and SMES.
- The converter modelling and control for conventional and deregulated power system has been presented in chapter 4.
- The sizing and optimal placement of the energy storage and FACTS controllers have been presented in chapter 5.
- Chapter 6 presents the conclusion and the future scope of the thesis.

Chapter 2

Load Frequency Control in Regulated Power System

A multiarea multimachine systems consist of different energy sources such as thermal, hydro, nuclear, gas, wind, and solar. The planning and commissioning of the new generating plants, transmission lines, and distribution systems require stability studies to estimate voltage capacity and power transfer capacity. A power system stability study is carried out by perturbing the power system about the operating point. These studies are assisted by several computer programs based on the power system's mathematical models. The non linear power system is perturbed about the equilibrium state with small load perturbation and the linearized model is obtained for small signal stability study. The linearized model of power system is suitable for LFC study. The task of LFC is to maintain the frequency constant and control tie-line power between control areas to the scheduled value. Thus, energy sources with high ramping rates, such as hydro and gas energy sources, are preferable for participating in LFC. In contrast, energy sources such as nuclear and thermal energy sources contribute to base loads [72]. In the next section brief description of generating unit linearized model for LFC of single area power system and multiarea power system is presented.

2.1 Linear Time Invariant Model of Generating Unit

2.1.1 Generator Modelling

The generators lying within the same control areas can be represented as a single generator for modelling. The equivalent moment of inertia and the damping coeffi-

ω	Angular Speed (rad/s)
α	Angular Acceleration (rad/s^2)
δ	Phase Angle of Rotor (rad)
T_e	Electrical Torque (Nm)
T_m	Mechanical Torque (Nm)
P_e	Electrical Power (KW)
P_m	Mechanical Power (KW)
J	Moment of inertia
M	Angular Momentum

cient are calculated for LFC study [73]. The dynamics of the rotation of rotor of the synchronous generator varies with the mechanical input power and the electrical output power. The relation between angular acceleration, mechanical input power, and electrical output power is given by the swing equation. Assuming the generator is rotating at constant angular speed ω_0. The phase angle in absence of angular acceleration is given as

$$\delta_0 = \int \omega_0 dt \tag{2.1}$$

The generator undergoes acceleration or de-acceleration due to mechanical or electrical disturbances. The deviation of the rotor angle from the reference frame rotating at constant angular speed ω_0 is given as

$$\Delta\delta = \int (\omega_0 + \alpha t) dt - \delta_0 \tag{2.2}$$

$$\Delta\delta = \frac{1}{2}\alpha t^2 \tag{2.3}$$

The deviation in angular speed is given as

$$\Delta\omega = \alpha t \tag{2.4}$$

Assuming there are no damper windings, the swing equation is given as

$$J\frac{d\omega}{dt} = T_m - T_e \tag{2.5}$$

Multiplying, ω_0 to (3.2.5), we have

$$J\omega_0\frac{d\omega}{dt} = M\frac{d\omega}{dt} = \omega_0(T_m - T_e) = P_m - P_e \tag{2.6}$$

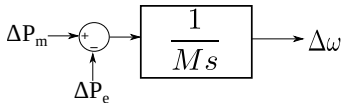

Figure 2.1: Generator Model

Linearizing, the above equation we have

$$M\frac{d\Delta\omega}{dt} = \Delta P_m - \Delta P_e \tag{2.7}$$

which can be expressed in frequency domain using Laplace transform as

$$Ms\Delta\omega(s) = \Delta P_m(s) - \Delta P_e(s) \tag{2.8}$$

The generator model is shown in Fig. 2.1.

2.1.2 Turbine Model

The real power from the source in a power system is controlled by the mechanical power output of the prime mover. Depending on the type of generation, the prime mover may be a steam turbine, gas turbine, hydro-turbine or diesel engine. In the case of a steam or hydro- turbine, mechanical power is controlled by the opening or closing of valves regulating the input of steam or water flow into the turbine. Steam (or water) input to turbines must be continuously regulated to match real power demand, failing which the machine speed will vary with consequent change in frequency. The models for the prime mover must take account of the steam supply and boiler control system characteristics in the case of a steam turbine. A reheat steam turbine can be represented quite adequately by the transfer function given as [74]

$$\frac{1 + sK_{RH}T_{RH}}{(1 + sT_{RH})(1 + sT_t)} \tag{2.9}$$

The time constant T_{RH} has a value in the range of 10 s and approximates the time delay for charging the reheat section of the boiler. K_{RH} is a reheat coefficient equal to the proportion of torque developed in the high-pressure section of the turbine. Typical values of K_{RH} are from 0.25 to 0.5. For state-space representation, the above transfer function can be decomposed into the product of two transfer functions, as shown in Fig. 2.2.

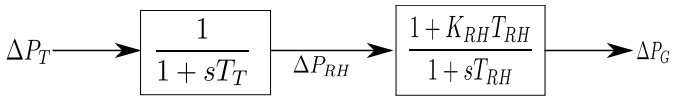

Figure 2.2: Reheat Turbine Model

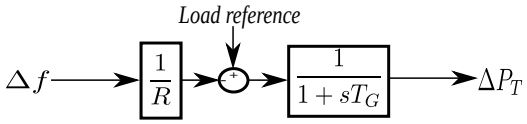

Figure 2.3: Governor Model

2.1.3 Load Model

The loads on a power system consist of a variety of electrical devices. Some are purely resistive, some are motor loads with variable power–frequency characteristics, and others exhibit quite different characteristics. Since motor loads are a dominant part of the electrical load, there is a need to model the effect of a change in frequency on the net load drawn by the system. The relationship between the change in load due to the change in frequency is given by

$$\Delta P_{freq} = D\Delta\omega \tag{2.10}$$

where D is expressed as percent change in load divided by percent change in frequency. Note that D = 1.5 tells us that the load would change by 1.5 pu for 1 pu change in frequency. The net change in ΔP_e is given as

$$\Delta P_e = \Delta P_L + D\Delta\omega \tag{2.11}$$

where ΔP_L is the load independent of frequency change.

2.1.4 Governor model

Suppose a generating unit is operated with a fixed mechanical power output from the turbine. Any load change would lead to speed change sufficient to cause the frequency-sensitive load to precisely compensate for the load change. This condition would allow system frequency to drift far outside acceptable limits. The frequency deviation is overcome by adding a governing mechanism that senses the machine speed and adjusting the input valve to change the mechanical power output to compensate for load changes and restore frequency to a nominal value.

To be able to run two or more generating units in parallel on a generating system, the governors are provided with a feedback signal that causes the speed error to go to 0 at different values of generator output. The block diagram for the governor is shown in Fig. 2.3. The value of R determines the slope of the characteristic. Common practice is to set R on each generating unit to change from 0 to 100 %. If two generators with drooping governor characteristics are connected to a power system, the system will settle to a unique frequency such that generators will share the load change between them.

2.2 Static Synchronous Compensator Model

Static Synchronous Compensator (STATCOM) is a shunt FACTS device. It can regulate the reactive power of the transmission line. The steady state model of STATCOM is presented in Fig. 2.4 in which STATCOM is modelled as a constant current source. To study steady state power flow, synchronous generator is modelled as constant impedance in this section. The power flow in a transmission line is given as

$$P_{g1} = V_{g1}E_g\frac{sin(\delta_{g1}-\theta_g)}{X_1} \tag{2.12}$$

where V_{g1}, is the generator voltage, E_g is the terminal STATCOM Bus voltage, δ_{g1} is the phase angle of the generator with respect to the phase angle of the terminal STATCOM Bus voltage and X_1 is the interface inductance and transformer reactance. Linearizing (2.12), the deviation in the power generated in area 1 is given as

$$\Delta P_{g1} = \Delta E_g\frac{V_{g10}sin(\delta_{10}-\theta_{g0})}{X_1} + \Delta V_{g1}\frac{E_{g0}sin(\delta_{10}-\theta_{g0})}{X_1} - \Delta\theta_g\frac{V_{g10}E_{g0}cos(\delta_{10}-\theta_{g0})}{X_1} \tag{2.13}$$

Assuming the generator as constant voltage source $\Delta V_{g1} = 0$. Also, due to lack of active power source in STATCOM, it can not inject active power, that is controlled by $\Delta\theta_g$. Thus, the power deviation due to the STATCOM is given as

$$\Delta P_{g1} = \Delta E_g\frac{V_{g10}sin(\delta_{10}-\theta_{g0})}{X_1} \tag{2.14}$$

From Fig. 2.4, the terminal voltage of the STATCOM is given as

$$E_g = V_{g1}\angle\delta_{g1} + jX_1I_{STATCOM}\angle\delta_{g1} \pm \frac{\pi}{2} \tag{2.15}$$

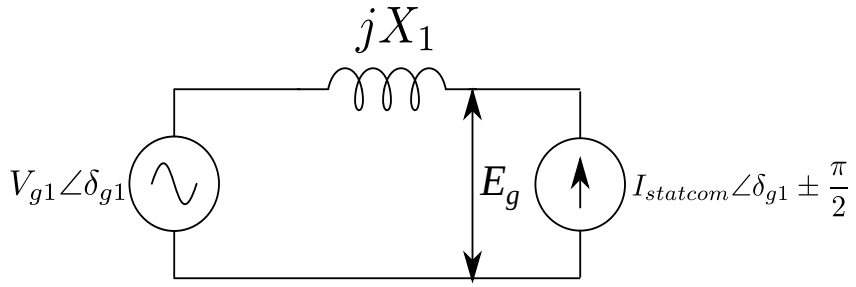

Figure 2.4: STATCOM modelled as current source

Assuming, that the STATCOM injects a current $I_{STATCOM}\angle(\delta_{g1} \pm \frac{\pi}{2})$. The deviation in ΔE_g is expressed as

$$\Delta E_g = \pm j\Delta I_{STATCOM} X_1$$

This corresponds to the deviation in active power generated as

$$\Delta P_{g1} = \pm j\Delta I_{STATCOM} V_{g10} sin(\delta_{10} - \theta_{g0}) \tag{2.16}$$

As STATCOM, injects reactive power in the line, this corresponds to the deviation of active power generated from the source due to reactive power injected by STATCOM. The control problem is then reduced to identify the injected current $\pm\Delta I_{STATCOM}$. An appropriate input control signal has to be chosen based on frequency deviation such that the deviation in current is calculated. At the point of common coupling, we have power transmitted (P_t) given as

$$P_t = P_{g1} = V_{g1} E_g \frac{sin(\delta_{g1} - \theta_g)}{X_1} \tag{2.17}$$

Linearizing, the above equation with respect δ_{g1}, we have

$$\Delta P_t \approx V_{g1} E_g \frac{cos(\delta_{g1} - \theta_g)}{X_1} (\omega_{g1}) \Delta\delta_{g1} \tag{2.18}$$

which can be rewritten as

$$\frac{d\Delta P_t}{dt} \approx V_{g1} E_g \frac{cos(\delta_{g1} - \theta_g)}{X_1} (\omega_{g1}) \frac{d\Delta\delta_{g1}}{dt} \tag{2.19}$$

Here, derivative of the transmitted power deviation (ΔP_t), corresponds to the frequency deviation. Thus, we can estimate the frequency deviation signal from trans-

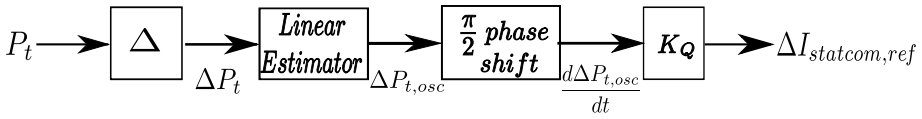

Figure 2.5: Block Diagram STATCOM reference current generation [3]

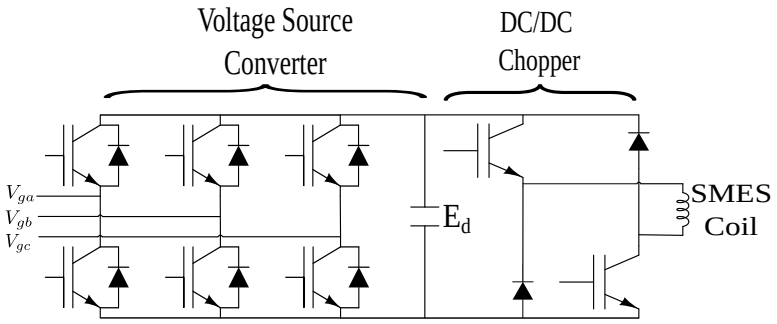

Figure 2.6: SMES schematic diagram

mitted power. The control block diagram for reference generation is presented in Fig. 2.5.

2.3 Super Magnetic Energy Storage Model

SMES is a DC device that stores energy in the magnetic field. The DC current flowing through a superconducting wire creates the magnetic field in a lossless inductive coil. Few features of SMES are high storage cost, best efficiency, best round trip efficiency, lowest energy density, as coil weight is more. The superior power density makes it suitable for load following [75]. When power is scheduled between utility control areas, the actual net power must match closely with the scheduled power. When a load disturbance occurs in a control area leading to an error in generation and load consumption . SMES can be designed with appropriate controls to inject power to eliminate this error and ensure that generators are efficiently scheduled and power demands are met. SMES employs a voltage source converter that allows independent control of active and reactive power regulation. The schematic diagram of SMES is given in Fig. 2.6. SMES coil is highly inductive, thus, instantaneous change in current is not possible. To achieve bidirectional power flow, the voltage across the coil is changed by DC/DC chopper. The deviation in power is then given as $\Delta E_{dc} I_{SMES}$. The control block diagram of SMES is given in Fig. 2.7.

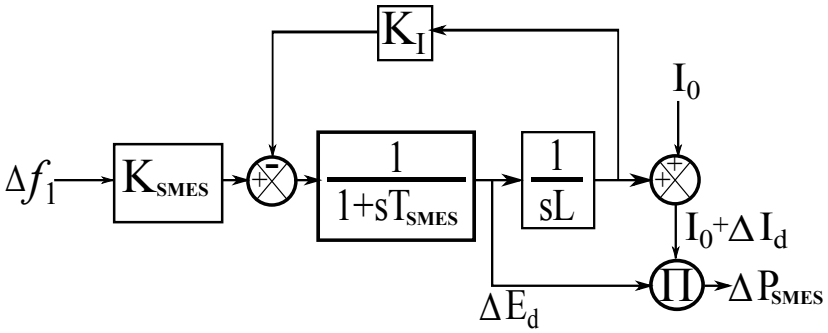

Figure 2.7: SMES control diagram

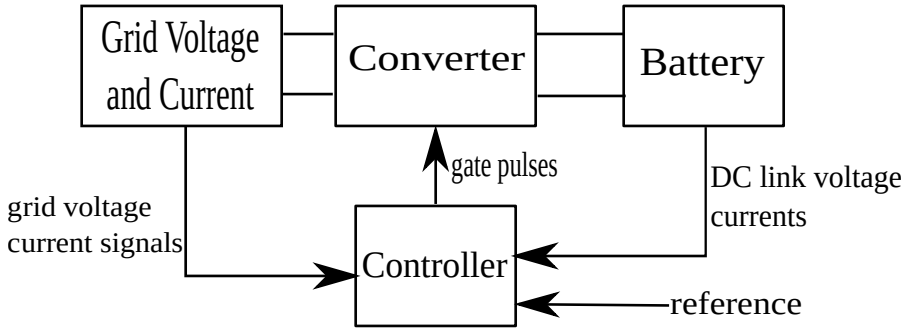

Figure 2.8: BESS Schematic

2.4 Battery Energy Storage System

A useful and systematic dynamic model of a Battery Energy Storage System (BESS) is developed for a large-scale power system stability study. The model takes into account converter equivalent circuits, battery characteristics and internal losses along with both charging mode and discharging mode are presented. The model is expressed in equivalent transfer function blocks, and it can be easily used in dynamic stability analysis of a power system. BESS is integrated to the power system with a power electronic converter. Vector control has been implemented for modeling such that the charging and discharging of the BESS are governed. The active power compensation required to maintain the frequency can be derived from the Phase Lock Loop (PLL) at the point of common coupling.

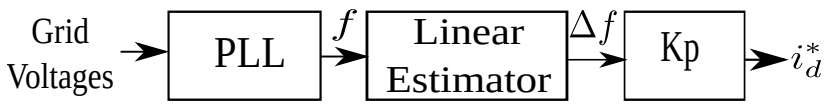

Figure 2.9: Reference derivation for BESS [4]

The schematic block diagram of BESS is presented in Fig. 2.8. The reference generation for BESS control is shown in Fig. 2.9. The active power injected by BESS is then given as

$$\Delta P_{BESS} = V_d i_d \tag{2.20}$$

where V_d is obtained from grid voltages Park transformation.

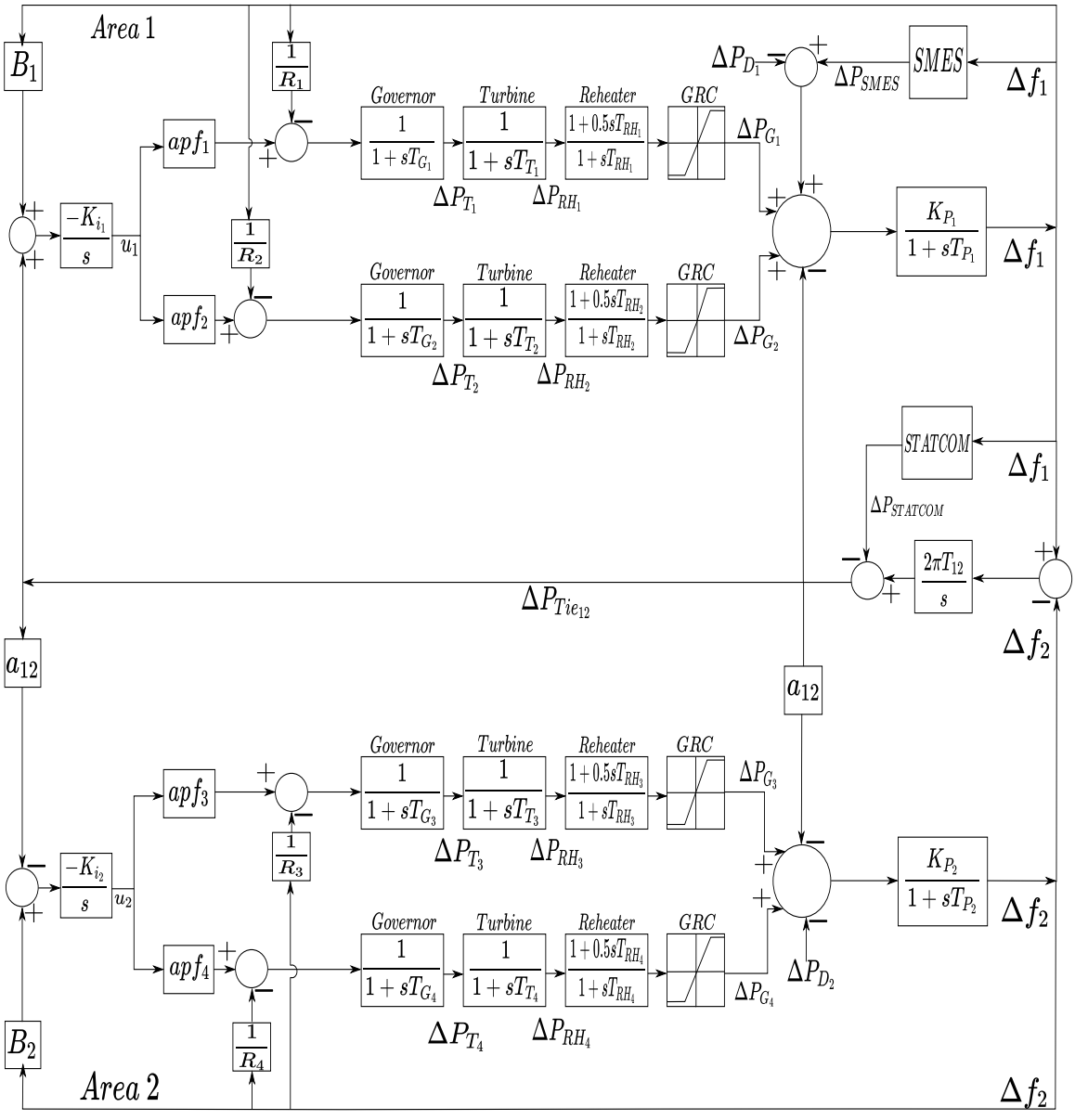

Figure 2.10: AGC Block Diagram With SMES and STATCOM

2.5 Regulated Power System with Static Synchronous Compensator and Super Magnetic Energy Storage

A sample two-area power system with STATCOM and SMES is studied and presented in Fig. 2.10. Conventionally, at the steady state, the generation matches with system loads and associated system losses. Any change in generation or load disturbs the power balance in the system, which may perturb the operating conditions. In addition to primary control loop, an additional control loop known as secondary control loop is added with an integral control to minimize the steady-state error over a specific period of time. In a reheat turbine, the steam is passed through the high-pressure stage of the turbine and then passed through the re-heater. The reheated steam is then passed through the low-pressure stage of the turbine. This cycle improves the efficiency of the turbine compared to the non-reheat turbine [76]. The dynamic performance of the steam turbine is analyzed, considering a GRC of 10 % / min [77]. For economic reasons, the generating units within a given area participate in load frequency control as per Area Participation factors ($apfs$). In any given area, sum of $apf's$ is always equal to 1. Therefore, $apf_1 + apf_2 = 1$ in area 1 and $apf_3 + apf_4 = 1$ in area 2. To meet the load demands, each generating unit in the same control area has to generate power as per standard industrial practices, such that the sum of $apfs$ is unity. To depict the simulation results $apf_1 = apf_2 = 0.5$ and $apf_3 = apf_4 = 0.5$ considered in this work. The optimized integral gain settings for different combinations of $apfs$ with step disturbance of 0.1 p.u. at time t = 0, in area 1 only and keeping area 2 uncontrolled are presented in Table 2.1. While with 0.1 p.u. step disturbance at t = 0, in area 2 only and keeping Area 1 uncontrolled is presented in Table 2.2.

The STATCOM-SMES combination in sample power system are modelled as first order dynamic equations, that are given as

$$\dot{X} = AX + BU + \Gamma P \tag{2.21}$$

where A is the state matrix, B is the input matrix and Γ is the disturbance matrix of appropriate dimension.

The power oscillations in an under damped power system are the result of sus-

Table 2.1: Optimized Integral Gain Constants for 0.1 p.u. MW disturbance in Area 1

		With STATCOM-SMES		Without STATCOM-SMES	
apf_1	apf_2	K_{i_1}	K_{i_2}	K_{i_1}	K_{i_2}
0.9	0.1	1.387	1.0845	1.3375	0.5521
0.75	0.25	1.264	1.0845	1.0562	0.4427
0.5	0.5	0.9864	0.1276	0.7827	0.5064
0.25	0.75	1.2641	1.0845	1.0711	0.45
0.1	0.9	3.287	1.0845	2.57	0.6078

Table 2.2: Optimized Integral Gain Constants for 0.1 p.u. MW disturbance in Area 2

		With STATCOM-SMES		Without STATCOM-SMES	
apf_3	apf_4	K_{i_1}	K_{i_2}	K_{i_1}	K_{i_2}
0.9	0.1	0.4262	2.5851	0.3742	2.4739
0.75	0.25	0.2394	1.6328	0.3924	1.5913
0.5	0.5	0.4324	0.9734	0.5683	0.8435
0.25	0.75	0.2956	1.0461	0.1346	1.0453
0.1	0.9	0.3486	2.6328	0.2594	2.3453

tained acceleration and de-acceleration of the rotor of synchronous generator in response to small disturbances. The power oscillations are damped out by rapid compensating devices such as an SMES. SMES consists of super conducting coil, which is connected to an AC grid by a voltage source converter. SMES coil is held at 50-77 K temperature range to increase the power density. The coil stores magnetic energy in superconducting DC coil that is controlled to compensate the sudden load demands in the grid [78]. As the load change is reflected in the frequency deviation, the input for the controller is taken as frequency deviation. Since the coil is inductive, a sudden change in current is not possible. Hence DC link voltage has to be regulated by modulating DC link current using pulse width modulation which discharges the SMES when a sudden load demand occurs. Similarly, when the load demand drops, the SMES gets charged to absorb the increased active power in the grid. SMES is interconnected with the three phase grid ($k = a, b, c$) by a voltage source converter which is modelled mathematically as, [79],

$$V_{kg} = i_{kg} R_s + L_s \frac{d i_{kg}}{dt} + V_{ki} \tag{2.22}$$

where V_{kg} is the grid voltage, V_{ki} is the converter output voltage and i_{kg} is the instantaneous grid current, R_s and L_s being the interfacing resistance and inductance as shown in Fig. 2.11. Park's transformation from three phase system to d-q coordinate system is given as

$$\begin{bmatrix} V_q \\ V_d \\ V_o \end{bmatrix} = \frac{2}{3} \begin{bmatrix} cos(\delta) & cos(\delta - \frac{2\pi}{3}) & cos(\delta - \frac{4\pi}{3}) \\ sin(\delta) & sin(\delta - \frac{2\pi}{3}) & sin(\delta - \frac{4\pi}{3}) \\ \frac{1}{\sqrt{2}} & \frac{1}{\sqrt{2}} & \frac{1}{\sqrt{2}} \end{bmatrix} \begin{bmatrix} V_a \\ V_b \\ V_c \end{bmatrix}$$

The active power in d-q co-ordinate is then given as, $P = V_d i_d + V_q i_q$
where $V_d = 0$, thus, $P = V_q i_q$.
Perturbing above equation, we get, $\Delta P = \Delta V_q i_q + V_q \Delta i_q$
Assuming, the voltage deviations are negligible compared to current deviations we have, $\Delta P = V_q \Delta i_q$

Park's transformation of the (2.22) yields voltage and currents in d-q domain and the active power deviation is

$$\Delta P_{SMES} = v_{qg} \Delta i_{qg} + v_{dg} \Delta i_{dg} \tag{2.23}$$

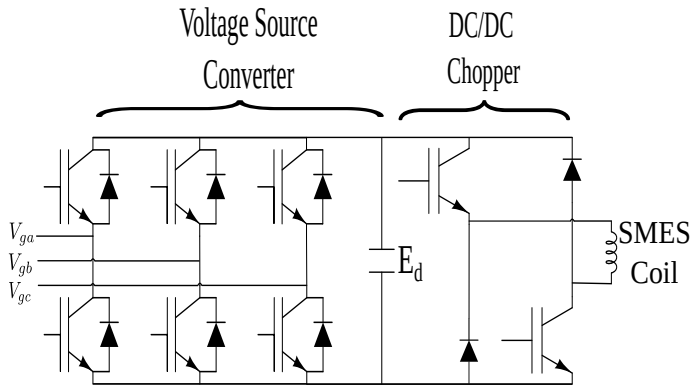

Figure 2.11: Schematic diagram of SMES [5]

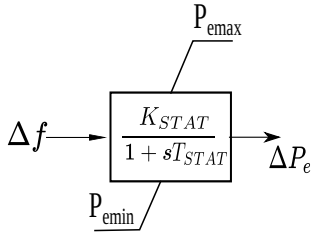

Figure 2.12: STATCOM control

For the control of the active power output from SMES, Δi_{dg} is forced to zero and Δi_{qg} is controlled to regulate active power.

$$\Delta P_{SMES} = V_{qg} \Delta i_{qg} \tag{2.24}$$

The oscillations can also be controlled by a shunt compensating device such as STATCOM which will inject the reactive power into the transmission line during accelerating period and absorb reactive power during de-accelerating period and regulate active power in the line [80]. STATCOM conditions the limit of transmittable power in the line. Thus area frequency is chosen as STATCOM control input. The power flow between STATCOM and the grid is given by (2.25) where x is transformer impedance.

$$P_e = \frac{V_1 V_2 sin\delta_{12}}{x} \tag{2.25}$$

Perturbing (2.25), about the nominal operating values we get

$$P_e + \Delta P_e = \frac{(V_1^0 + \Delta V_1)(V_2^0 + \Delta V_2) sin(\delta_{12}^0 + \Delta\delta_{12})}{x} \tag{2.26}$$

If the voltage deviations are negligible, then

$$\Delta P_e = \frac{V_1^0 V_2^0 cos\delta_{12}^0 \Delta\delta_{12}}{x} \tag{2.27}$$

Taking Laplace transform,

$$\Delta P_e(s) = \frac{V_1^0 V_2^0 cos\delta_{12}^0 \Delta\delta_{12}(s)}{x} \tag{2.28}$$

Since

$$\Delta F_{12}(s) = Ks\Delta\delta_{12}(s) \tag{2.29}$$

where $K = \frac{1}{2\pi}$, from (2.28) and (2.29)

$$\Delta P_e(s) = \frac{K_{STAT}\Delta F_{12}(s)}{s} \tag{2.30}$$

where,

$$K_{STAT} = \frac{V_1^0 V_2^0 cos\delta_{12}^0}{Kx} \tag{2.31}$$

STATCOM control strategy is presented in Fig. 2.12 where the STATCOM has been modelled as a first order transfer function and the time constant of STATCOM operation is given as T_{STAT}. The state equations for STATCOM-SMES in two area power system is given as

$$\Delta\dot{f}_1 = \frac{-\Delta f_1}{T_{P_1}} + \frac{K_{P_1}}{T_{P_1}}(-\Delta P_{tie_{12}} + \Delta P_{G_1} + \Delta P_{G_2} + \Delta P_{SMES} - \Delta P_{D_1}) \tag{2.32}$$

$$\Delta\dot{f}_2 = \frac{-\Delta f_2}{T_{P_2}} + \frac{K_{P_2}}{T_{P_2}}(-a_{12}\Delta P_{tie_{12}} + \Delta P_{G_3} + \Delta P_{G_4} - \Delta P_{D_2}) \tag{2.33}$$

$$\Delta\dot{P}_{tie_{12}} = (2\pi T_{12} + \frac{K_{st_1}}{T_{P1}} + K_{st_2})\Delta f_1 + K_{st_1}\frac{K_{P1}}{T_{P1}}(\Delta P_{tie_{12}} - \Delta P_{G1} - \Delta P_{G2} - \Delta P_{SMES}) - 2\pi T_{12}\Delta f_2 \tag{2.34}$$

$$\Delta\dot{P}_{G_1} = -\frac{\Delta P_{G_1}}{T_{RH_1}} + \Delta P_{RH_1}(\frac{1}{T_{RH_1}} - \frac{1}{2T_{T_1}}) + \frac{\Delta P_{T_1}}{2T_{T_1}} \tag{2.35}$$

$$\Delta \dot{P}_{RH_1} = \frac{-\Delta P_{RH_1}}{T_{T_1}} + \frac{\Delta P_{T_1}}{T_{T_1}} \tag{2.36}$$

$$\Delta \dot{P}_{G_2} = -\frac{\Delta P_{G_2}}{T_{RH_2}} + \Delta P_{RH_2}\left(\frac{1}{T_{RH_2}} - \frac{1}{2T_{T_2}}\right) + \frac{\Delta P_{T_2}}{2T_{T_2}} \tag{2.37}$$

$$\Delta \dot{P}_{RH_2} = \frac{-\Delta P_{RH_2}}{T_{T_2}} + \frac{\Delta P_{T_2}}{T_{T_2}} \tag{2.38}$$

$$\Delta \dot{P}_{G_3} = -\frac{\Delta P_{G_3}}{T_{RH_3}} + \Delta P_{RH_3}\left(\frac{1}{T_{RH_3}} - \frac{1}{2T_{T_3}}\right) + \frac{\Delta P_{T_3}}{2T_{T_3}} \tag{2.39}$$

$$\Delta \dot{P}_{RH_3} = \frac{-\Delta P_{RH_3}}{T_{T_3}} + \frac{\Delta P_{T_3}}{T_{T_3}} \tag{2.40}$$

$$\Delta \dot{P}_{G_4} = -\frac{\Delta P_{G_4}}{T_{RH_4}} + \Delta P_{RH_4}\left(\frac{1}{T_{RH_4}} - \frac{1}{2T_{T_4}}\right) + \frac{\Delta P_{T_4}}{2T_{T_4}} \tag{2.41}$$

$$\Delta \dot{P}_{RH_4} = \frac{-\Delta P_{RH_4}}{T_{T_4}} + \frac{\Delta P_{T_4}}{T_{T_4}} \tag{2.42}$$

$$\Delta \dot{P}_{T_1} = \frac{-\Delta f_1}{R_1 T_{G_1}} + \frac{-\Delta P_{T_1}}{T_{G_1}} + \frac{u_1}{T_{G_1}} \tag{2.43}$$

$$\Delta \dot{P}_{T_2} = \frac{-\Delta f_1}{R_2 T_{G_2}} + \frac{-\Delta P_{T_2}}{T_{G_2}} + \frac{u_1}{T_{G_2}} \tag{2.44}$$

$$\Delta \dot{P}_{T_3} = \frac{-\Delta f_2}{R_3 T_{G_3}} + \frac{-\Delta P_{T_3}}{T_{G_3}} + \frac{u_2}{T_{G_3}} \tag{2.45}$$

$$\Delta \dot{P}_{T_4} = \frac{-\Delta f_2}{R_4 T_{G_4}} + \frac{-\Delta P_{T_4}}{T_{G_4}} + \frac{u_2}{T_{G_4}} \tag{2.46}$$

$$\dot{u_1} = -K_{i_1} B_1 \Delta f_1 - K_{i_1} \Delta P_{tie_{12}} \tag{2.47}$$

$$\dot{u_2} = -K_{i_2} B_2 \Delta f_2 + K_{i_2} a_{12} \Delta P_{tie_{12}} \tag{2.48}$$

$$\dot{\Delta P_{SMES}} = \Delta f_1(K_{SMES} + K_c) + \frac{K_{P_1} G}{T_{P_1}}(\Delta P_{tie_{12}} - \Delta P_{G_1} - \Delta P_{G_2} - \Delta P_{SMES}) \tag{2.49}$$

$$\dot{\Delta P_{STATCOM}} = \Delta f_1(\frac{K_{STAT}}{T_{STAT}} + G_s) - \frac{K_{STAT} K_{P1} \Delta P_{tie_{12}}}{T_P 1} + \frac{K_{STAT}}{T_{P1}}(\Delta P_{G1} + \Delta P_{G2} + \Delta P_{SMES}) \tag{2.50}$$

Table 2.3: System Parameters [9][6]

Rated Area Capacities	(P_{R1}, P_{R2})	1200 MW
Generator gain constants	(K_{p1}, K_{p2})	120 Hz/p.u. MW
Generator time constant	(T_{p1}, T_{p2})	20 s
Governor time constant	$(T_{G1}, T_{G2}, T_{G3}, T_{G4})$	0.08 s
Turbine time constant	$(T_{T1}, T_{T2}, T_{T3}, T_{T4})$	0.3 s
Turbine time constant	$(T_{RH1}, T_{RH2}, T_{RH3}, T_{RH4})$	10 s
Frequency Bias Constant	(B_1, B_2)	0.4249
Speed Regulation	(R_1, R_2, R_3, R_4)	2.4 Hz/p.u. MW
STATCOM Gain	(K_{STAT})	0.049
Synchronizing Coefficient	(T_{12})	0.0866
SMES Control Gain	(K_{SMES})	0.335
SMES time constant	(T_{SMES})	0.1 s
STATCOM time constant	(T_{ds})	0.5 ms
Cell		Polycrystalline Silicon
Rated power output	P_{PV}	216 W
Open circuit voltage	V_{oc}	36.50 V
Short circuit current	I_{SC}	8.10 A
Diode ideality factor	A	1.45
Inverse diode saturation current	I_{or}	3.047×10^7 A
Ambient Temprature	T	25^oC
Boltzmann's constant	K	1.38×10^{23}
Band gap energy	E_g	1.11 eV
Solar Insolation	S	1000 W/m^2
Solar PV gain constant	K_{PV}	0.1
Solar PV time constant	T_{PV}	1.8 s
BESS gain constant	K_{BESS}	1/300
BESS time constant	T_{BESS}	0.1 s

The parameters used for the two area system and STATCOM-SMES combination are given in Table 2.3. The convergence of the objective function with nu-

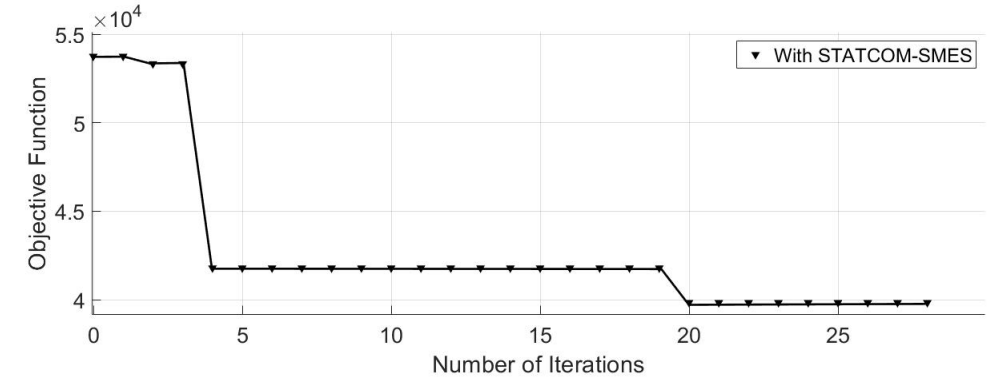

(a) With STATCOM-SMES

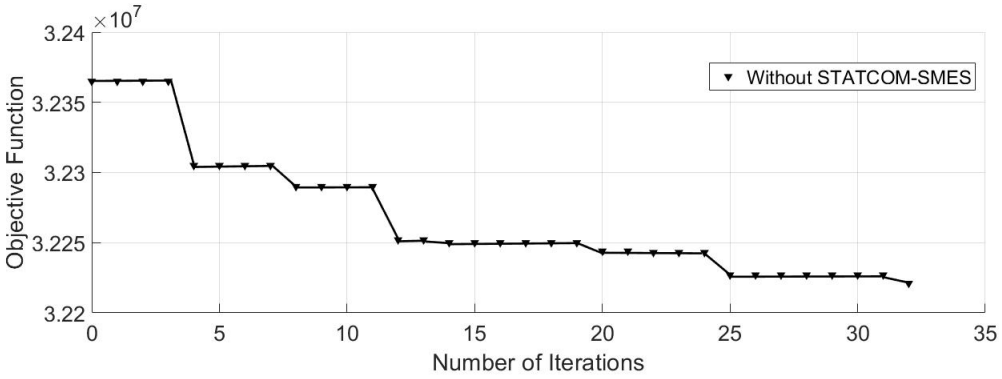

(b) Without STATCOM-SMES

Figure 2.13: Objective function vs. No. of Iterations and disturbance in Area 1

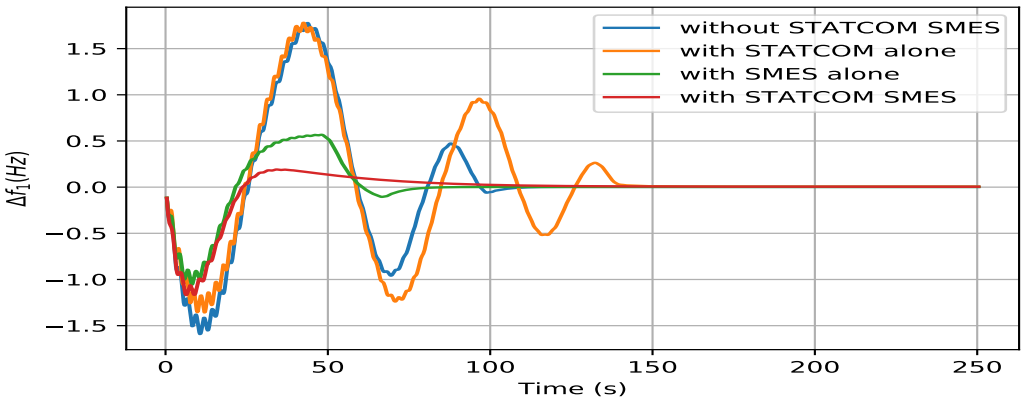

(a) Frequency Deviation in area 1

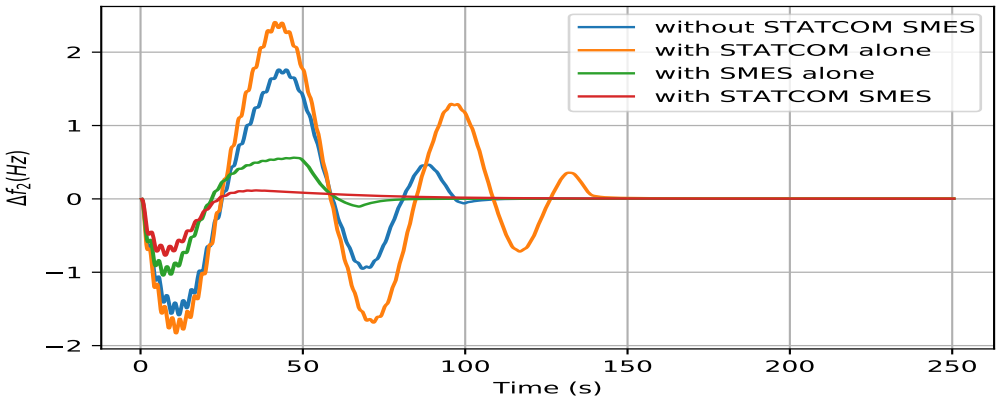

(b) Frequency Deviation in Area 2

Figure 2.14: Frequency deviations with 0.1 pu disturbance in area 1 only .

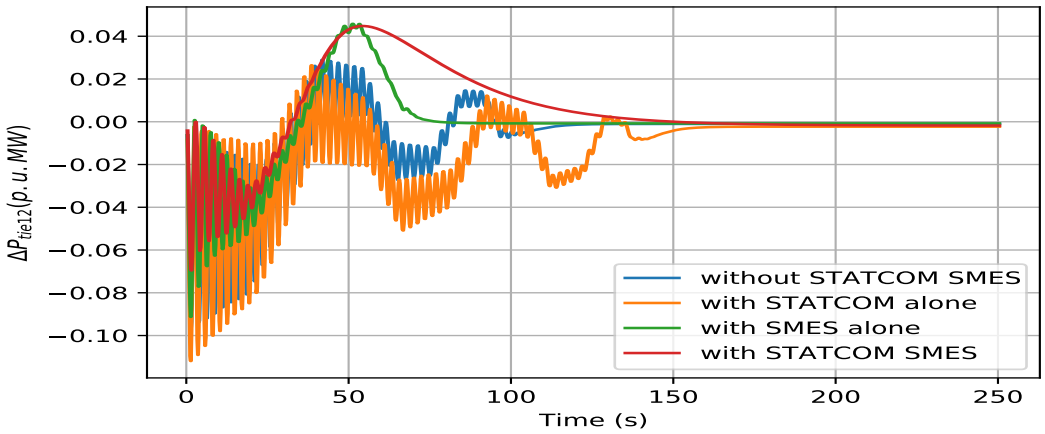

Figure 2.15: Tie line Power deviation with 0.1 pu disturbance in Area 1 only

ber of iterations is shown in Fig. 2.13. The system's different dynamic responses with optimal gain settings are presented in Figs. 2.14 to 2.17. With a step load change of 0.1 p.u in area 1, Fig. 2.14 shows the area frequency deviations (Δf_1 and Δf_2). The transients have been minimized effectively in both the area frequencies using STATCOM-SMES. Further, settling time also has been improved. Fig. 2.15 depicts that the tie-line power oscillations have damped out with STATCOM-SMES much faster with a reduced settling time of approximately 45 secs than the case without STATCOM-SMES. The power output deviations of the generating units ($\Delta P_{G1}, \Delta P_{G2}, \Delta P_{G3}, \Delta P_{G4}$) in both the areas as shown in Fig. 2.16 and Fig. 2.17, show faster responses and improved settling times with reduced peak overshoots. Since a load perturbation of 0.1 p.u. MW and an apf of 0.5 each is considered, each generating unit in area 1 must settle down to $0.1 \times 0.5 = 0.05$ p.u. MW at a steady state as seen from Fig. 2.16. Further, since the load perturbation occurred in area 1, the power output deviation of generating units in area 2 must be zero as per standard industrial practices. This is evident from Fig. 2.17.

Different configurations involving STATCOM and SMES in the same and different areas were simulated and studied. The results obtained in all the cases were more or less similar. A power system undergoes various changes in operating states, thus control parameters are to be varied according to the new states. The classical control and search based heuristic techniques to follow load demand and regulate frequency are presented in [81], [82], [83], [84], [85], [55], [86]. A Fuzzy Genetic Algorithm based sizing and placement strategy has been proposed in [87] for FACTS devices.

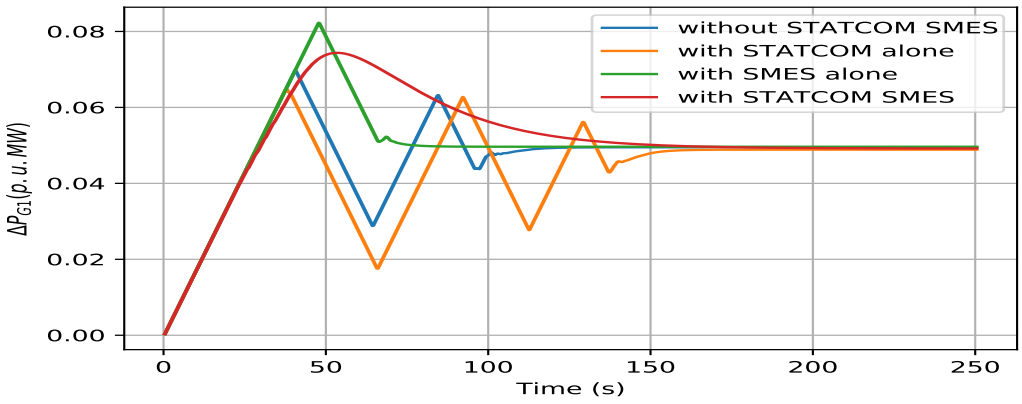

(a) Deviations in Power Generated by Unit 1

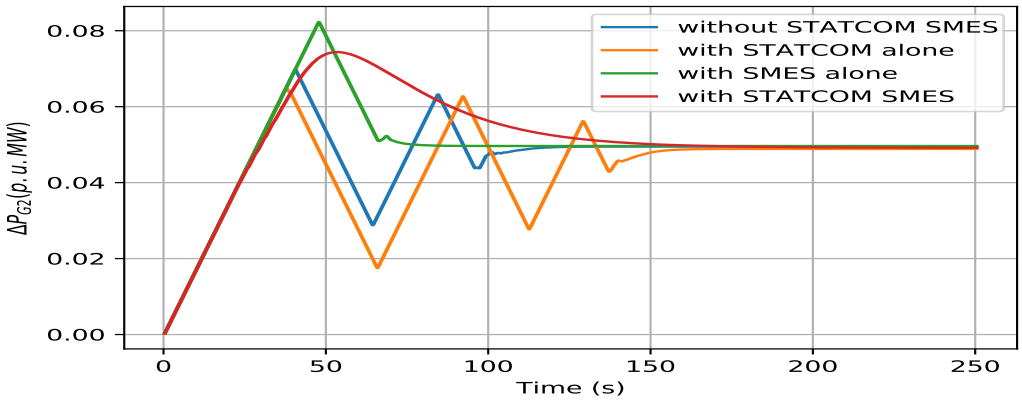

(b) Deviations in Power Generated by Unit 2

Figure 2.16: Power deviations in Area 1 with 0.1 pu MW disturbance.

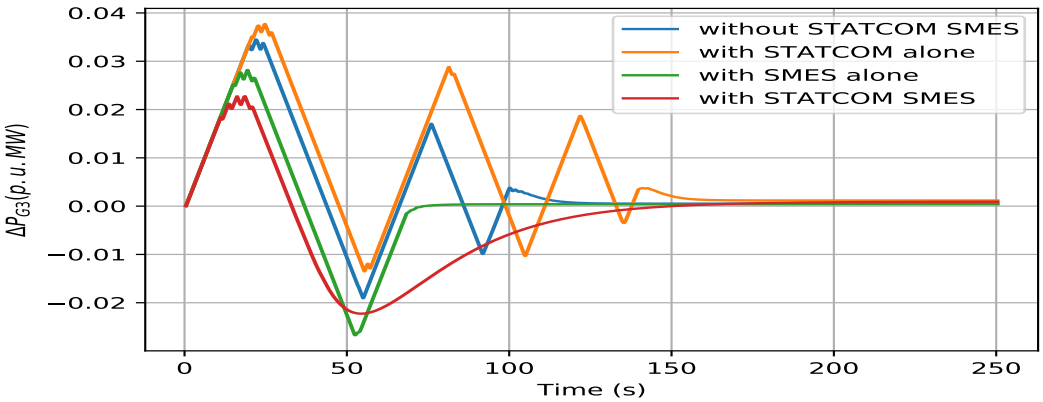

(a) Deviations in Power Generated by Unit 3

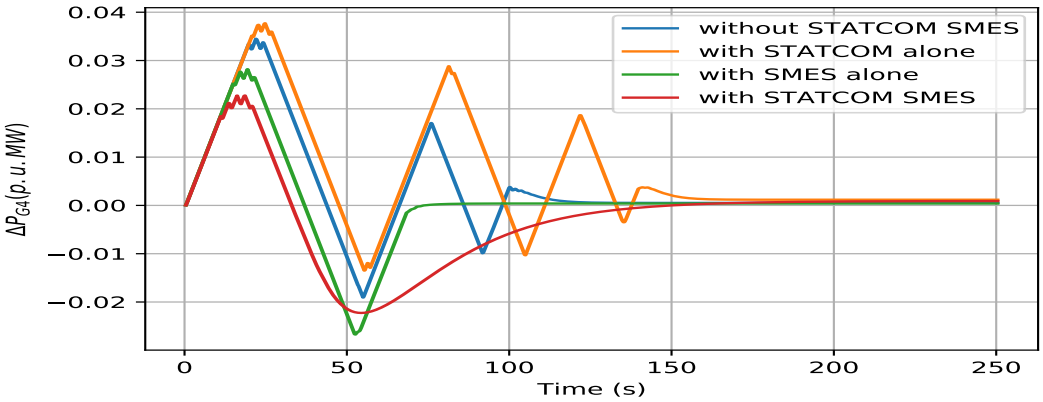

(b) Deviations in Power Generated by Unit 4

Figure 2.17: Power deviations in Area 2 with 0.1 pu MW disturbance.

In [88], moth flame, JAYA hybrid algorithm has been proposed to optimize the line losses. The optimal reactive power dispatch using a harmony search algorithm to improve voltage stability margin has been presented in [89]. However, small-signal stability is not analyzed in [88], [89]. Classical optimization techniques are based on minima-maxima theory under imposed equality non-equality constraints. These techniques tend to find a locally optimal solution rather than a global solution, as they search for points where the slope of the optimization function is zero or move in the direction with the steepest gradient [90]. Enumerative and random search-based methods use all the possible solutions in the search space. While enumerative search selects the solution one by one, random search uses a probabilistic algorithm to take care of searching for the next possible solution point. This creates a trade-

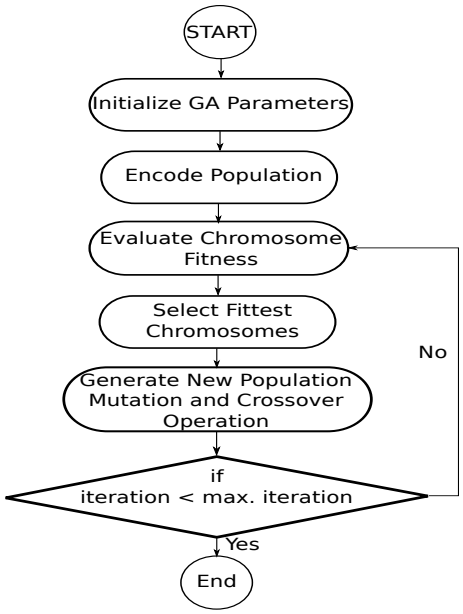

Figure 2.18: Flowchart of Genetic Algorithm

off between solution accuracy and time to obtain a solution. However, these search techniques are applicable for small systems. GA is based on the process of natural selection and evolution, [85], [91]. GA is more robust than other search techniques for the following reasons

1. It uses an encoded set of parameters instead of actual parameters.
2. A set of solutions (population) are used instead of a single solution.
3. It uses probabilistic rules instead of deterministic rules.
4. Compared to other optimization techniques, GA converges.
5. For searching global optimal solutions, GA is better than other search algorithms as it explores the solution space more effectively due to the mutation process.

A comparative performance of various control techniques is done in [92], [93], [94],[95]. Genetic Algorithm (GA), provides a robust optimization for tuning AGC control gains, as it is less sensitive to the power system parameter variations [96],[97]. A random set of possible solutions (population) is generated at the initialization of the algorithm. Later each solution (individual) is encoded in chromosomes. The most common encoding method is binary coding, in which strings of 1 and 0 represent a

Table 2.4: Parameters for Genetic Algorithm

Population	100
Number of Iterations	50
Crossover Rate	0.9
Elite Count	10
Initially Penalty	10
Penalty Factor	100
Mutation Rate	0.001

chromosome. Each chromosome is tested on an objective function, followed by a selection process. The objective function is formulated by Integral Square Error (ISE) with a set of weight constants (w_1, w_2, w_3) as

$$J = \int_0^t (w_1 \Delta f_1(t)^2 + w_2 \Delta f_2(t)^2 + w_3 \Delta P_{tie12}(t)^2) dt \tag{2.51}$$

ISE penalizes large errors heavily by squaring them. Thus larger errors are eliminated quickly. Fitter solutions are selected, and unfit solutions are eliminated through selection. This is followed by crossover and mutation. The crossover creates new solutions by interchanging some genes of specifically chosen chromosomes from the selected pool of solutions. The mutation operator changes a gene in the selected chromosomes and thus generates new chromosomes. The next generation is tested for fitness and henceforth follows the same procedure until the minimum value of the objective function is reached. The parameters used for Genetic Algorithm is presented in Table 2.4.

2.6 Regulated Power System with Solar PV and Battery Energy Storage

Depletion of fossil fuel energy sources with increasing petroleum prices along with climatic concerns has resulted in severe questions on the future of energy. This has led to the development of alternative energy sources and research on increasing the efficiency of various traditional power systems especially integrated with renewable energy sources. In these scenarios, the importance of wind and solar photovoltaic (Solar PV) energy supply has been growing vigorously with increasing concern about the price and availability of fossil fuel and greenhouse gases [98]. In [99], a fuzzy

controller is used to control the PV output in coordination with other generators depending on the load demand for the frequency regulation without energy storage system. In this coordination strategy, the maximum power point tracking (MPPT) control is used for PV power systems, which can derive the maximum output power. In [100], a simple fuzzy-based frequency control method is proposed for the PV generator in a PV–diesel hybrid power system, while [101] has explored the impact of high PV penetration on the inter-area oscillation modes of large-scale power grids. The impacts of adding hybrid renewable energy–based generation on frequency regulation capability of isolated grids have been discussed in [102]. Power generation from solar PV, a renewable source of energy, is increasing at a faster rate which converts sunlight directly into electricity using PV cells. Various energy sources like batteries, ultracapacitors and flywheel energy storage can be used due to the unpredictable and intermittent nature of solar PV system. In this work, we have explored the solar PV along with battery energy storage system (BESS) to supply energy in the wake of sudden loads for achieving better system performance. The thermal generating unit considered is of non-reheat type. A typical value is of 10% /min. The control areas are connected by a tie line. In each area, a linear combination of tie-line power flow deviation (ΔP_{tieij}) and frequency deviation (Δf_i) forms a control signal error, called area control error (ACE_i). This control error signal is monitored by integral controller (K_I) to produce necessary control action and is further fed to the governor that senses machine speed deviation and gives output (P_{Ti}) to adjust the input valve for changing the mechanical power output to re-establish the frequency to its nominal value. The mechanical power input (ΔP_{Gi}), step load change (ΔP_{Di}) and tie-line power flow deviation ($P_{tie_{ij}}$) combine to form a synchronous frequency deviation and determined by generator constant K_{Pi} and T_{Pi} as given by the following equations:

$$\Delta f_1 = \frac{K_{p1}}{1+sT_{p1}}[\Delta P_{G1} - \Delta P_{D1} + a_{12}\Delta P_{tie_{12}}] \tag{2.52}$$

$$\Delta f_2 = \frac{K_{p2}}{1+sT_{p2}}[\Delta P_{G2} - \Delta P_{D2} + \Delta P_{tie_{12}}] \tag{2.53}$$

$$\Delta P_{tie12} = \frac{2\pi T_{12}}{s}[\Delta f_1 - \Delta f_2] \tag{2.54}$$

$$\Delta P_{T1} = \frac{\Delta P_{G1}}{1+sT_{T1}} \tag{2.55}$$

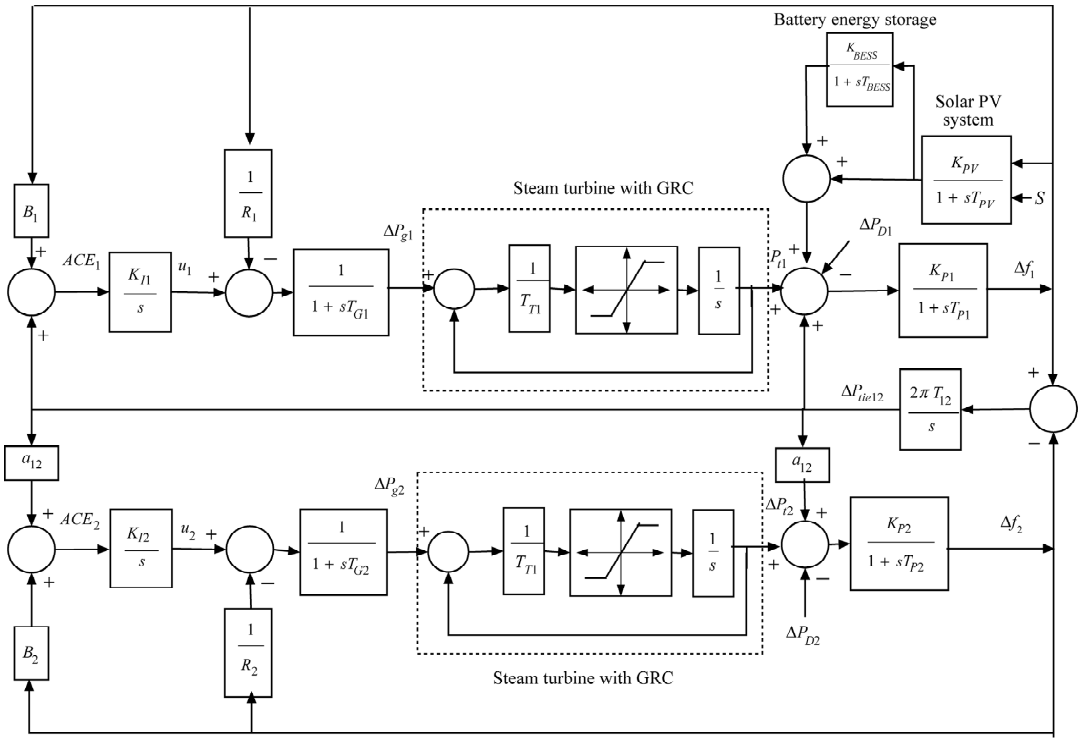

Figure 2.19: Two area power system with Solar PV and BESS

$$\Delta P_{T2} = \frac{\Delta P_{G2}}{1+sT_{T2}} \tag{2.56}$$

$$\Delta P_{G1} = \frac{u_1}{1+sT_{T1}} \tag{2.57}$$

$$\Delta P_{G2} = \frac{u_2}{1+sT_{T2}} \tag{2.58}$$

The sudden demand of power is fulfilled by the combination of solar PV and BESS. Different solar subsystem controllers are explained in [103], [104], [105] to generate power under varying operating conditions. In this paper, system frequency droop control method is used to generate PV power. Whenever solar PV is incapable of supplying energy due to unfavourable climatic conditions, the stored power in the battery will provide power under such deficient conditions. The net power generation from Area-1 with PV and BESS as in Fig. 2.20 is as follows:

$$P_{S1} = \Delta P_{PV} + \Delta P_{BESS} + \Delta P_{G1} - \Delta P_{D1} - \Delta P_{tie12} \tag{2.59}$$

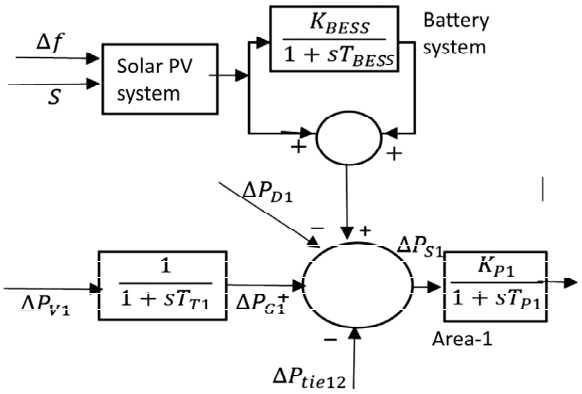

Figure 2.20: Control Block Diagram for Solar PV and BESS Combination

Table 2.5: Integral gain parameters

	K_{i1}	K_{i2}
Without Solar PV Battery System	0.76	0.0132
Solar PV Battery System Area 1 Alone	0.79	0.028
Solar PV Battery System Area 2 Alone	0.77	0.040
Solar PV Battery System in Both Areas	0.88	0.039

In this work, GA is used to tune the integral controller gain settings K_{I1} and K_{I2} with and without solar PV–BESS combination. The flowchart for the GA is depicted in Fig. 2.18. An objective function that takes into account the solar PV power generation change (ΔP_{PV}) in addition to frequency perturbations (Δf_1andΔf_2) and tie-line power deviation ($\Delta P_{tie_{12}}$) is formulated to tune the controller gains as given below

$$J = \int_0^T \Delta f_1^2 + \Delta f_2^2 + \Delta P_{tie12}^2 + \Delta P_{PV}^2 dt \tag{2.60}$$

Solar PV and BESS has been implemented as a linear time-invariant model to improve the frequency and the tie line deviations. The combination of Solar PV and BESS has been placed in area 1, as shown in Fig. 2.19. The integral controller gains are obtained using GA to maintain the small-signal stability. The system responses for a load perturbation of 0.1 p.u. MW is depicted in Fig. 2.21 to Fig. 2.24. It can be seen that with Solar PV and BESS combination, the settling time and peak overshoot of the responses are reduced. The integral controller gain values (K_{i1},K_{i2}) with the combination of PV–BESS in Area-1, Area-2 and in both areas obtained by GA are given in Table 2.5. The regulated system parameters with Solar PV and BESS is presented in Table 2.3[1].

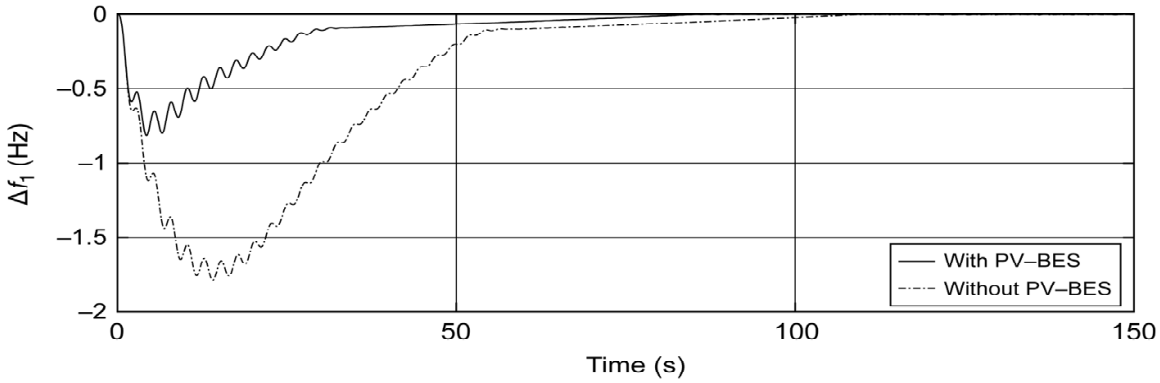

(a) Frequency Deviations in area 1

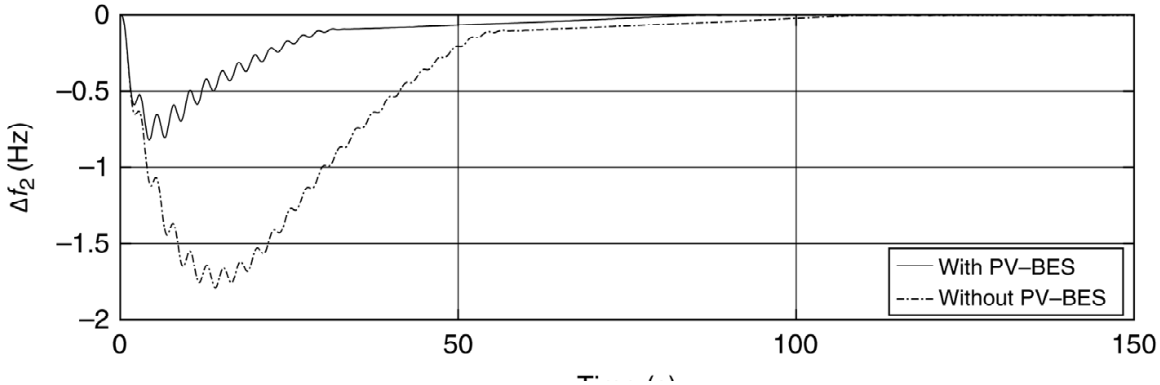

(b) Frequency Deviation in area 2

Figure 2.21: Frequency deviations in Area 1 with 0.1 pu MW disturbance.

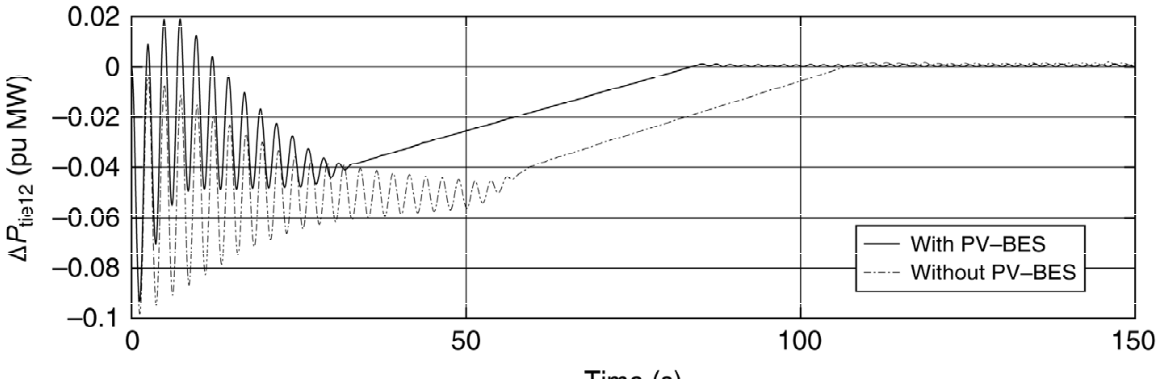

Figure 2.22: Tie line Power deviation with disturbance in Area 1

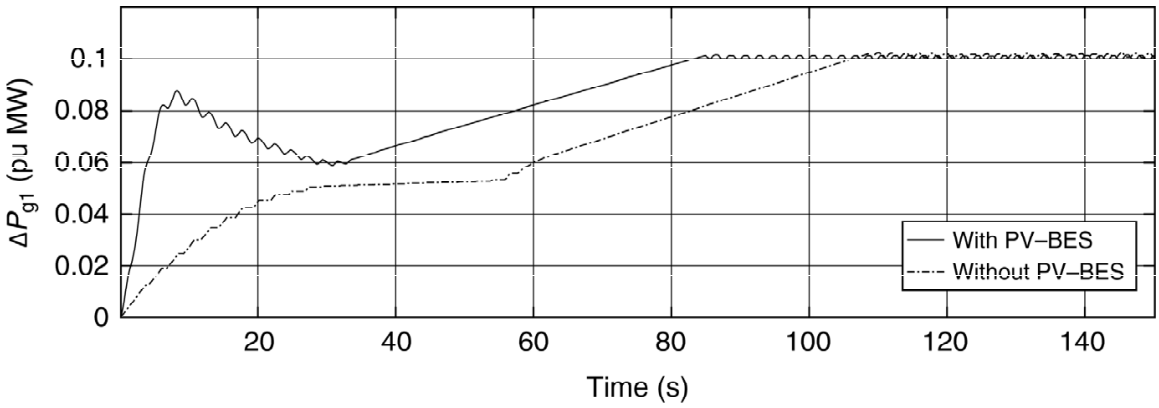

Figure 2.23: Power deviations in Area 1 with 0.1 pu MW disturbance.

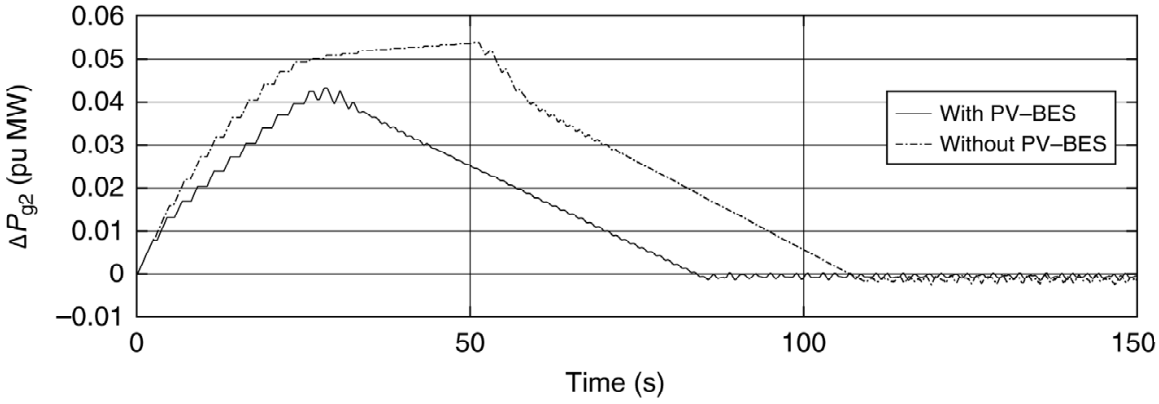

Figure 2.24: Power deviations in Area 2 with 0.1 pu MW disturbance.

.

[1]Rachakonda S.R. Akshay and Rajesh J. Abraham "Load-frequency regulation with solar PV and battery energy storage system". International Journal of Power and Energy Systems, ACTA Press, 2019, 39(1).

2.7 Conclusion

In this work, we have proposed and simulated the combined effect of PV–BESS in improving the frequency of an interconnected power system following a sudden load demand. A linear incremental model of PV and BESS has been used to improve the performance of AGC of two- area interconnected power system. The optimized integral gain values of AGC with and without PV–BESS combinations are obtained using GA. Simulation studies carried out in MATLAB validate that the proposed combination can effectively improve the system frequency in the wake of sudden load disturbances. The effectiveness of PV– BESS in damping out low-frequency oscillations in area frequency and tie-line power flow has been analysed through simulation.

Chapter 3

Load Following in Deregulated Power System

There has been a shift from a regulated framework to a deregulated one since the last few decades to subdue monopoly and encourage competition in the power industry. While doing so, operational, structural and regulatory complications have arisen [106]. The operational complications include ancillary services such as load following, reactive power voltage regulation, energy imbalance services etc. [107]. Regulatory complications involve determining tariffs and prompt fair competition among the participants in the electric power industry.
The generation of each unit in the control areas and the power interchange between control areas are maintained at optimum economic values in deregulated framework by load following as shown in Fig. 3.1 [108]. In [30], deregulated power system with DISCO Participation Matrix (DPM) is introduced which conveys the authorized contract between a DISCO and GENCO under various scenarios.
The STATCOM-SMES combination is placed in area 1. The contracts between GENCOs and DISCOs is represented by DISCO Participation Matrix (DPM), whose entries are the contract participation factors [30]. The parameters used in simulation are given in Table 2.3. The linearized state space equation for the deregulated system is

$$\dot{X} = AX + BU + \Gamma P \tag{3.1}$$

where A, B and Γ are matrices of appropriate dimension.

Each GENCO can participate in load following, meeting the load demands from DISCOs based on an agreed contract which can be visualized as DISCO Participation Matrix [30] as shown below.

$$DPM = \begin{bmatrix} cpf_{11} & cpf_{12} & \dots & cpf_{1n} \\ cpf_{21} & cpf_{22} & \dots & cpf_{2n} \\ : & : & : & : \\ : & : & : & : \\ cpf_{m1} & cpf_{m2} & \dots & cpf_{mn} \end{bmatrix}$$

where contract participation factor, cpf_{ij} is the fraction of the total load from j^{th} DISCO to i^{th} GENCO. The number of rows in DPM correspond to the number of GENCOs and the no of columns in DPM is equal to the number of DISCOs. Sum of the all the entries in a column in this matrix is unity. In our case since there are four GENCOs and DISCOs (m = 4 and n = 4), the DPM is a 4×4 matrix.
The power contracted by the i^{th} GENCO with the DISCOS is

$$\Delta P_{G_i} = \sum_{j=1}^{n} cpf_{ij} \Delta P_{L_j} \tag{3.2}$$

where ΔP_{L_j} = total demand of j^{th} DISCO and cpf_{ij} = contract participation factor.
The scheduled power flow in the tie line at steady state is, $\Delta P_{tie_{12,scheduled}}$ = (Demand of DISCOs in area 2 from GENCOs in area 1) - (Demand of DISCOs in area 1 from GENCOs in area 2). Thus,

$$\Delta P_{tie_{12,scheduled}} = \sum_{i=1}^{m/2} \sum_{j=(n/2)+1}^{n} cpf_{ij} \Delta P_{Lj} - \sum_{i=(m/2)+1}^{m} \sum_{j=1}^{n/2} cpf_{ij} \Delta P_{Lj} \tag{3.3}$$

For the above system, the tie line power error is given as

$$\Delta P_{tie_{12,error}} = \Delta P_{tie_{12,actual}} - \Delta P_{tie_{12,scheduled}} \tag{3.4}$$

At steady state the tie line power error ($\Delta P_{tie_{12},error}$) decays to zero as the actual tie line power ($\Delta P_{tie_{12},actual}$) reaches the scheduled tie line power flow ($\Delta P_{tie_{12},scheduled}$). As in the traditional case, the respective Area Control Error (ACE) signal is generated using this tie line error signal as

$$ACE_1 = B_1 \Delta f_1 + \Delta P_{tie_{12},error} \tag{3.5}$$

$$ACE_2 = B_2 \Delta f_2 + a_{12} \Delta P_{tie_{12},error} \tag{3.6}$$

.

3.0.1 Deregulated Power System Model Assumptions

The majority of the power generating sources comprise the thermal power plants. Thus, ramping control of the thermal power plants plays crucial role in load following. The main components of the thermal generating plant are the governor, the generator and the turbine. Based on the ACE, integral controller changes the governor steam set points in proportion to the area participation factor of the GENCOs. The time taken by governor to act on the updated set point has been represented by a time constant T_G. The turbine time constant T_T represent the time taken by the turbine to change the mechanical power output based on the changed steam input. For improving the efficiency of the power plant, the steam passed through the turbine is recollected and passed through the steam reheat unit. In each area the equivalent model of the generators owned by different GENCOs has been modelled using swing equation as presented in [109]. A Generation Rate Constraint, GRC non linearity of 10% / min [110],[111] has been considered for each of the reheat generating units. For small signal stability study of the system, the load demand from DISCO1, DISCO2, DISCO3 and DISCO4 has been modelled as step load perturbation as 0.1 p.u. MW. The schedule tie line power between the control areas is supplied by transmission lines. The deviation in scheduled tie line power is given as (3.3). ISO is responsible to regulate the load contracted between GENCOs and DISCOs based on DISCO Participation Matrix (DPM). DPM for various Unilateral case, Bilateral case and Contract violation has been presented in Simulation results.

In this section, the effect of STATCOM along with an SMES unit on load following with different contract scenarios- unilateral contract, bilateral contract and contract violation is investigated.

3.1 Unilateral Contract

In the unilateral contract case, since the DISCOs demand power from the GENCOs in the same area the following DPM is considered.

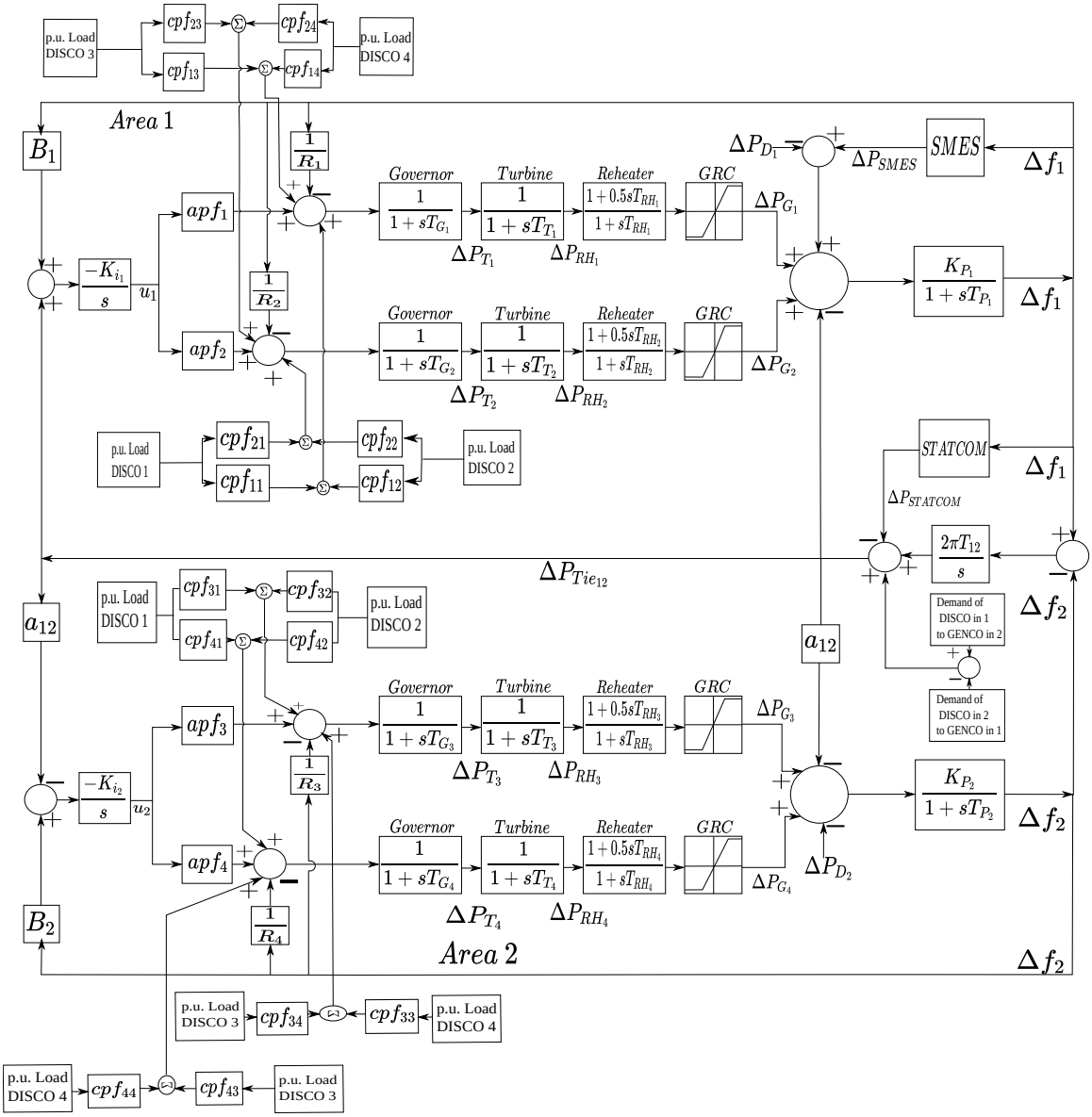

Figure 3.1: Deregulated Power System

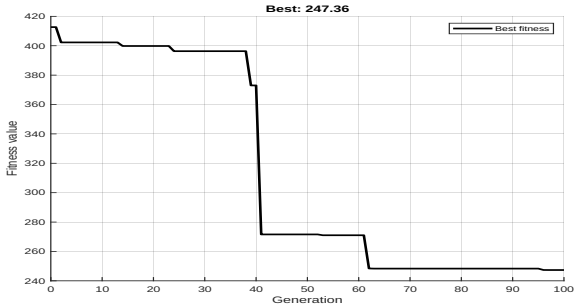

(a)

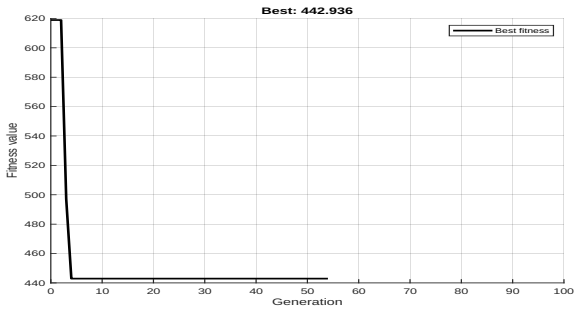

(b)

Figure 3.2: Unilateral contract: (a) with STATCOM SMES (b) without STATCOM SMES

$$DPM = \begin{bmatrix} 0.5 & 0.5 & 0 & 0 \\ 0.5 & 0.5 & 0 & 0 \\ 0 & 0 & 0 & 0 \\ 0 & 0 & 0 & 0 \end{bmatrix}$$

It maybe noted that, as there are no load contracts with DISCOs outside the same area, the remaining rows and columns of DPM are zero. Fig. 3.2 depicts the convergence of fitness value with number of generations for GA. The DISCOs in area 1 have a total load demand of ΔP_{L_1} = ΔP_{L_2} = 0.1 p.u. MW. Fig. 3.3 depicts the deviations in area frequencies. It is evident that, with the STATCOM-SMES combination the frequency deviations are damped out faster and with reduced peak overshoots and undershoots. In unilateral case, at steady state $\Delta P_{tie12,actual}$ = $\Delta P_{tie12,schedule}$ since DISCOS in an area demand power from GENCOS in the same area only. Hence from (11) tie line power error $\Delta P_{tie_{12},error} = 0$. Fig. 3.4 shows the actual tie line power flow in this case which clearly indicates an improvement in the response with STATCOM-SMES combination. The power contracted by the i^{th} GENCO with the DISCOS is

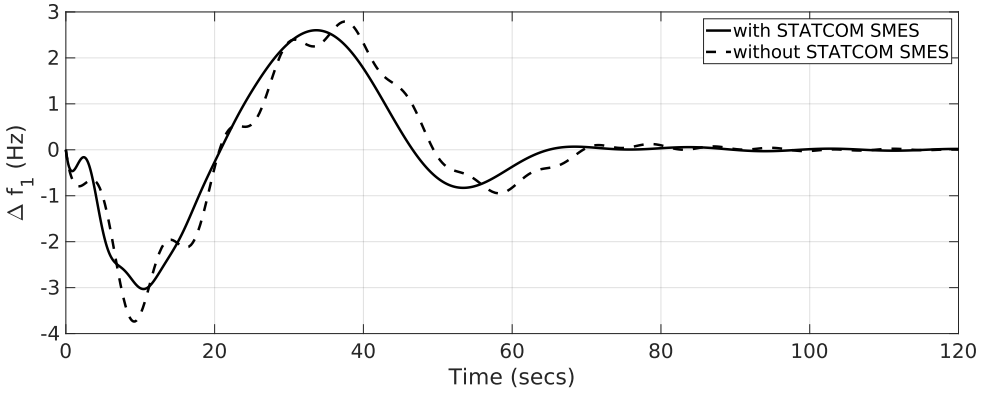

(a) Frequency deviation in Area 1

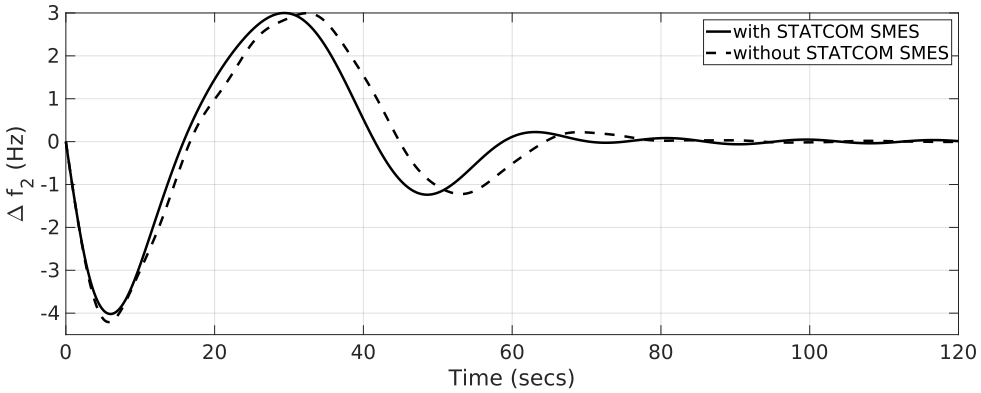

(b) Frequency deviation in Area 2

Figure 3.3: Unilateral Contract: Frequency deviations with disturbance in Area 1 only

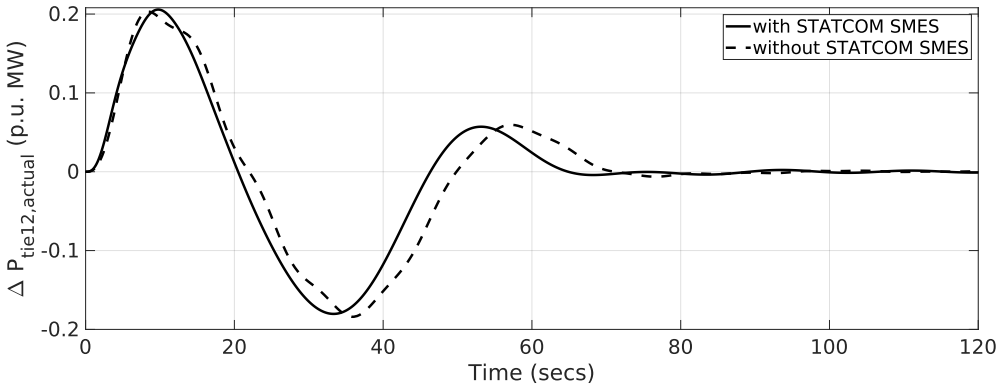

Figure 3.4: Actual tie line power deviation in unilateral contract case

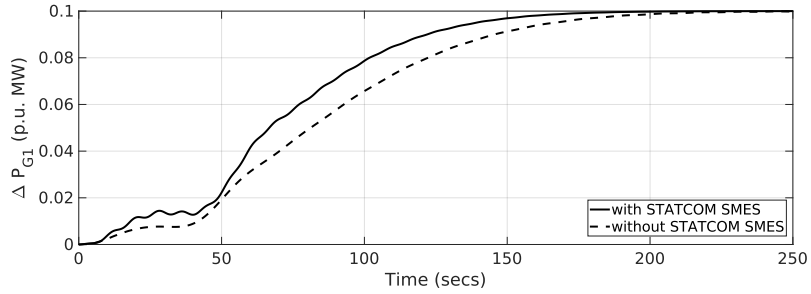

(a)

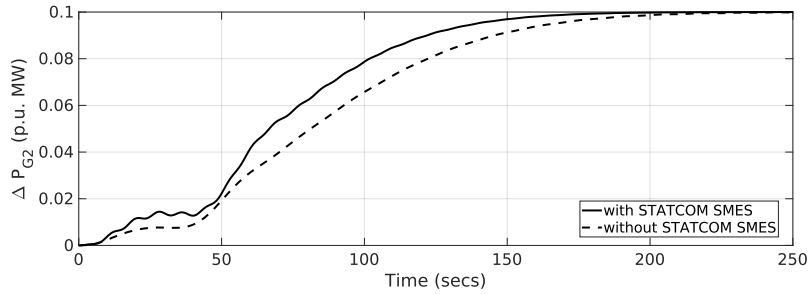

(b)

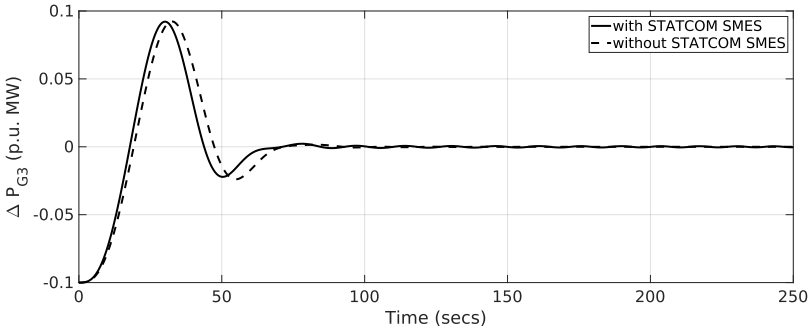

(c)

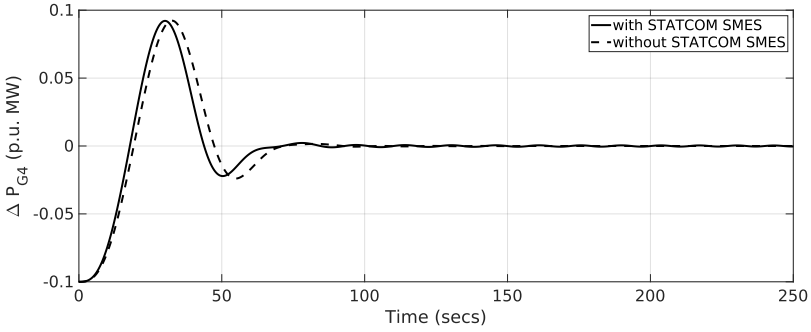

(d)

Figure 3.5: Unilateral contract: Deviations in power generated by (a) GENCO 1 (b) GENCO 2 (c) GENCO 3 (d) GENCO 4

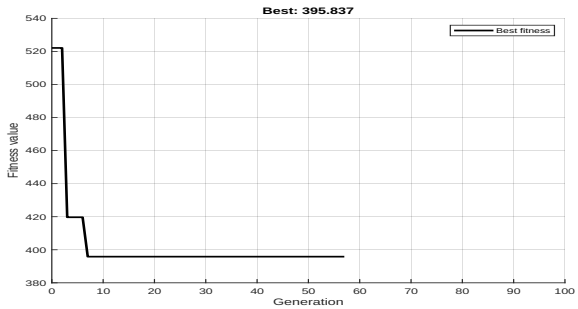

(a)

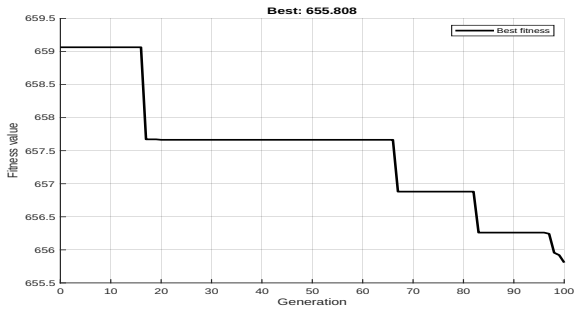

(b)

Figure 3.6: Bilateral contract: (a) with STATCOM SMES (b) without STATCOM SMES

$$\Delta P_{G_i} = \sum_{j=1}^{n} cpf_{ij} \Delta P_{L_j} \tag{3.7}$$

where ΔP_{L_j} = total demand of j^{th} DISCO and cpf_{ij} = contract participation factor. Thus, power generated by GENCO1 is given as $\Delta P_{G_1} = (0.5 \times 0.1) + (0.5 \times 0.1) = 0.1$ p.u MW. Similarly, $\Delta P_{G_2} = 0.1$ p.u. MW and $\Delta P_{G_3} = \Delta P_{G_4} = 0$ p.u. MW. As depicted in Fig. 3.5, ΔP_{G_1} and ΔP_{G_2} settles down to 0.1 p.u. MW each and ΔP_{G_3}=ΔP_{G_4} = 0.

3.2 Bilateral Contract

In bilateral contract, DISCOs can demand power from GENCOs in any area. All the DISCOs have a total load demand of 0.1 p.u. MW each which are contracted to the different GENCOs as per the given DPM.

$$DPM = \begin{bmatrix} 0.2 & 0.25 & 0 & 0 \\ 0.5 & 0.25 & 0 & 0.3 \\ 0.3 & 0.25 & 0 & 0 \\ 0 & 0.25 & 1 & 0.7 \end{bmatrix}$$

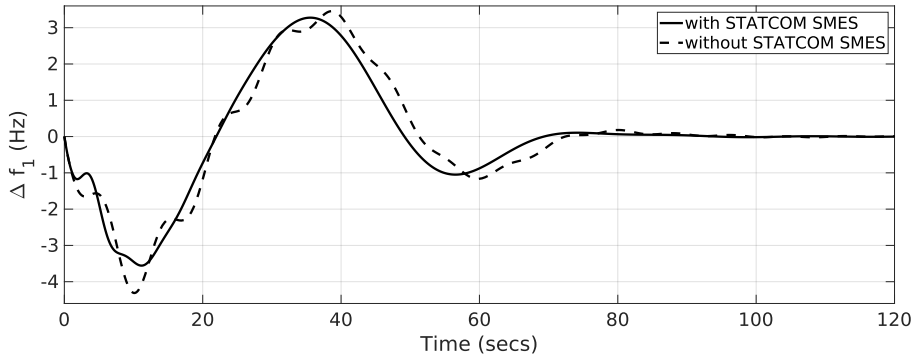

(a) Frequency deviation in Area 1

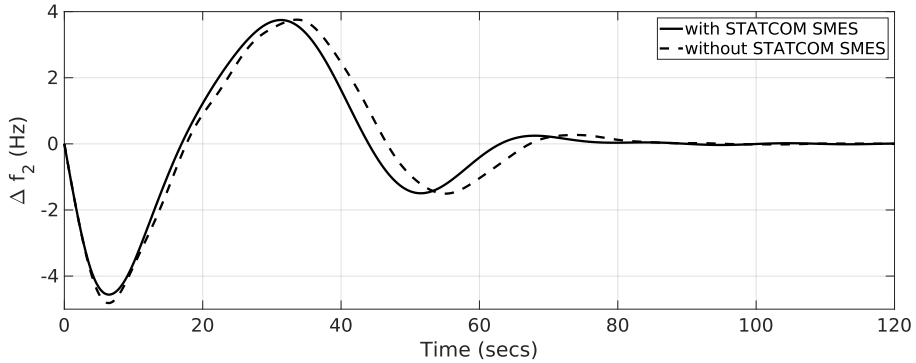

(b) Frequency deviation in Area 2

Figure 3.7: Bilateral contract: Frequency deviation in (a) area 1 and (b) in area 2.

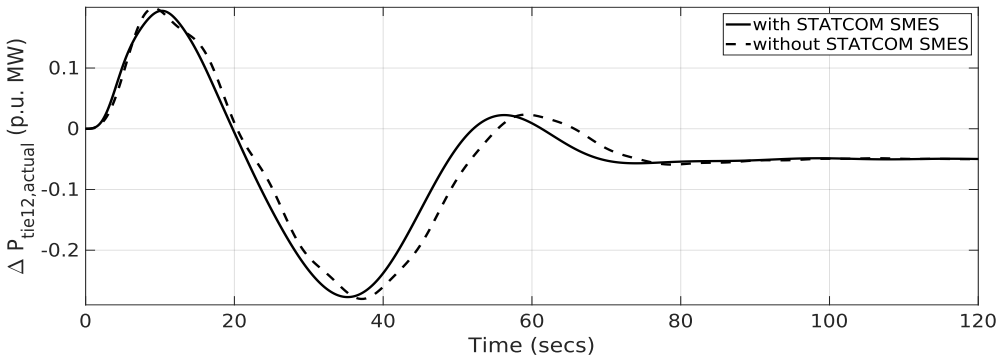

Figure 3.8: Actual tie line power deviation in bilateral contract case

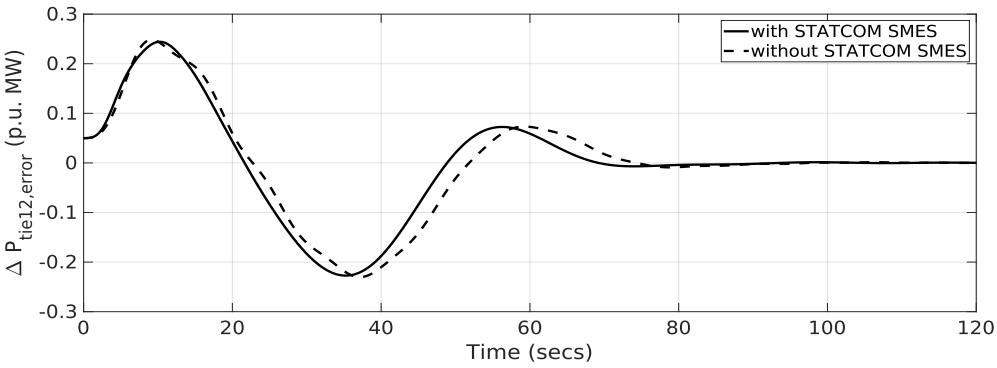

Figure 3.9: Tie line power error deviation in bilateral contract case

The convergence of the fitness value with respect to the number of generations is shown in Fig. 3.6. Fig. 3.7 shows deviations in area frequencies, where as Figs. 3.8 and 3.9 depict the actual tie power flow deviation and tie line power error deviation respectively, where it is observed that the system STATCOM SMES combination has dampened the oscillations quickly with reduced overshoots. In bilateral contract case, actual tie line power deviations follows the scheduled tie line power deviations such that in steady state the tie line power error deviations become zero. The scheduled power flow in the tie line at steady state is, $\Delta P_{tie_{12,scheduled}}$ = (Demand of DISCOs in area 2 from GENCOs in area 1) - (Demand of DISCOs in area 1 from GENCOs in area 2) which is given as

$$\Delta P_{tie_{12,scheduled}} = \sum_{i=1}^{m/2} \sum_{j=(n/2)+1}^{n} cpf_{ij} \Delta P_{Lj} - \sum_{i=(m/2)+1}^{m} \sum_{j=1}^{n/2} cpf_{ij} \Delta P_{Lj} \tag{3.8}$$

For the above system, the tie line power error is given as

$$\Delta P_{tie_{12,error}} = \Delta P_{tie_{12,actual}} - \Delta P_{tie_{12,scheduled}} \tag{3.9}$$

For the assumed DPM, the scheduled tie line power deviation is given as $\Delta P_{tie_{12,scheduled}} = (0 \times 0.1 + 0 \times 0.1 + 0 \times 0.1 + 0.3 \times 0.1) - (0.3 \times 0.1 + 0.25 \times 0.1 + 0 \times 0.1 + 0.25 \times 0.1 = -0.05)$ p.u. MW, which is as shown in Fig. 3.8. The tie line error deviation obtained from (3.4) is presented in Fig. 3.9. The power generation deviations, ΔP_{G_1}, ΔP_{G_2}, ΔP_{G_3} and ΔP_{G_4} are presented in Fig. 3.10. It maybe noted that from (3.2),

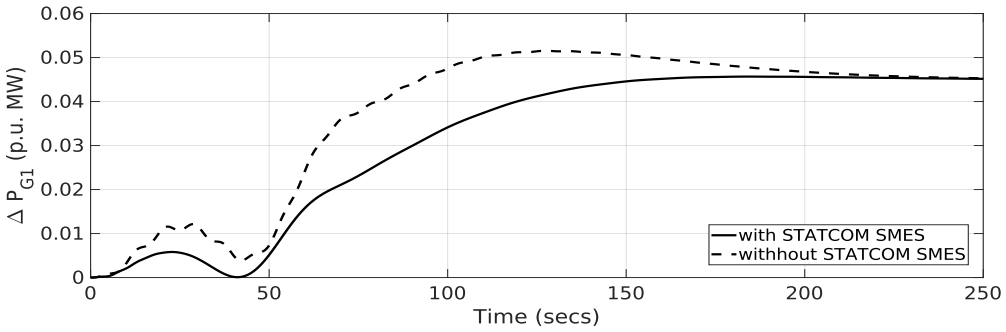

(a)

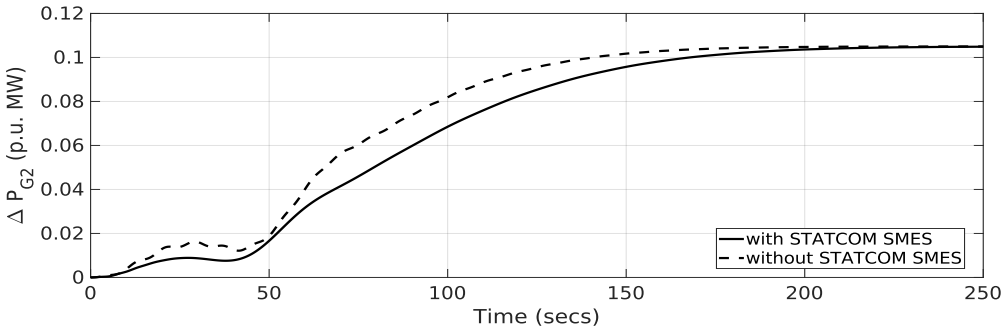

(b)

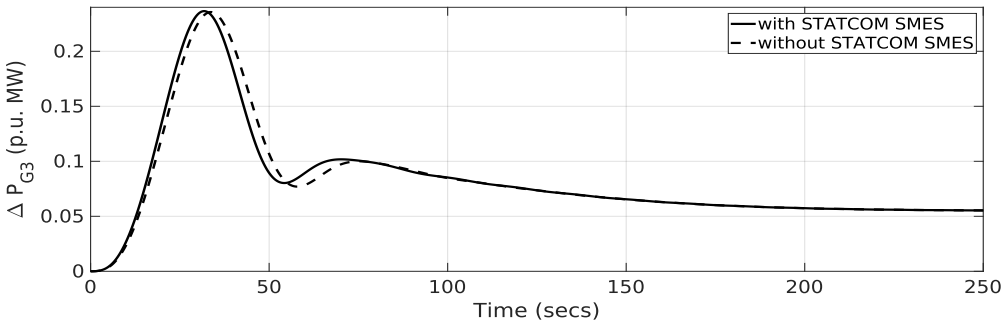

(c)

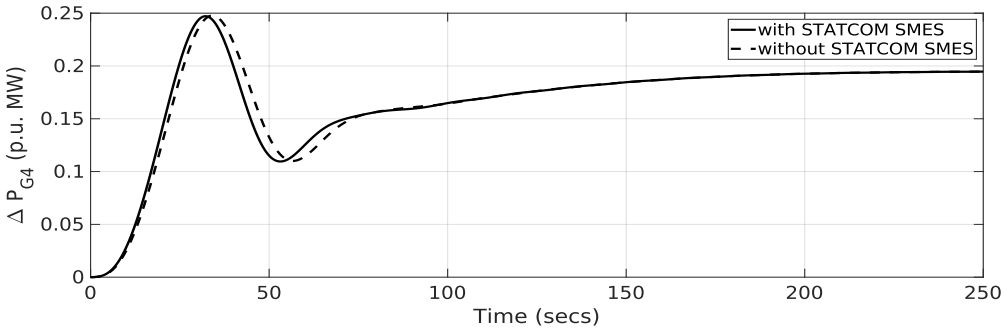

(d)

Figure 3.10: Bilateral Contract: Deviation in power generated by (a) GENCO 1 (b) GENCO 2 (c) GENCO 3 (d) GENCO 4

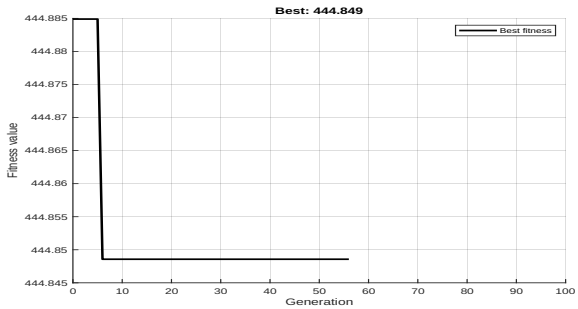

(a)

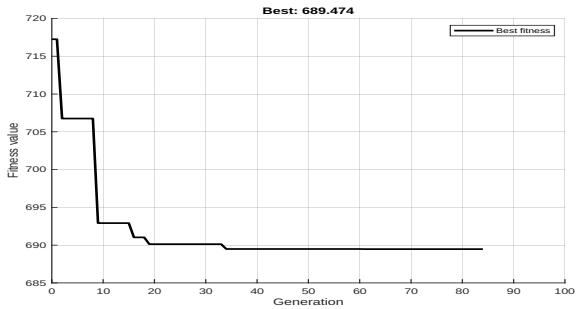

(b)

Figure 3.11: Contract violation: (a) with STATCOM SMES (b) without STATCOM SMES

$\Delta P_{G_1} = 0.2 \times 0.1 + 0.25 \times 0.1 + 0 \times 0.1 + 0 \times 0.1 = 0.045$ p.u.MW. Similarly, $\Delta P_{G_2} = 0.105$ p.u. MW, $\Delta P_{G_3} = 0.055$ p.u. MW and $\Delta P_{G_4} = 0.195$ p.u. MW.

3.3 Contract Violation

In this case, DISCOs in an area demands more load than contracted to the GENCOs. In such case, GENCOs in the same area must meet the uncontracted demand according to their respective ACE participation factors as per the standard industrial practices. Let DISCO1 demand an uncontracted excess power of 0.1 p.u. MW. Therefore, total load in area 1, ΔP_{D_1} = contracted loads of DISCO1 and DISCO2 + uncontracted power of DISCO1 = 0.2 + 0.1 = 0.3 p.u. MW. Likewise, in area 2 the total load ΔP_{D_2} = contracted loads of DISCO3 and DISCO4 = 0.2 p.u. MW. Using the DPM in the bilateral case, GENCO1 in steady state generates ΔP_{G_1} = $cpf_{11}\Delta P_{L1} + cpf_{12}\Delta P_{L2} + cpf_{13}\Delta P_{L3} + cpf_{14}\Delta P_{L4} + apf_1$uncontracted power = 0.095 p.u. MW. Similarly, ΔP_{G_2} = 0.155 p.u. MW. Likewise, in area 2, ΔP_{G_3} = 0.055 p.u. MW and ΔP_{G_4} = 0.195 p.u. MW at steady state. Fig. 3.11 present the fitness value

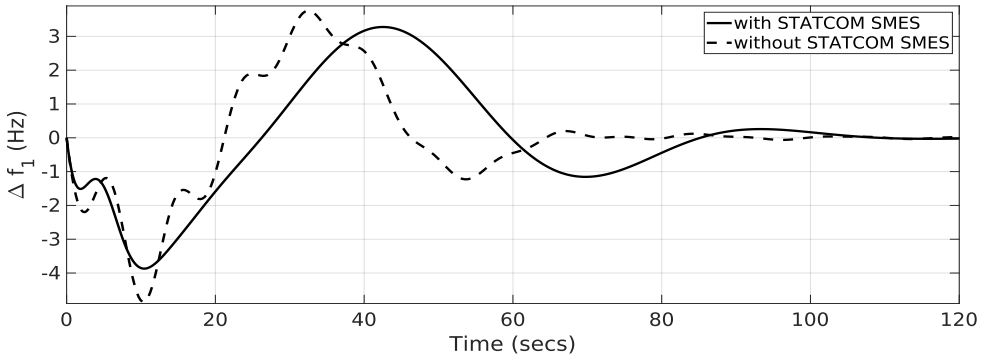

(a) Frequency deviation in Area 1

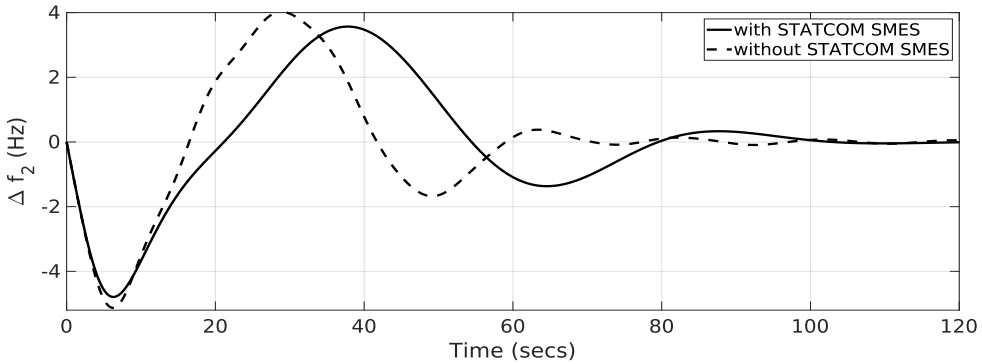

(b) Frequency deviation in Area 2

Figure 3.12: Contract violation: Frequency deviation in (a) area 1 and (b) in area 2.

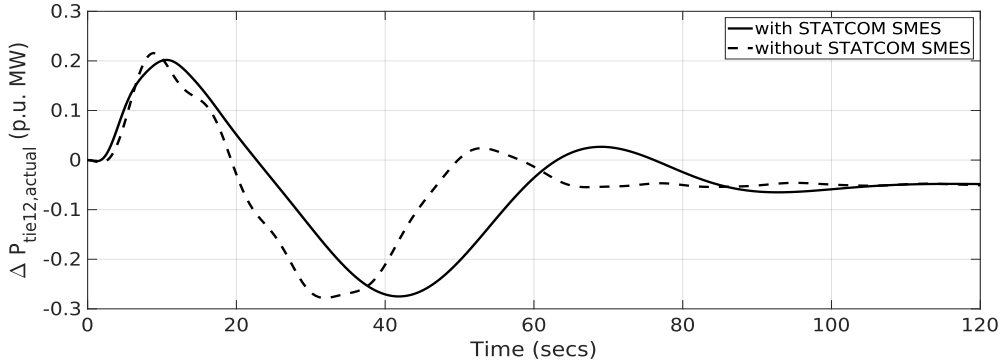

Figure 3.13: Actual tie line power deviation in contract violation case

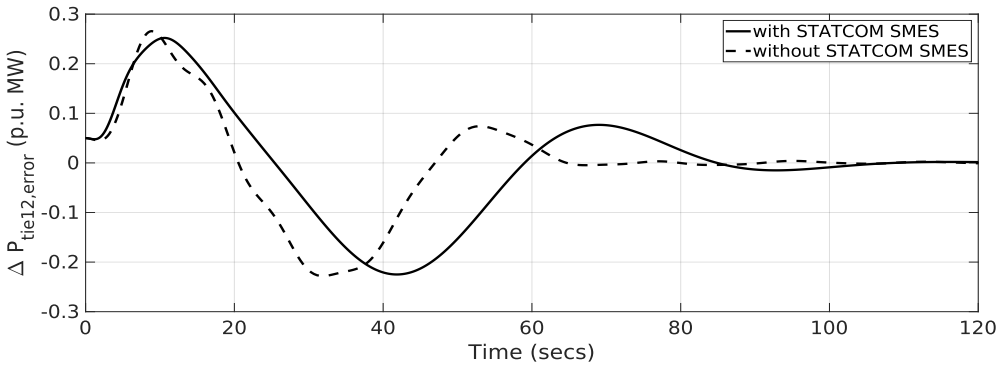

Figure 3.14: Tie line power error deviation in contract violation case

(J) vs. the number of generation plot for contract violation. The different responses in this contract violation case have been plotted in Figs. 3.12 - 3.15 which indicates that combinedly a STATCOM SMES combination has improved the transient and steady state responses.

The excess uncontracted load of DISCO1 has been met by GENCO1 and GENCO2 in the same area at steady state. As shown in Figs. 3.15 (a) and (b), which matches with the calculated value. Further it can be seen that the generations of GENCO3 and GENCO4 are uneffected by the uncontracted load of DISCO1 as seen in Figs. 3.15 (c) and (d)[1].

3.4 Conclusion

This chapter investigated the application of STATCOM-SMES in a deregulated two area power system. STATCOM has been controlled to regulate reactive power in the tie line. SMES compensates the sudden load demand occurs, improving the dynamic stability of the system. The peak drop in frequency and the frequency oscillations have been reported to be minimised with STATCOM-SMES. The tie line oscillations with STATCOM- SMES are damped out effectively under contract violation and unilateral cases, but in bilateral case the STATCOM control results in higher oscillations. The control area integral gains are optimised by Genetic Algorithm.

[1]Rachakonda Shri Rama Akshay & Rajesh Joseph Abraham. "Load following performance in a deregulated power system with static synchronous compensator and super magnetic energy storage". Energy Systems. 2022 May 13:1-20.

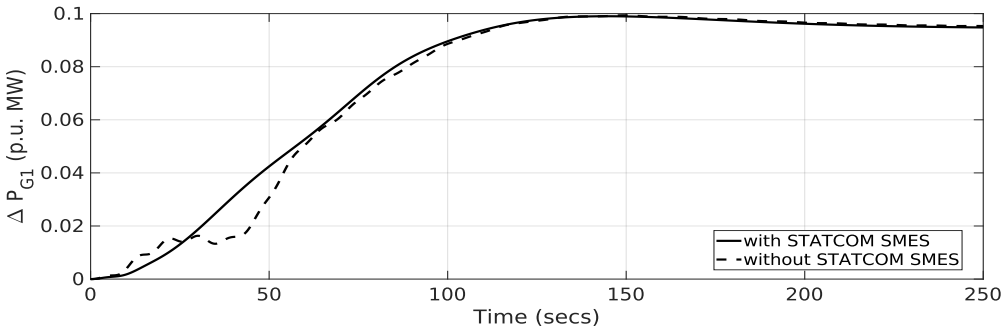

(a)

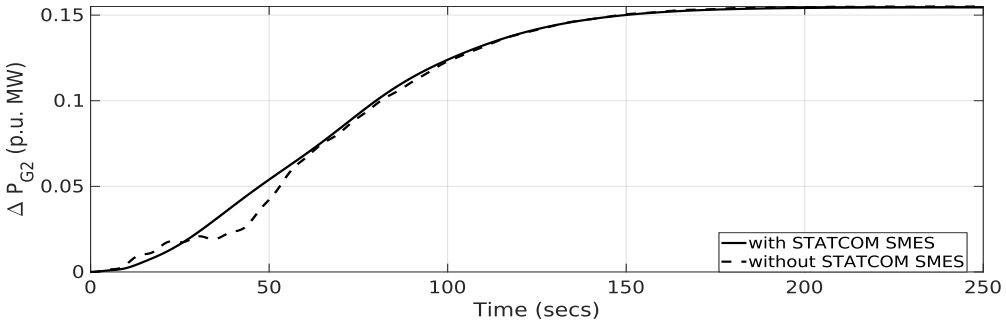

(b)

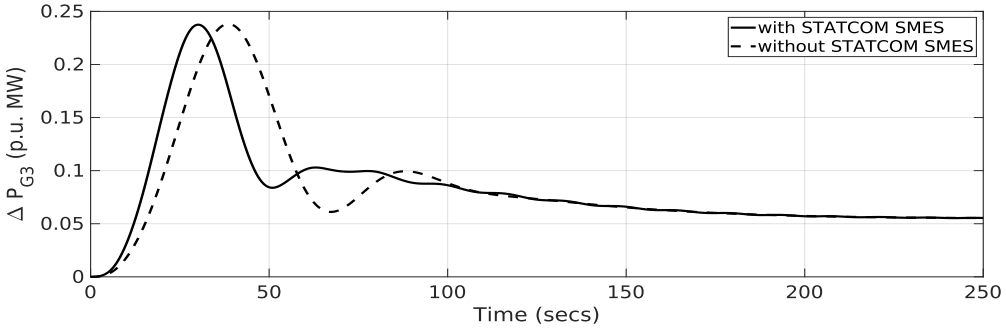

(c)

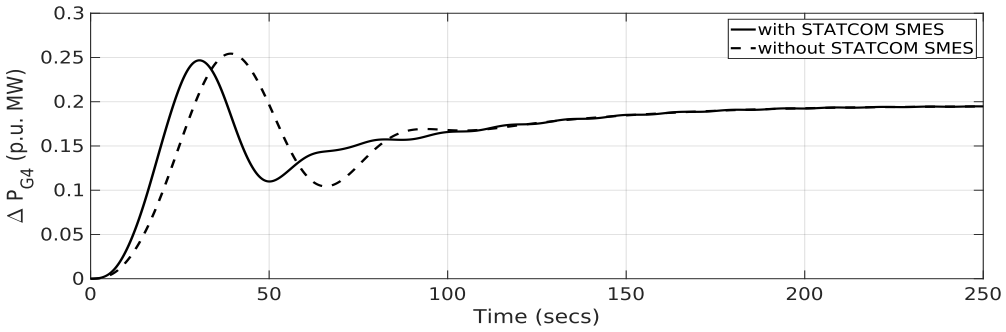

(d)

Figure 3.15: Contract Violation : Deviation in power generated by (a) GENCO 1 (b) GENCO 2 (c) GENCO 3 (d) GENCO 4

Chapter 4

Converter Modelling and Control

Systems with at least one semiconductor switch and passive elements and/or active elements (Resistors, Capacitors, Inductors) are termed as power electronic converters. The power electronic converters are classified as current source converter (CSC) and voltage Source converter (VSC) based on the DC side source. In recent years, the VSCs have facilitated power conversion and grid integration of the renewable energy sources and FACTS controllers. In this chapter, the mathematical models of the VSC based systems are to be investigated. To meet design challenges, suitable power switching devices are chosen. For full control, high voltage applications such as Static Var Generator (SVG), Back to Back connection (BTB), Traction Propulsion System, high voltage inverter Gate Thyristor Off (GTO) modules are preferred (maximum ratings 4.4 KV , 4000 A) [112]. GTOs are phase controlled bipolar unidirectional device. High voltage IGBT modules are also available which are bidirectional unipolar Pulse Width Modulation (PWM) devices. PWM reduces the harmonics in the grid with higher switching frequency devices. This chapter presents large signal models of the VSC that is implemented for the FACTS devices, energy storages and grid integrated renewable sources. In section 4.1, the mathematical model for phase control of VSC is presented. Sine PWM model of VSC is analyzed in section 4.2. Modelling and control of Battery Energy Storage, Super Magnetic Energy Storage, Static Compensator, Solar PV are presented in the following sections.

4.1 Phase Controlled VSC

The mathematical model of a two level GTO based VSC connected to a three phase grid with 180^o conduction mode is investigated in [6]. VSC without an active power

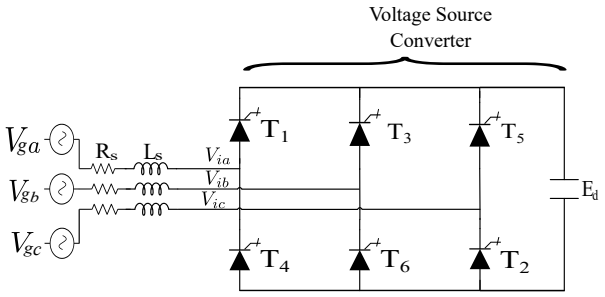

Figure 4.1: Two level VSC circuit diagram

source can be controlled as an impedance load. The first order equations are given as

$$v_{ga} = v_{ia} + i_a R_s + L_s \frac{di_a}{dt} \tag{4.1}$$

$$v_{gb} = v_{ib} + i_b R_s + L_s \frac{di_b}{dt} \tag{4.2}$$

$$v_{gc} = v_{ic} + i_c R_s + L_s \frac{di_c}{dt} \tag{4.3}$$

$$C \frac{de_d}{dt} = i_{dc} \tag{4.4}$$

$$i_{dc} = \frac{1}{e_d}(s_a i_a + s_b i_b + s_c i_c) \tag{4.5}$$

where v_{gk}, and v_{ik} represent the grid and VSC terminal voltages respectively, i_k are the grid currents and s_k are the switching states of the switches $(T_1, T_2, T_3, T_4, T_5, T_6)$ as depicted in Fig. 4.1. Each leg of a VSC is denoted by k. The switching state for leg a is shown in Fig. 4.2. The switching states for leg b and leg c are given as

$$s_b = s_a(\omega t - \frac{2\pi}{3}) \tag{4.6}$$

$$s_c = s_a(\omega t + \frac{2\pi}{3}) \tag{4.7}$$

The state variables of the converter model are given as $x = [i_a, i_b, i_c, e_d]^T$. In this model, the converter is connected to an infinite bus, thus, grid voltage magnitude and the phase angle is constant. The grid voltages are given as

$$v_{ga} = V_m sin(\omega t) \tag{4.8}$$

$$v_{gb} = V_m sin(\omega t - \frac{2\pi}{3}) \tag{4.9}$$

$$v_{gc} = V_m sin(\omega t + \frac{2\pi}{3}) \tag{4.10}$$

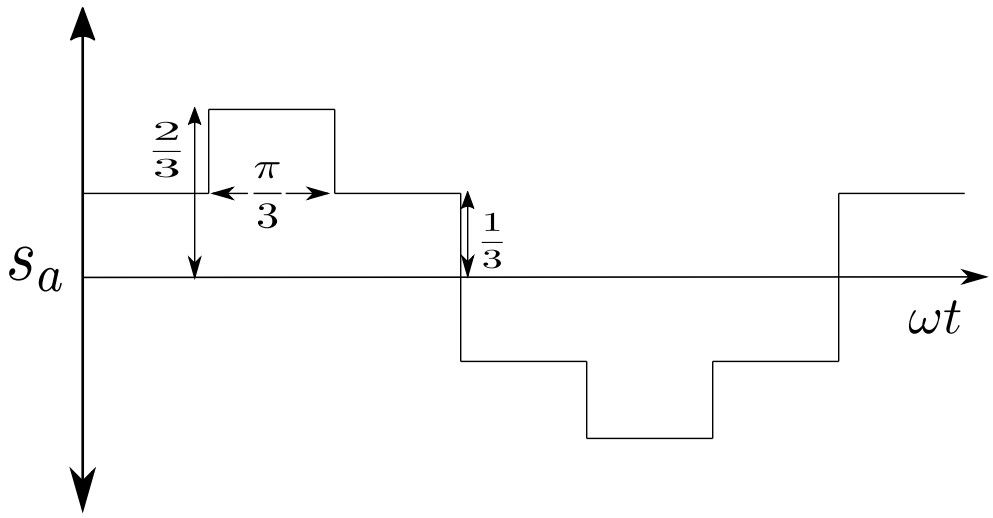

Figure 4.2: Switching state s_a for leg a [6]

The terminal voltage of the converter is a function of the switching states. From Fourier series, the terminal converter voltages are given as

$$v_{ia} = \sum_{n=6m\pm1} \frac{2e_d}{n\pi} sin(\omega t + \alpha) \tag{4.11}$$

$$v_{ib} = \sum_{n=6m\pm1} \frac{2e_d}{n\pi} sin(\omega t + \alpha - \frac{2\pi}{3}) \tag{4.12}$$

$$v_{ic} = \sum_{n=6m\pm1} \frac{2e_d}{n\pi} sin(\omega t + +\alpha + \frac{2\pi}{3}) \tag{4.13}$$

where m is an integer number and α is the firing angle of GTO. From the fundamental components of converter terminal voltages the numerical solution of the nonlinear first order equations are obtained by solving (4.1) to (4.5).

4.2 Sine PWM controlled VSC

In the previous section, firing angle controls the terminal voltage of VSC, however, the conduction period of the switches were fixed at 180^o conduction mode. The harmonics introduced due to this conduction method is very high and given as $6m \pm 1$, where m is the integer number. Thus, to reduce harmonics PWM technique are introduced. Sinusoidal PWM is a popular technique to reduce harmonics and switching losses. It is easy to implement and widely used in power electronics converter control [113]. The output harmonics are give as $mF + nf$, where m, n are integers and F is

the carrier wave frequency and f is the reference wave frequency. As a result of high switching frequency (F), the harmonics are of higher order and easier to filter out. However, the maximum voltage under linear range (under modulation) is reduced to 78.5 % compared to 180^o conduction mode. As a consequence of changing switching technique, the switching function s_{kj} are given as

$$s_{kj} = \begin{cases} 1 & \text{if} \quad \text{switch}_{kj} \quad \text{closed} \\ 0 & \text{if} \quad \text{switch}_{kj} \quad \text{open} \end{cases}$$

where $k = a, b, c$ is the converter leg and $j = 1, 2$ represents top or bottom switch as shown in Fig. 4.3 . For switching frequency significantly higher than grid frequency, the converter circuit model can be averaged over the switching period [114]. The converter terminal voltage measured from converter neutral point N, is given as

$$v_{aN} = \begin{cases} \frac{e_d}{2} & \text{if} \quad \text{switch}_{a1} \quad \text{closed} \\ \frac{-e_d}{2} & \text{if} \quad \text{switch}_{a1} \quad \text{open} \end{cases}$$

The converter terminal voltages measured from grid neutral point (n) is given as

$$\begin{aligned} v_{ia} &= \frac{2v_{aN} - v_{bN} - v_{cN}}{3} \\ v_{ib} &= \frac{2v_{bN} - v_{aN} - v_{cN}}{3} \\ v_{ic} &= \frac{2v_{cN} - v_{cN} - v_{aN}}{3} \end{aligned} \tag{4.14}$$

The fundamental voltage component of a voltage source converter output is given as

$$\begin{aligned} v_{ia0} &= \frac{e_d}{2} m_i sin(\omega t) \\ v_{ib0} &= \frac{e_d}{2} m_i sin(\omega t - \frac{2\pi}{3}) \\ v_{ic0} &= \frac{e_d}{2} m_i sin(\omega t + \frac{2\pi}{3}) \end{aligned} \tag{4.15}$$

where m_i is the modulation index. From Park's transformation, the three phase grid voltages and the converter fundamental voltages are transformed to two constant

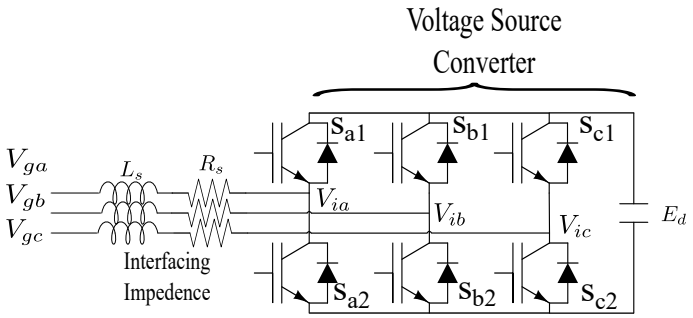

Figure 4.3: PWM converter

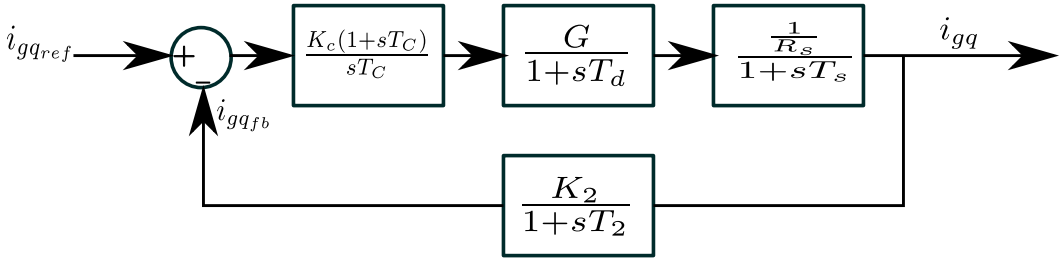

Figure 4.4: VSC current controller [7]

vectors aligned to $d-q$ axis given as

$$\begin{aligned}
V_{gd} &= \frac{2}{3}(v_{ga}sin(\omega t) + v_{gb}sin(\omega t - \frac{2\pi}{3}) + v_{gc}sin(\omega t + \frac{2\pi}{3})) \\
V_{gq} &= \frac{2}{3}(v_{ga}cos(\omega t) + v_{gb}cos(\omega t - \frac{2\pi}{3}) + v_{gc}cos(\omega t + \frac{2\pi}{3})) \\
V_{id} &= \frac{2}{3}(v_{ia0}sin(\omega t) + v_{ib0}sin(\omega t - \frac{2\pi}{3}) + v_{ic0}sin(\omega t + \frac{2\pi}{3})) \\
V_{iq} &= \frac{2}{3}(v_{ia0}cos(\omega t) + v_{ib0}cos(\omega t - \frac{2\pi}{3}) + v_{ic0}cos(\omega t + \frac{2\pi}{3}))
\end{aligned} \tag{4.16}$$

where v_{gk} and v_{ik} are grid and converter terminal voltages respectively. The grid equations transformed to $d-q$ axis are given as

$$\begin{aligned}
V_{gd} &= V_{id} + i_{gq}\omega L_s + L_s\frac{di_{gd}}{dt} + i_{gd}R_s \\
V_{gq} &= V_{iq} - i_{gd}\omega L_s + L_s\frac{di_{gq}}{dt} + i_{gq}R_s
\end{aligned} \tag{4.17}$$

where i_{gk} is the Park's transformation of grid current. VSC sine PWM has an outer DC link voltage control loop and an inner current control loop. The current controller is presented in Fig. 4.4.

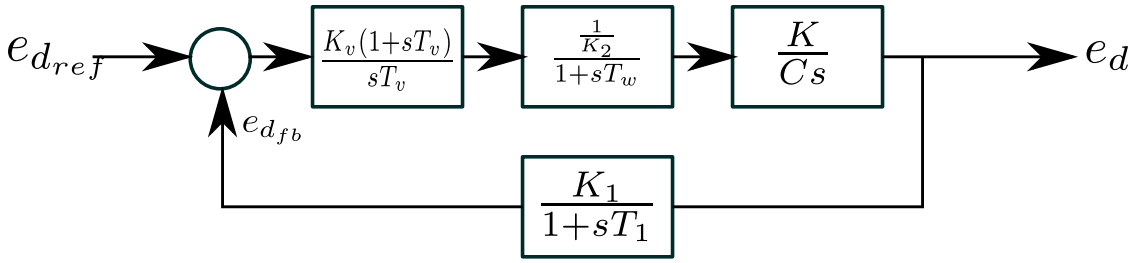

Figure 4.5: VSC DC link voltage controller [7]

4.2.1 Current Controller

The linear time invariant model of converter is given as gain G and time constant T_d. The time delay depends on the switches turn on and turn off time. The carrier signal period T_{sw} is chosen such that $T_d \leq \frac{T_{sw}}{2}$. The inductance and resistance of the inductive coil or transformer interfacing the converter to the gird is given as R_s, L_s. The time constant associated to the inductive coil or the transformer leakage inductance is given as T_s. The gain and time constant of the current sensor is given as K_2, T_2. The controller parameters T_c is taken such that $T_c = T_s$. And the gain K_c is selected for 5 % overshoot. The operating time of the current controller must be designed lower than the voltage controller [115].

4.2.2 Voltage Controller

The schematic diagram of a DC link voltage controller of VSC is depicted in Fig. 4.5. As the bandwidth of the voltage controller is lower than the current controller, the current controller can be approximated to a linear transfer function with gain $\frac{1}{K_2}$ and time constant $T_w = 2(T_d + T_s)$. The PI voltage controller gain and time constant is given as K_v, T_v. Assuming loss free converter, the power at the DC link and AC side of converter is equal which is given as

$$i_{dc} = \frac{2}{3E_d} v_{gq} i_{gq} = K i_{gq} \tag{4.18}$$

The relation between grid q axis current and the DC link current is denoted by K. The output of the controllers are converted to three phase quantities, which act as modulating waves for sine PWM.

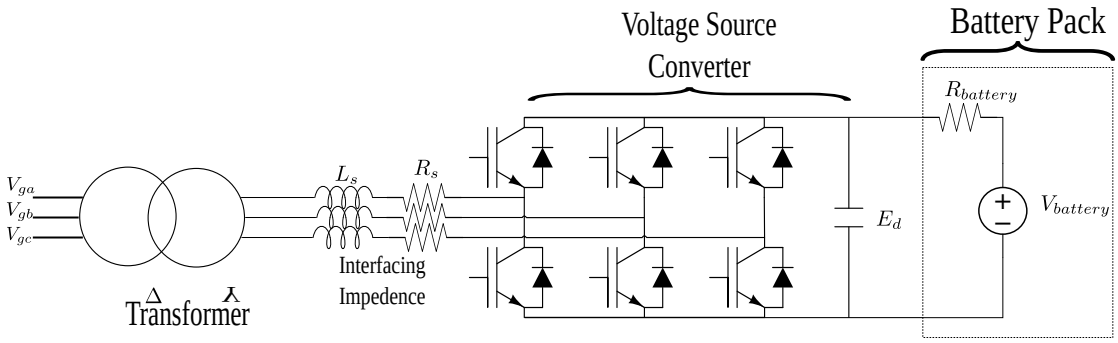

Figure 4.6: Battery Energy Storage System Model

4.3 Battery Energy Storage System Model

Battery Energy Storage System (BESS) constitutes an energy source (battery pack) and a power converter. The selection of the battery pack depends on several constraints among which capacity, cost, lifetime, charging - discharging, thermal, system reliability and environmental constraints are critical [116]. BESS has been modelled as a zero order circuit as shown in Fig. 4.6. This model consists of a DC voltage source in series with a resistor. This model is sufficient to portray the steady state performance of the BESS [117]. The objective of bi directional active power flow control is to regulate DC link capacitor voltage E_d. During charging period of battery pack $V_{battery}$ is lower than E_d and during discharging period the magnitude of E_d is controlled less than $V_{battery}$. The active power exchange between BESS and grid is controlled by DC link voltage controller. For participation of BESS in load frequency regulation the DC link voltage reference $\Delta e_{d_{ref}}$ is given by droop method as shown in Fig. 4.7. The droop method is an auxillary control implemented along with DC link voltage control. From Fig. 4.7 ΔP_{BESS} represents the maximum power limit BESS can provide for frequency regulation. The control block diagram of BESS is shown in Fig. 4.8. BESS output current with respect to the grid voltage is shown in Fig. 4.9. The power drawn from BESS is used to charge BESS. From 1 sec the reference of BESS is changed to discharging mode and the current is 180^o out of phase of grid voltage.The bidirectional power flow from the BESS is depicted in Fig.4.10. The simulation parameters for average switch modelling is presented in Table 4.1.

From ΔP_{BESS}, the voltage reference can be obtained as

$$\Delta e_d^{ref} = \frac{R_{Battery}\Delta P_{BESS}}{2E_{do} - V_{Battery}} \tag{4.19}$$

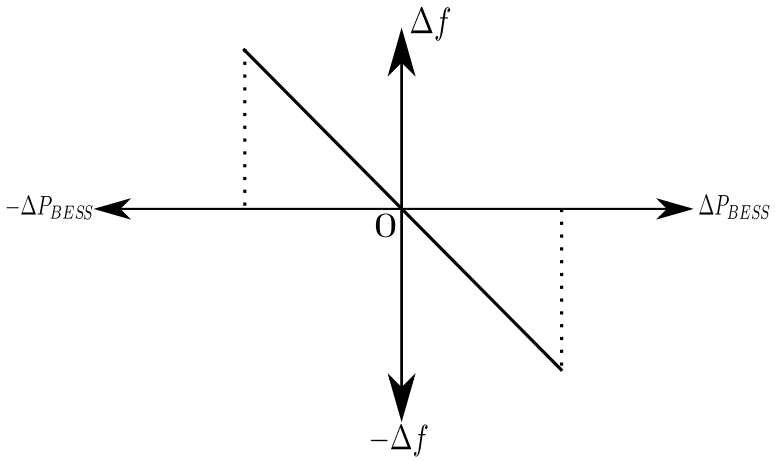

Figure 4.7: Battery Energy Storage System Model frequency regulation

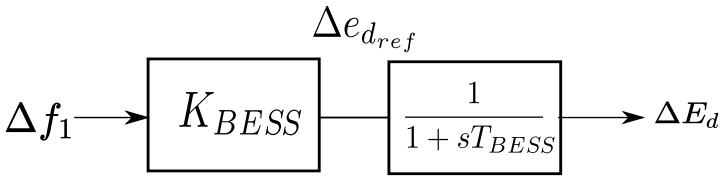

Figure 4.8: Battery Energy Storage System Model frequency regulation control block diagram

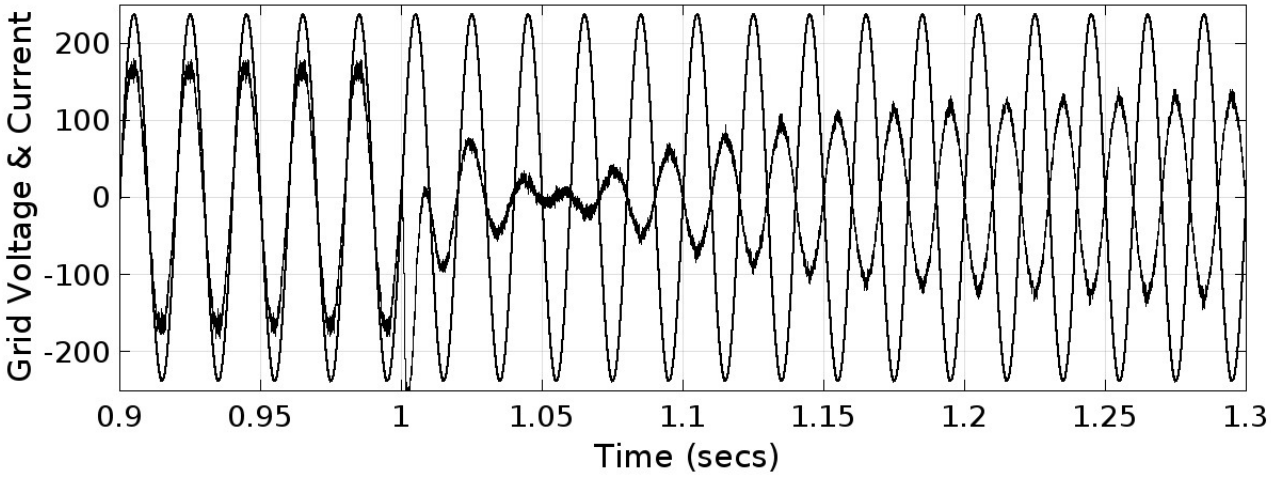

Figure 4.9: Grid voltage and current with BESS

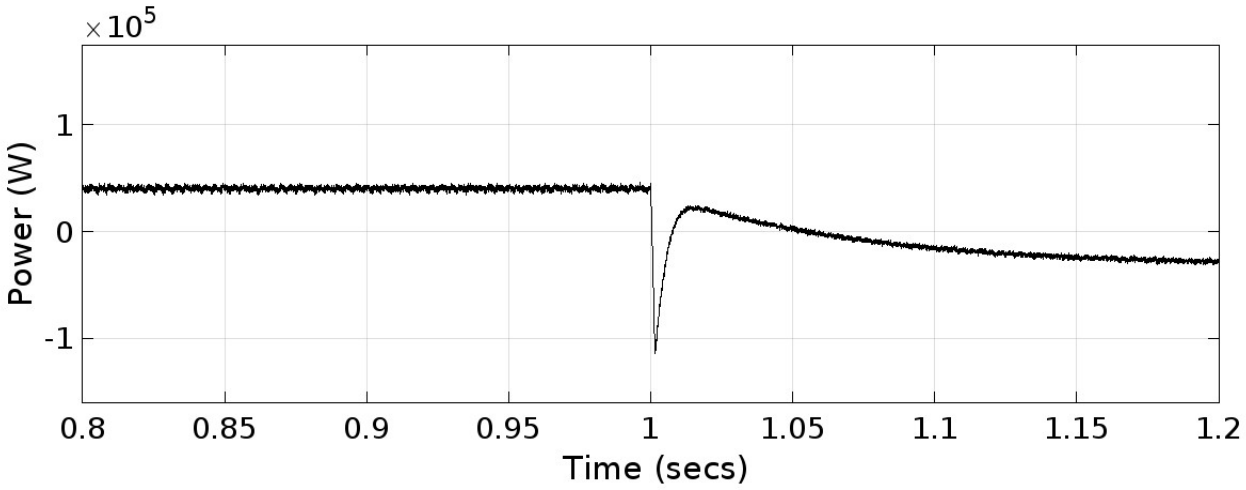

Figure 4.10: Active Power output from BESS

Table 4.1: Simulation Parameters for BESS

Simulation Parameters for BESS	
Parameter	Value
Battery Internal Resistance	1 Ω
DC link Capacitance	6750 μ F
Transformer Size	900 kVA
Transformer Primary	230 kV
Grid Voltage	290 V

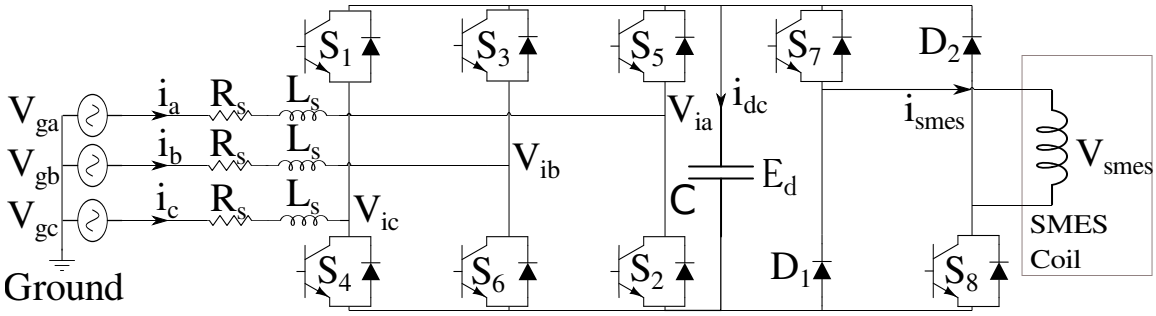

Figure 4.11: Circuit diagram of SMES

4.4 Super Magnetic Energy Storage

An SMES consists of a super conducting magnetic energy coil and a power electronic interface for grid connection. SMES coil current is inductive, thus there is no change in DC coil current transients due to power electronic switching. The inductive coil stores the electromagnetic energy which is kept at cryogenic temperature around 20 K [36]. DC-DC converter across SMES coil controls the direction of power flow between SMES and grid as shown in Fig. 4.11.

The output power deviation is given as

$$\Delta P_{SMES} = \Delta E_d I_o \tag{4.20}$$

where I_o is the inductive coil current. ΔE_d is the incremental voltage change across SMES coil. By controlling DC DC converter across SMES coil, the bidirectional power flow is achieved. Similar to the droop control in BESS, the required ΔP_{SMES} is calculated from the frequency deviation Δf. The small signal of SMES control is shown in Fig. 4.12.

SMES average switch modelling has been done for the dynamic studies in MATLAB/Simulink. The grid connected SMES can be controlled to operate in bidirectional power flow mode. Fig. 4.13 shows that the DC current through the SMES is constant. The charging and discharging current from the SMES is presented in Fig. 4.14. It can be noted from Fig. 4.14 and Fig. 4.16 that in charging mode when SMES act as load, i.e. when grid voltage and current drawn by SMES are in phase the active power from the grid source is high while. However, in discharging mode when SMES act as power source the active power from the grid source reduces. The parameters used for average switch modelling is presented in Table 4.2.

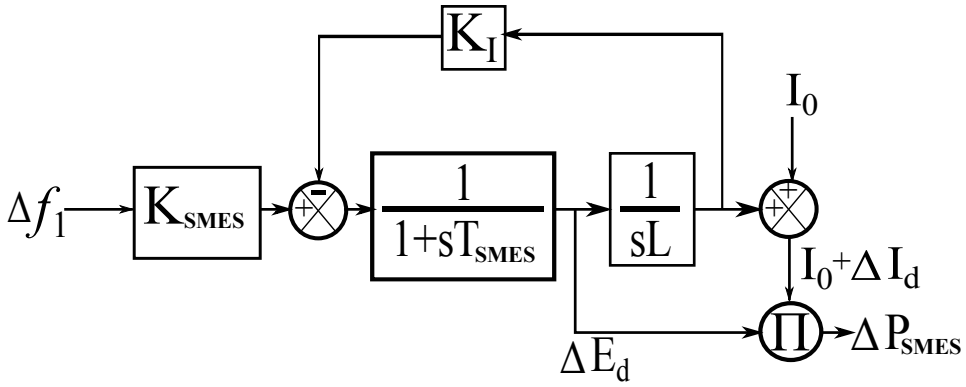

Figure 4.12: SMES Control Block Diagram

Table 4.2: Simulation Parameters for SMES

Simulation Parameters for SMES	
Parameter	Value
SMES inductive coil	3.3 H
DC link Capacitance	6750 μ F
Grid Voltage	290 V
Interface Resistance	2 m Ω
Interface Inductance	660 μ H

4.5 Static Synchronous Compensator

A voltage source converter has been interconnected at the mid point of the transmission line of SMIB system as shown in Fig. 4.17. To portray the sub transient and transient characteristics of the system, the previous assumption of synchronous machine model has been relaxed in this section. The synchronous generator has been modelled as a variable voltage source behind sub transient reactance. The phasor relation between the bus voltages and line current has been depicted in Fig. 4.18. The equations (4.21) to (4.25), have been further simplified as (4.26) and (4.27) . The VSC with the active power source can independently control the terminal voltage and current. Thus, a four quadrant control is possible. The grid voltage at PCC can be controlled by varying VSC ac terminal voltage and current. Due to four quadrant operation the grid voltage V_s trajectory is circular. Once, the grid voltage V_s has been controlled the terminal bus voltage V_t can have trajectory given as semi circle.

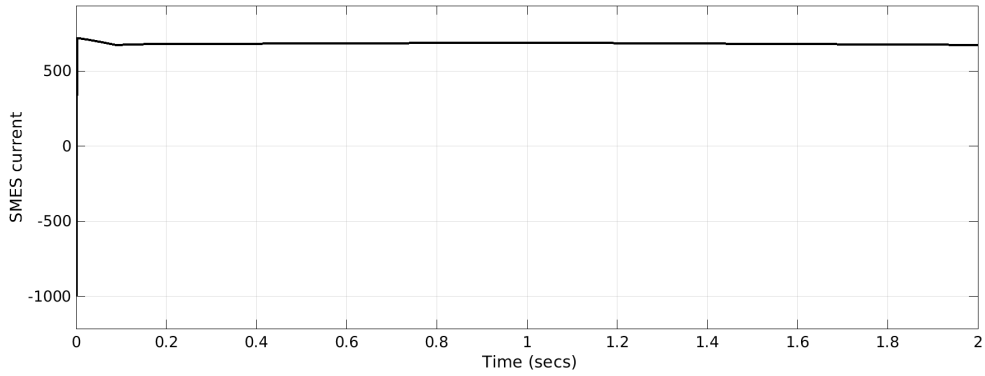

Figure 4.13: SMES current

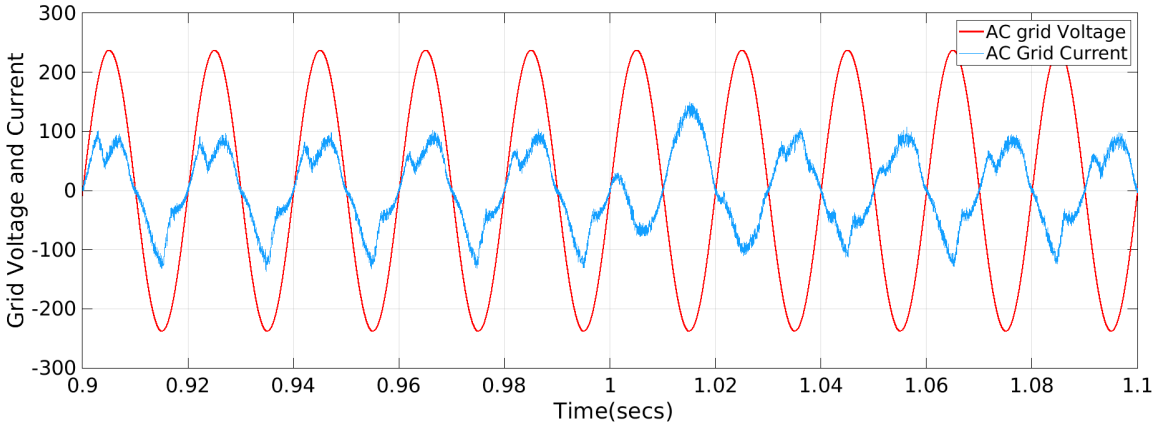

Figure 4.14: SMES bidirectional Power flow

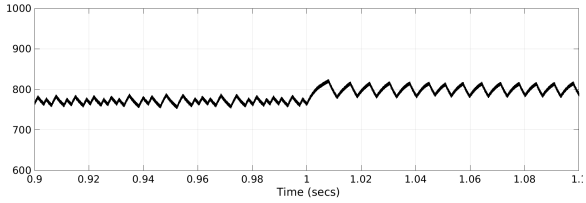

Figure 4.15: DC link voltage E_d

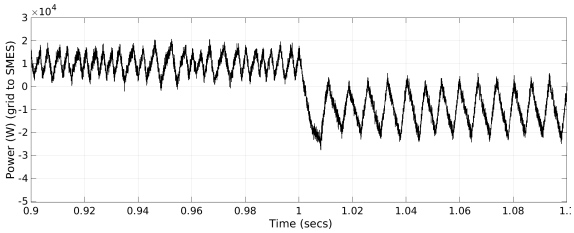

Figure 4.16: Active power flow

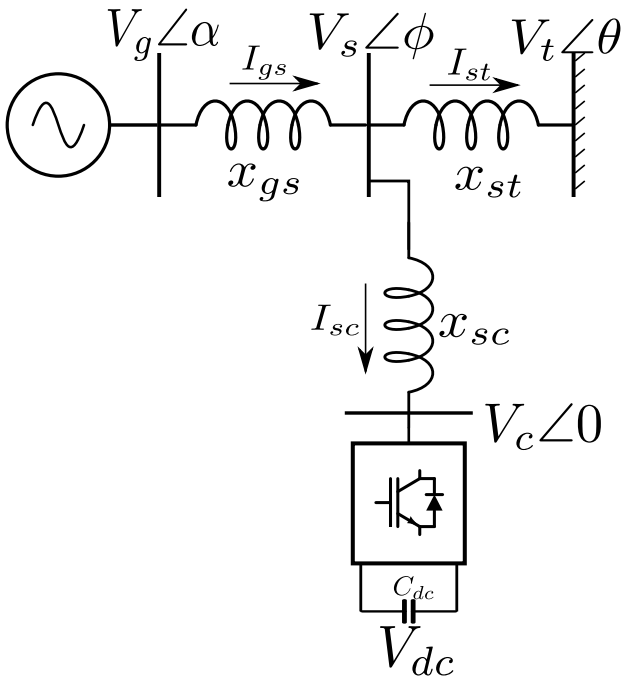

Figure 4.17: SMIB with VSC

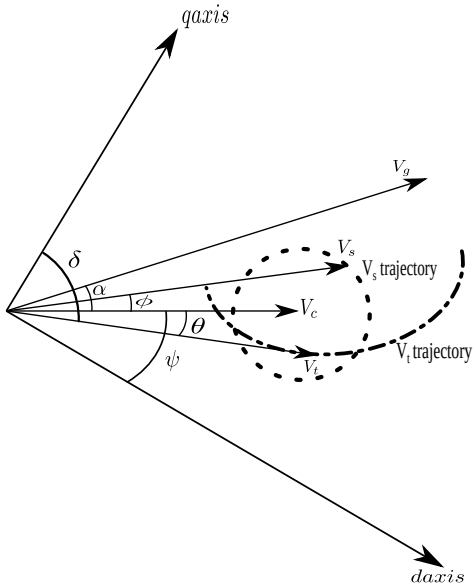

Figure 4.18: SMIB with VSC phasor diagram

$$\bar{V_g} = \bar{V_s} + jx_{gs}\bar{I_{gs}} \tag{4.21}$$
$$\bar{V_s} = \bar{V_t} + jx_{st}\bar{I_{st}} \tag{4.22}$$
$$\bar{V_s} = \bar{V_c} + jx_{sc}\bar{I_{sc}} \tag{4.23}$$
$$\bar{I_{gs}} = \bar{I_{sc}} + \bar{I_{st}} \tag{4.24}$$
$$\tag{4.25}$$

From (4.21) to (4.25), we can simplify the equations as below

$$\bar{V_g} = \bar{V_t} + jx_{gs}\bar{I_{gs}} + jx_{st}(\bar{I_{gs}} - \bar{I_{sc}}) \tag{4.26}$$
$$jx_{sc}\bar{I_{sc}} + \bar{V_c} - \bar{V_t} = jx_{st}(\bar{I_{gs}} - \bar{I_{sc}}) \tag{4.27}$$

The phasor quantities are transformed to the synchronously rotating $d-q$ axis, given as

$$v_{gd} + jv_{gq} = V_t e^{j\frac{\pi}{2}-\delta} + jx_{gs}(i_{gsd} + ji_{gsq}) + jx_{st}(i_{gsd} - i_{scd} + j(i_{gsq} - i_{scq})) \tag{4.28}$$
$$jx_{sc}(i_{scd} + ji_{scq}) + V_c e^{j\psi} - V_t e^{j\frac{\pi}{2}-\delta} = jx_{st}(i_{gsd} - i_{scd} + j(i_{gsq} - i_{scq})) \tag{4.29}$$

The generalised model of the synchronous machine is given as

$$\dot{\Psi}_d = v_{gd} + \omega\Psi_q \tag{4.30}$$
$$\dot{\Psi}_q = v_{gq} - \Omega\Psi_d \tag{4.31}$$
$$\dot{\Psi}_f = v_f - r_f i_f \tag{4.32}$$
$$\dot{\Psi_D} = -r_D i_D \tag{4.33}$$
$$\dot{\Psi_Q} = -r_Q i_Q \tag{4.34}$$

where

$$\begin{bmatrix} \Psi_d \\ \Psi_f \\ \Psi_D \\ \Psi_q \\ \Psi_Q \end{bmatrix} = \begin{bmatrix} x_d & x_{ad} & x_{ad} & 0 & 0 \\ x_{ad} & x_f & x_{ad} & 0 & 0 \\ x_{ad} & x_{ad} & x_D & 0 & 0 \\ 0 & 0 & 0 & x_q & x_{ad} \\ 0 & 0 & 0 & x_{ad} & x_Q \end{bmatrix} \begin{bmatrix} -i_{gsd} \\ i_f \\ i_D \\ -i_{gsq} \\ i_Q \end{bmatrix}$$

Comparing (4.30) and (4.31) to (4.28), we have

$$\dot{\Psi}_d = V_t sin\delta - i_{gsq}(x_{gs} + x_{st}) + i_{scq}x_{st} + \omega\Psi_q \tag{4.35}$$

$$\dot{\Psi}_q = V_t cos\delta + i_{gsd}(x_{gs} + x_{st}) - i_{scd}x_{st} - \omega\Psi_d \tag{4.36}$$

Also from (4.29),

$$V_c cos\psi - V_t sin\delta = i_{scq}(x_{sc} + x_{st}) - i_{gsq}x_{st} \tag{4.37}$$

$$V_c sin\psi - V_t cos\delta = -i_{scd}(x_{sc} + x_{st}) + i_{gsd}x_{st} \tag{4.38}$$

From (4.35) to (4.36), the generator flux linkages can be written in terms of the converter terminal voltages as

$$\dot{\Psi}_d = V_c cos\psi - i_{scq}x_{sc} - i_{gsq}x_{gs} + \omega\Psi_q \tag{4.39}$$

$$\dot{\Psi}_q = V_c sin\psi + i_{scd}x_{sc} + i_{gsd}x_{gs} - \omega\Psi_d \tag{4.40}$$

where the output voltage of the PWM VSC with modulation index m is given as

$$\bar{V_c} = m\frac{V_{DC}}{2}\angle\psi \tag{4.41}$$

Assuming no losses in the converter, the active power received at the DC capacitor is given as

$$V_{DC}I_{DC} = i_{scd}m\frac{V_{DC}}{2}cos\psi + i_{scq}m\frac{V_{DC}}{2}sin\psi \tag{4.42}$$

Thus, I_{DC}, is given as

$$I_{DC} = i_{scd}m\frac{1}{2}cos\psi + i_{scq}m\frac{1}{2}sin\psi \tag{4.43}$$

The DC side dynamic voltage is given as

$$C_{DC}\dot{V_{DC}} = i_{scd}m\frac{1}{2}cos\psi + i_{scq}m\frac{1}{2}sin\psi + i_{dc,2} \tag{4.44}$$

where $i_{dc,2}$ is the current from active source. If $i_{dc,2} = 0$, the VSC acts STATCOM. The relation between STATCOM control and frequency is thus given as

$$\begin{bmatrix}\dot{\delta}\\ \dot{\omega}\end{bmatrix} = \begin{bmatrix}\omega_o\Delta\omega\\ \frac{1}{M}(-K_s\Delta\delta - D\Delta\omega - K_{STAT}\Delta m)\end{bmatrix} \tag{4.45}$$

Table 4.3: Simulation Parameters for STATCOM

Simulation Parameters for STATCOM	
Parameter	Value
DC link Capacitance	6750 μ F
Transformer Capacity	900 kVA

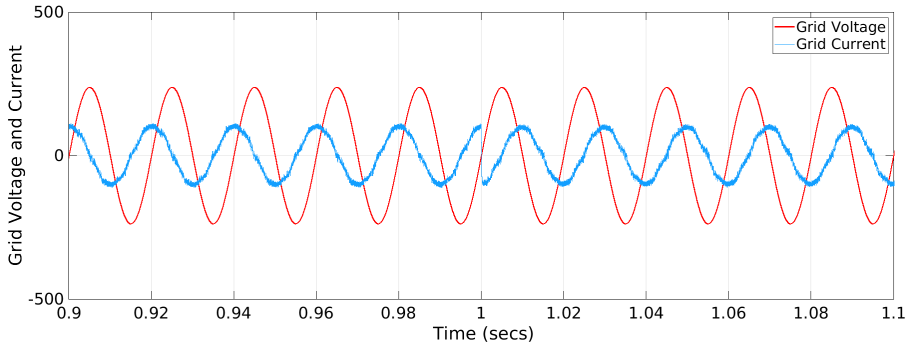

Figure 4.19: Grid Voltage and current with STATCOM

STATCOM can be controlled to operate as inductive load or capacitive load. While operating as an inductive load the current drawn by the STATCOM lags the phase voltage by 90^o, it leads the phase voltage with same phase when operating as a capacitive load, as shown in Fig. 4.19. The DC link voltage of the STATCOM is shown in Fig, 4.20 The parameters used for average switch modelling of STATCOM is presented in Table 4.3. The reference of STATCOM is changed from capacitive to inductive at time = 2 sec. Fig. 4.21, STATCOM was generating reactive power in capacitive mode and with change in reference, STATCOM consumes the reactive power.

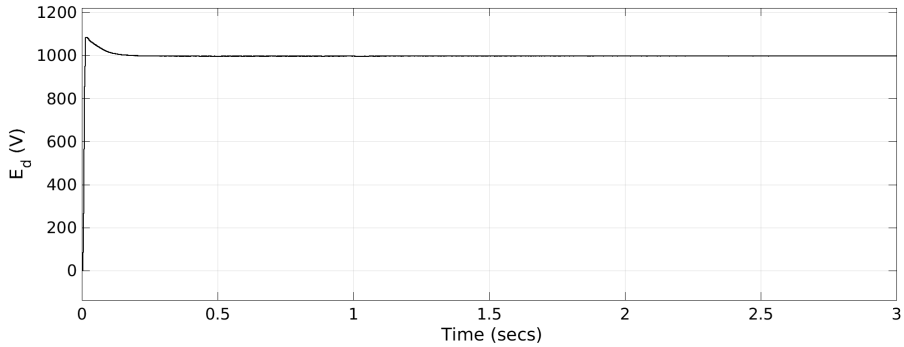

Figure 4.20: DC link voltage V_{dc}

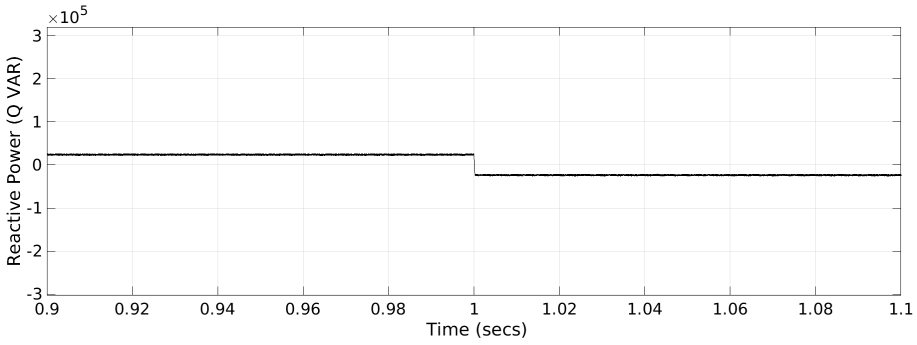

Figure 4.21: STATCOM Reactive Power flow

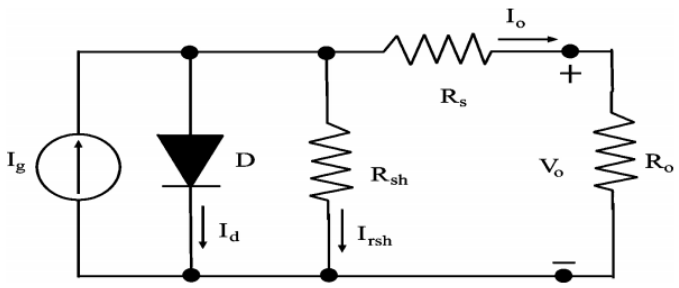

Figure 4.22: Solar PV model

4.6 Solar Photovoltaic

If a photon with sufficient energy (higher than band gap energy) strikes electron, it excites the electron to move towards p type region. And the current flows through P to N junction. This is analogous to a diode in forward bias, with an external current source (photocurrent). R_{sh} comes due to diode manufacturing factors as shown in Fig. 4.22. R_s occurs due to metal to semiconductor contact in Solar PV. [118].

From Fig. 4.22, the output current is given as

$$I_o = I_g - I_D \tag{4.46}$$

I_g depends on the solar irradiation S (KW/m^2) and temperature $T(C^o)$ as

$$I_g = \frac{[I_{sc} + I_t(T-25)]S}{1000} \tag{4.47}$$

And I_D is the diode uni directional current that flows from Anode to Cathode given

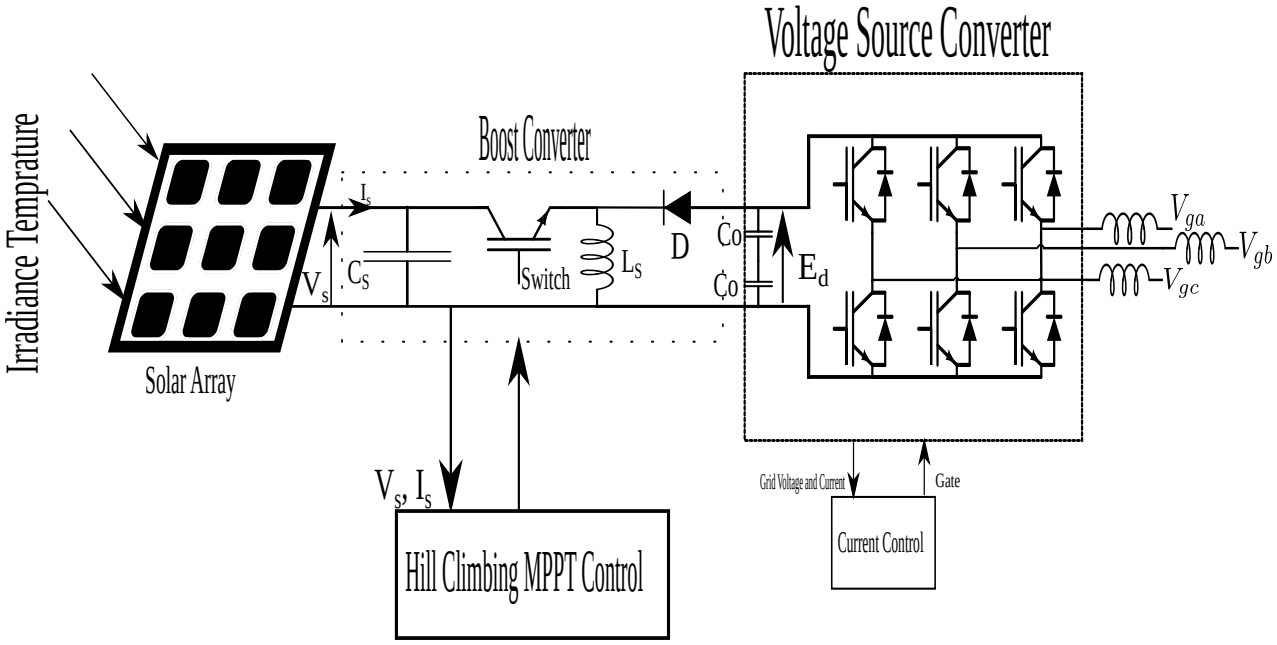

Figure 4.23: Grid connected Solar PV

as

$$I_D = I_{do}[e^{(\frac{V_o}{AKT})} - 1] \tag{4.48}$$

Thus output power is given as

$$P_o = V_o I_o$$

Linearizing the output power, about operating points we get

$$\Delta P_o = (I_{go} - I_{do})\Delta V_o + V_{o,0}(\Delta I_g - \Delta I_d) \tag{4.49}$$

Assuming, constant voltage and constant temperature at 25^oC, output power is a function of Solar irradiance given as

$$\Delta P_o = V_{o,0}\Delta I_g = V_{o,0}\frac{I_{sco}}{1000}\Delta S \tag{4.50}$$

This can be further modeled as [119]

$$\frac{\Delta P_o}{\Delta S} = \frac{G_s}{1 + sT_s} \tag{4.51}$$

[1] Grid connected Solar PV shown in Fig. 4.23, is controlled to deliver power to

[1]Rachakonda S.R. Akshay and Rajesh J. Abraham, "Load Frequency Regulation with Solar PV and

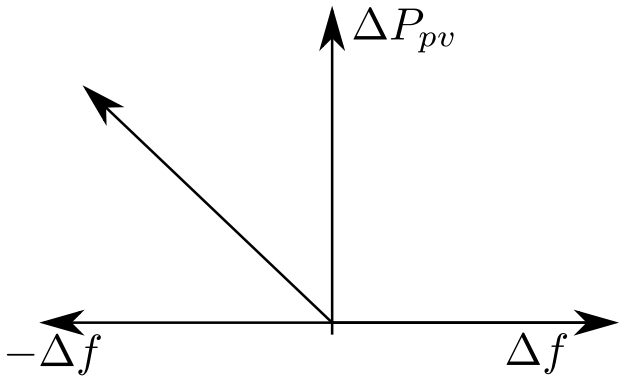

Figure 4.24: Grid connected Solar PV

Table 4.4: Simulation Parameters for Solar PV

Simulation Parameters for Solar PV	
Parameters	Value
Open Circuit voltage	36.3 V
Short Circuit Current	7.84 A
Maximum power point Voltage	29 V
Maximum Power Point Current	7.35 A
Panels connected in series	10
Strings connected in parallel	40
Maximum Power	80 kW

Table 4.5: Simulation Parameters for Solar PV Grid

Simulation Parameters for Solar PV Grid	
Parameters	Value
Voltage 25 kV	25 kV
Transformer Size	100 kVA
Transformer Primary	260 V
Transformer Secondary	25 kV

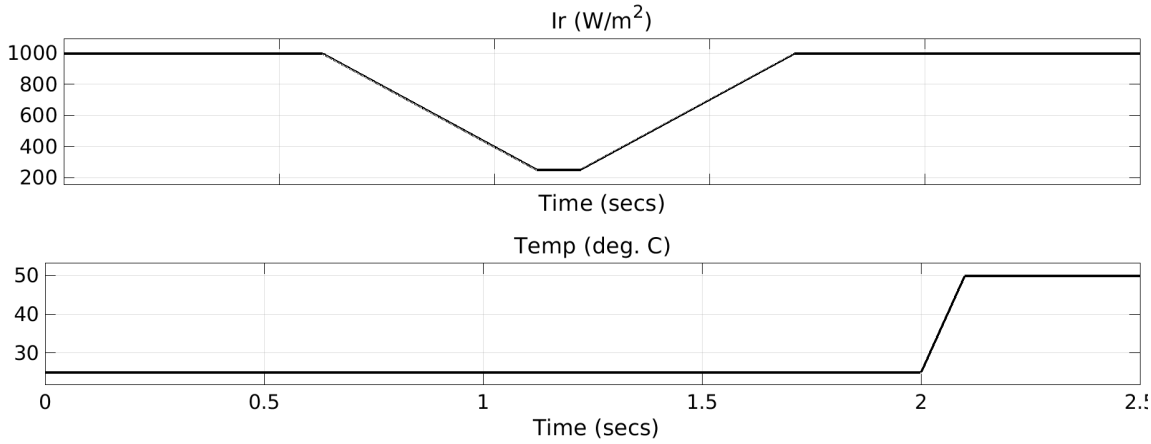

Figure 4.25: Temprature and irradiation

loads in conjunction with Grid Sources. Maximum Power Point Tracking control tracks maximum power to deliver under varying temperature and irradiance. It is important to note that the solar PV does not absorbs the active power from the grid. The solar PV injects power during frequency drop which is depicted in Fig. 4.24. The simulation parameters used for average switch modelling of solar PV is presented in Table 4.4 and Table 4.5. A frequency error based proportional controller is used that equalizes the power imbalance from Solar PV such that the system is further linearized as

$$\frac{\Delta P_o}{\Delta f} = \frac{K_{PV}}{1+sT_{PV}} \tag{4.52}$$

The power output of the solar PV varies with solar irradiance and the temperature. For the dynmaic model of solar PV the assumed solar irradiance and temperature is presented in Fig. 4.25.

The power output from the solar PV decreases with increase in temperature, and reduction in solar irradiance which can be seen from Fig.4.26. Solar PV power output is unidirectional, the phase current and the grid voltage is presented in Fig. 4.27.

4.7 Conclusion

The mathematical model of VSC to control STATCOM, SMES, BESS and Solar PV for LFC application has been discussed in detail in this chapter. The phase control

Battery Energy Storage System", International Journal of Power and Energy Systems, ACTA press, 39.1 (2019)

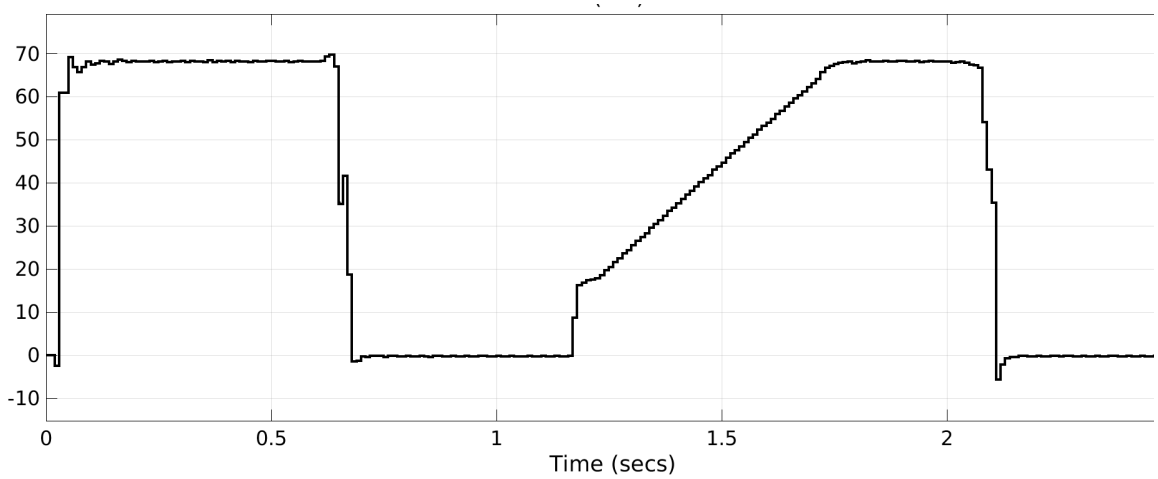

Figure 4.26: Solar Power flow

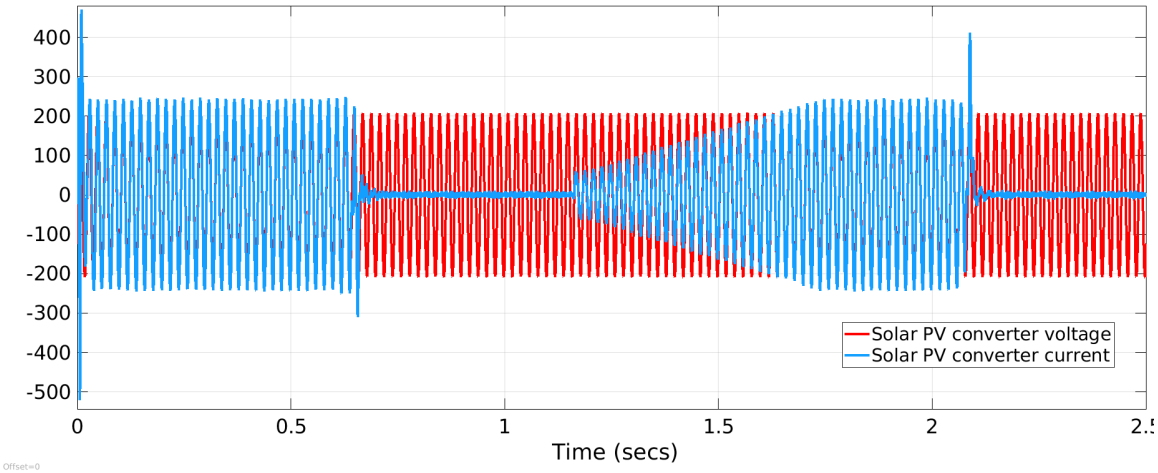

Figure 4.27: Solar PV VSC output voltage and current

method of VSC has been discussed in the first section. This method induces harmonics of the order of $6m \pm 1$ into the system, that are difficult to filter. The next section focuses on Sine PWM control of VSC, that has harmonics of the order of $mF \pm nf$ that are at the higher frequency end and easier to filter out.

In grid tied converter, a vector decoupled controller, can independently control the active and reactive power injected into the grid. The dynamic control techniques for active power in BESS and SMES are outlined in this section, while the dynamic response of reactive power in STATCOM is also presented. The average switching model solar PV that varies dynamically with temperature and solar irradiance is presented in section 4.6.

Chapter 5

Optimal Sizing and Placement of Energy Storage and FACTS Devices

In this section we attempt to present optimal placement and size of Static Compensator (STATCOM), Battery Energy Storage (BESS), Solar Photovoltaic (Solar PV). A simplified technique to locate best voltage bus to place shunt reactive power compensation, solar PV and Battery Energy storage is explained. The contingency analysis reveal critical transmission lines connected between weak voltage buses. The weak buses are potential sites for connecting shunt FACTS devices such as STATCOM to improve voltage stability of a bus by reactive power compensation. A weak bus is characterized as a load bus prone to voltage instability [120]. The weak bus in the power system is an ideal location to place a shunt FACTS device.

However, in a large system with more than one weak bus, optimal location is chosen such that the

- Objectives of Optimal location
  - Minimize active power loss
  - Minimum bus voltage deviation
  - Minimum injected reactive power compensation.
- Objectives of Optimal sizing
  - Maintain Power flow limit.
  - Maintain bus voltage limit.
  - Minimum investment cost.

A case study of IEEE 9-Bus is presented in this section and small signal model is simulated using Pandapower.

The problem of optimal placement of compensating devices is formulated as a multi-objective problem which meets the above criteria.

5.1 Optimal Sizing and Placement in IEEE 9-Bus System

Contingency analysis preview the security of the power system by simulating the contingency events in advance and categorizing the state of power system as safe, severe and critical [121], [122].
To execute contingency analysis, Load flow analysis is carried out after until each line has been taken out of service once [123],[124]. The buses violating the voltage limits are identified as weak voltage buses and the lines violating Power limits are identified as weak lines. The load flow data for the analysis has been presented in [125].

The size of compensating device is calculated to maintain system within power and voltage limits. Compensating device is placed at weak buses and load flow analysis is carried out again. Active power loss and bus voltage deviation is calculated. The case with minimum active power loss and voltage deviation gives optimal location and size for compensating device. Fig. 5.1 shows IEEE 9-Bus system, where bus 1 is the slack bus. While, bus 2 and bus 3 are the generator buses. bus 5, bus 7 and bus 9 are the load buses. buses violating the voltage limits given in (5.1) are identified as weak buses.

$$V_{min} \leq V_{bus} \leq V_{max} \tag{5.1}$$

At each weak bus, compensating devices are placed and the optimal bus location is searched by evaluating power losses and size of reactive power compensation required. The reactive power source with no active power generation has been placed at each weak bus using (5.2) and (5.3), it is found that bus 2 is the optimal location to place STATCOM and bus 8 is the optimal for Solar PV and BESS that minimizes active power losses. It may be inferred that the power loss in the IEEE 9-Bus system is reduced with solar PV-BESS combination to 5.12 MW, whereas without solar PV-BESS-STATCOM combination is 10.68 MW. Hence, 5.56 MW has been supplied by solar PV and BESS. The reactive power demand at bus 2 has reduced from 78.94

Table 5.1: Load Flow without Solar PV STATCOM BESS

bus	V (pu)	δ	P (MW)	Q (MVAR)
1	1.000000	0.000000	-77.680773	-2.438062
2	1.000000	-2.088319	-163.000000	-78.947813
3	1.000000	-2.556817	-85.000000	-11.050500
4	0.999598	-2.565539	0.000000	0.000000
5	0.982600	-6.670000	90.000000	30.000000
6	0.994772	-5.426918	0.000000	0.000000
7	0.957660	-9.550092	100.000000	35.000000
8	0.956101	-8.204944	0.000000	0.000000
9	0.794007	-22.569376	125.000000	50.000000

Table 5.2: Load Flow with Solar PV STATCOM BESS

bus	V (pu)	δ	P (MW)	Q (MVAR)
1	1.000000	0.000000	-68.120491	-22.957721
2	1.000000	10.086551	-163.000000	-8.324468
3	1.000000	5.103786	-85.000000	5.251542
4	0.987556	-2.277065	0.000000	0.000000
5	0.976089	-3.810932	90.000000	30.000000
6	1.004313	2.260974	0.000000	0.000000
7	0.988327	1.031750	100.000000	35.000000
8	1.000000	4.239400	-4.000000	-8.697111
9	0.959144	-4.093385	125.000000	50.000000

MVAR to 8.32 MVAR. The difference, 70.62 MVAR in the bus 2 has been compensated by the STATCOM. Thus, the minimum size of solar PV and BESS is 5.56 MW and the STATCOM is 70.62 MVAR. The load flow results before and after the compensation are presented in Tables 5.1 and 5.2 respectively.

$$P_{loss} = \sum P_{gen} - \sum P_{demand} \tag{5.2}$$

$$Q_{size} = max(\sum Q_{gen} + \sum (Q_{demand})) \tag{5.3}$$

For the assumed case it is found that

- bus 2 is found suitable for reactive power compensation for voltage support.

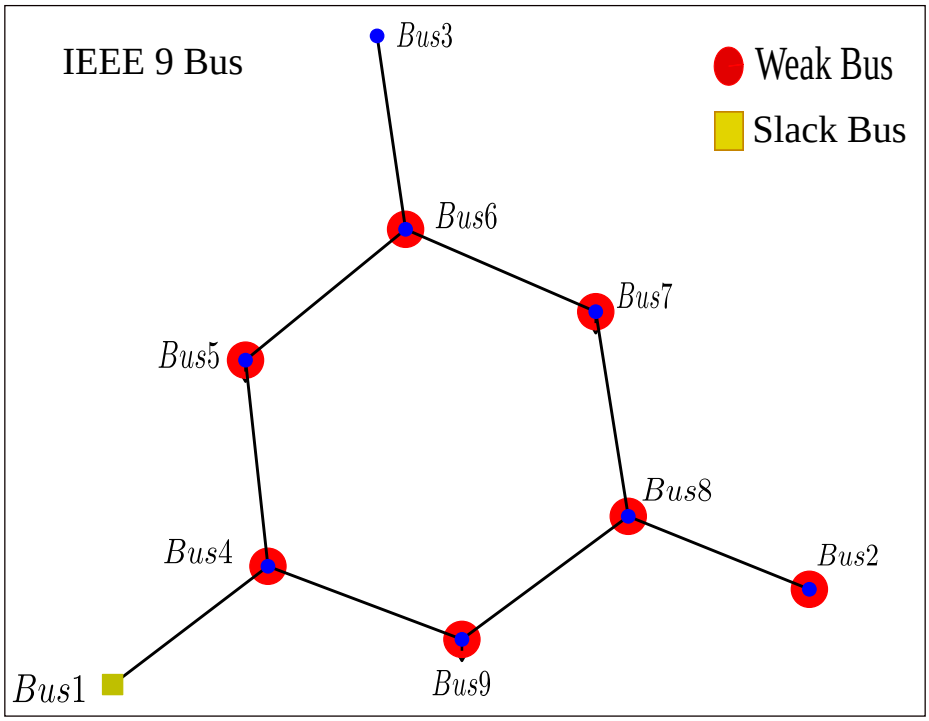

Figure 5.1: Nine bus System weak buses

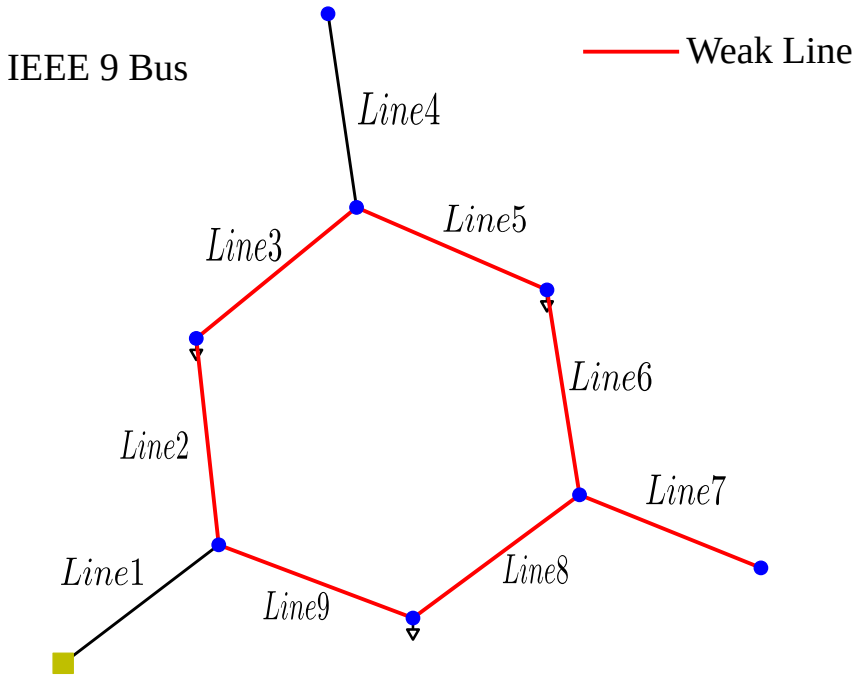

Figure 5.2: Nine bus system weak lines

- Active power compensation at bus 8 minimizes power losses.

5.2 Optimal Location and Sizing of Solar PV-BESS and STATCOM in IEEE 57-Bus System with Genetic Algorithm

The IEEE 57-bus system stands as a simplified yet representative model of an American Electric Power System (AEP) from the early 1960s. Designed as a benchmark for power system analysis, it comprises 57 buses, 7 generators, and 42 loads as shown in Fig. 5.3. The IEEE 57-Bus system finds widespread application in various power system studies such as:

- Power Flow Analysis: Investigating the flow of active and reactive power throughout the system to determine voltage magnitudes, angles, power losses, and line flows.

- Contingency Analysis: Evaluating the system's resilience against potential failures, such as line outages or generator trips, and its ability to recover from such disruptions.

- Optimization Studies: Identifying optimal operating conditions for the system to minimize costs, enhance efficiency, or improve reliability.

The IEEE 57-Bus system proves invaluable for power system engineers and researchers, enabling them to develop, test, and refine power system analysis tools and algorithms.

5.2.1 Sizing and Location of Solar PV and BESS

The N-1 contingency analysis (single line outage) is performed to identify the lines that are overloading (>100 %) in IEEE 57-Bus system. The buses of the overloading lines are potential candidates for solar PV and BESS grid integration. The active power source is connected to the candidate buses and Genetic algorithm (GA) is utilized to determine the optimal size of active power source for the selected buses, aiming to minimize active power loss [126]. The objective function for minimizing

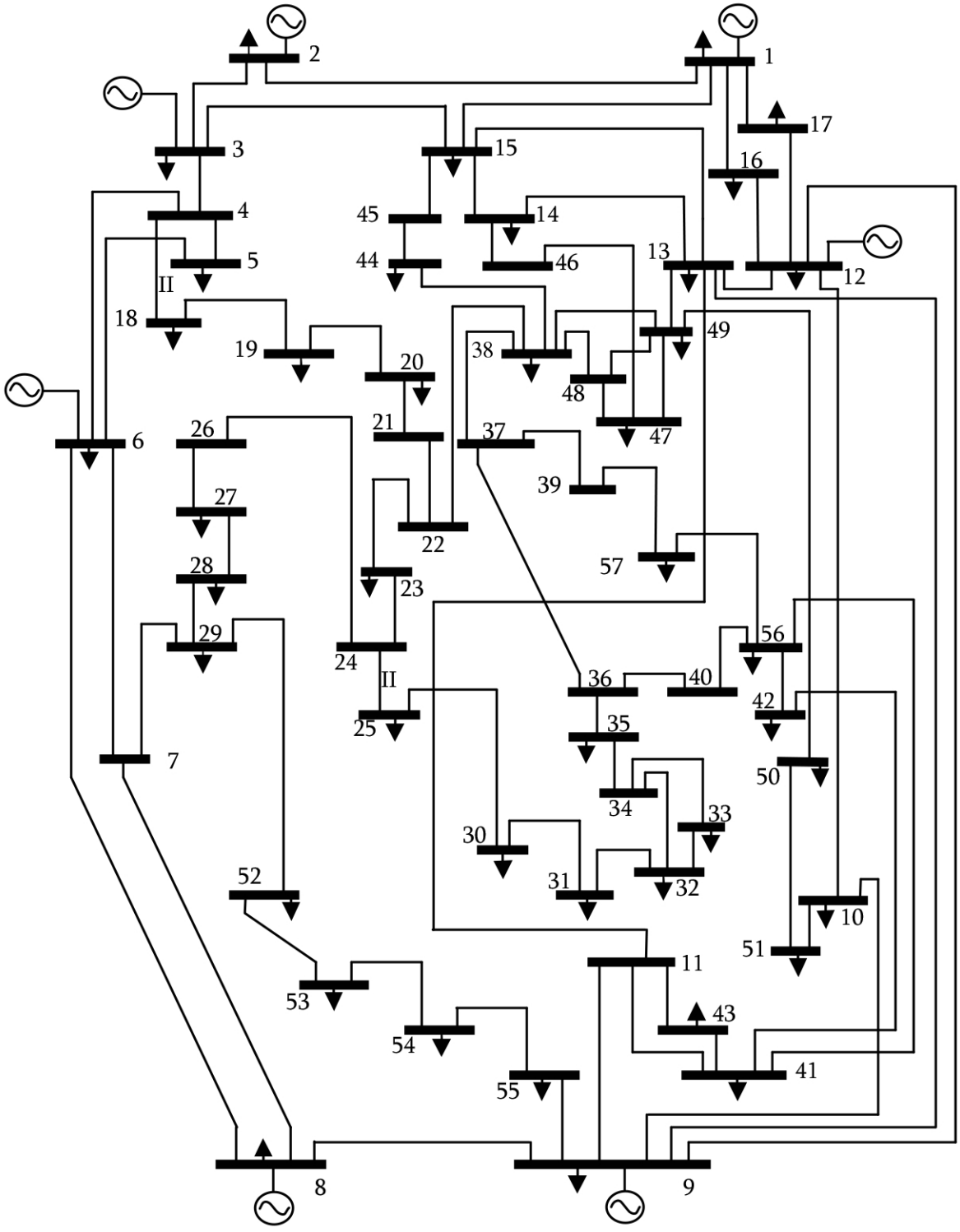

Figure 5.3: IEEE 57-Bus system [8]

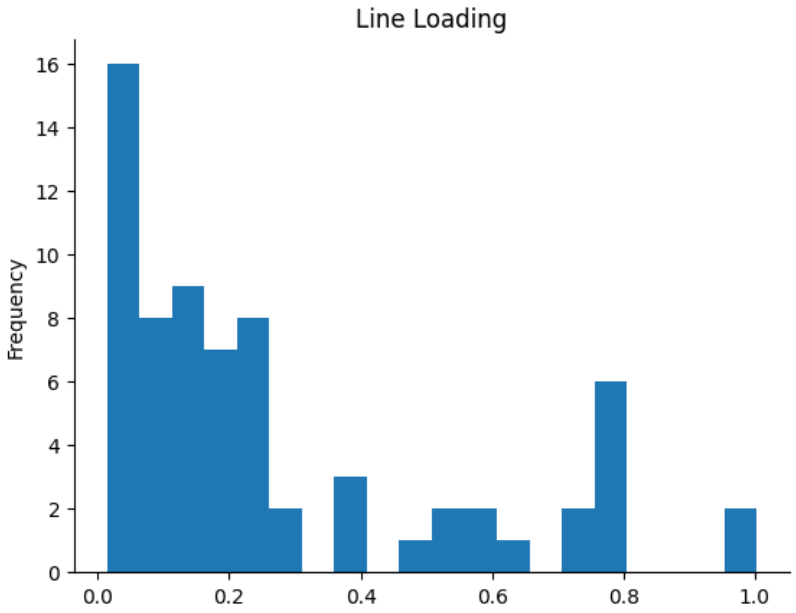

Figure 5.4: Line loading of base network

the active power loss is given as

$$J_{solarPV,BESS} = P_{loss} \tag{5.4}$$

The base IEEE 57-Bus system without STATCOM, solar PV and BESS in Fig. 5.4. The histogram plot in Fig. 5.4 shows the number of lines in y axis vs. the line loadings as a fraction of line's own capacity in x axis. It can be seen that two lines are loaded to their maximum capacity in this case.

The optimal location and size for the solar PV and BESS to minimize the active power losses is found to be Bus 7 and 130 MW. The plot of objective function ($J_{solarPV,BESS}$) to the number of iterations is shown in Fig. 5.5. The minimum losses and the peak line loading reduced due to the inclusion of active power source to 0.85 as presented in Fig. 5.6.

5.2.2 Sizing and Location of STATCOM

To identify the weak voltage buses, N-1 contingency is carried out. The buses with voltage magnitudes below 0.95 p.u. are considered weak voltage buses [127]. The weak voltage buses are prioritized location for STATCOM integration.

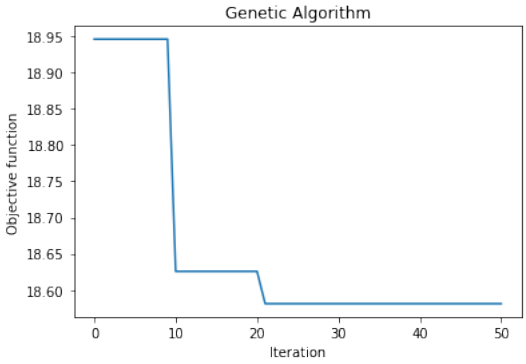

Figure 5.5: Objective functions (active power loss) vs No. of iterations of GA

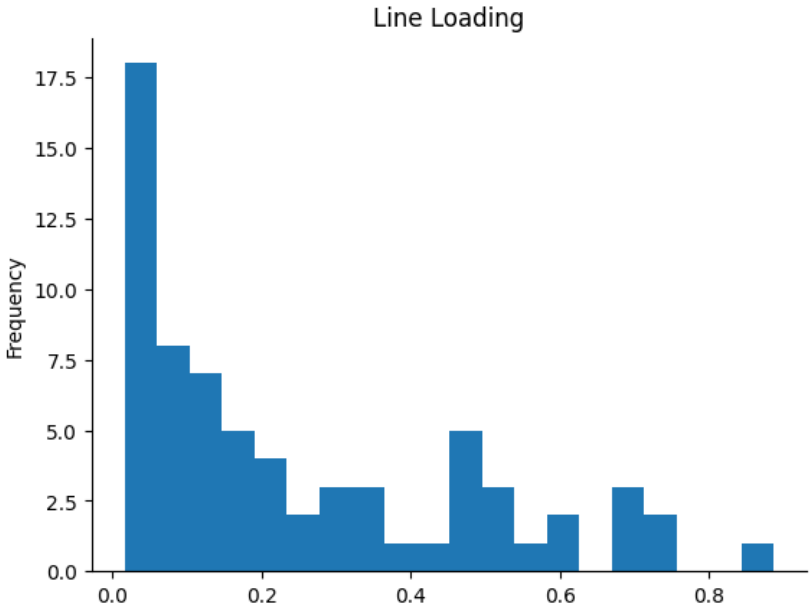

Figure 5.6: Line Loading of IEEE 57-Bus system with Solar PV and BESS

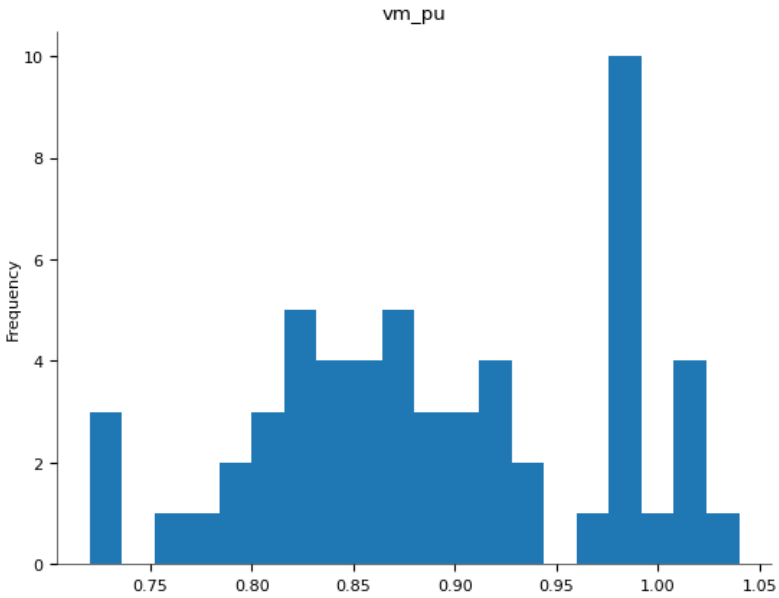

Figure 5.7: Bus Voltages for base IEEE 57-Bus network

The objective function to minimize using GA is given as below

$$J_{STATCOM} = |(1 - \mu_{V_{Bus}} + 0.5\sigma_{V_{Bus}})| \tag{5.5}$$

where $\mu_{V_{Bus}}$, is the mean of bus voltages and $\sigma_{V_{Bus}}$ is the standard deviation of bus voltages. The fitness of each configuration is estimated by the objective function value (voltage deviation).

The base network bus voltages is presented in Fig. 5.7. The minimum bus voltage is improved with 50 MVAR STATCOM at Bus 33, and shown in Fig. 5.8. The convergence of objective function to the number of iterations using GA is given in Fig. 5.9.

5.3 Conclusion

This chapter attempts to select optimal location for placement of energy systems such as solar PV, BESS and STATCOM, while focusing on the impact of energy systems on the IEEE bus system. In section 5.1, IEEE 9-Bus system, small system is considered. In this case it is expected to observe the impact of energy storages more significantly as compared to their impact on a larger system. Contingency Analysis conducted show that Bus 2 is optimal location to place STATCOM and Bus 8 is optimal for solar

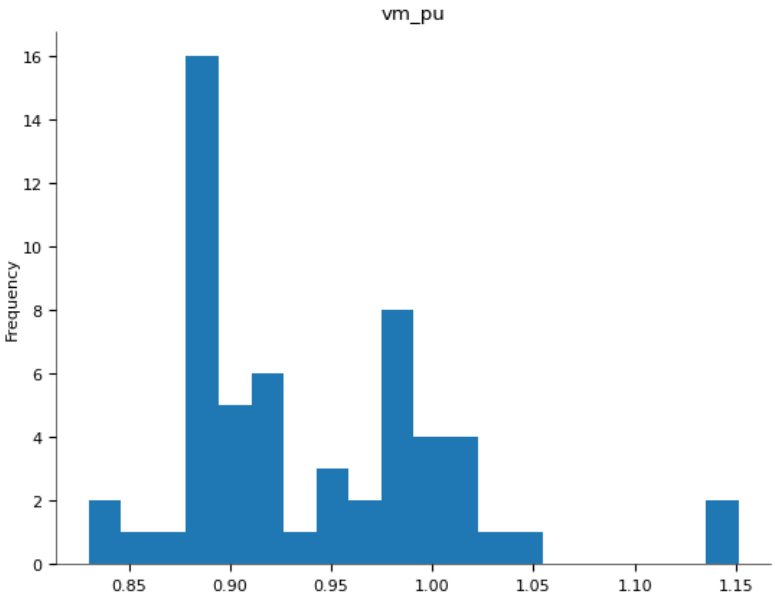

Figure 5.8: Bus Voltages for IEEE 57-Bus network with solar PV, BESS and STATCOM

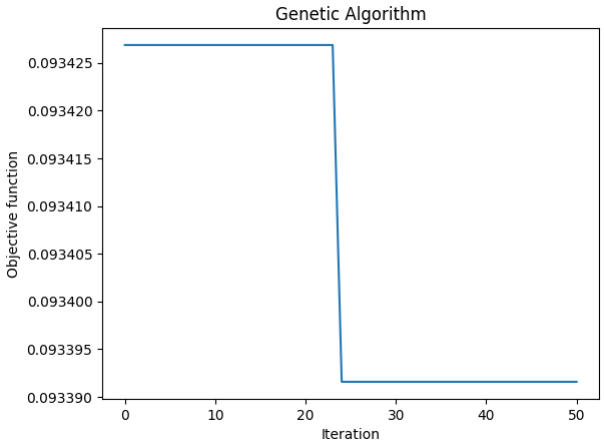

Figure 5.9: Objective functions (voltage deviation) vs No. of iterations of GA

PV-BESS in an IEEE 9-Bus system.

The sizing and optimal location study for energy storages and STATCOM is carried out in section 5.2 for IEEE 57-Bus system using GA. The size of active power source (solar PV and BESS) is found to be 130 MW to minimize active power losses to 18 MW. The STATCOM of size 50 MVAR is found to be suitable at Bus 33 for minimum voltage deviation.

Chapter 6

Conclusion and Future Work

Load Frequency Control is used to maintain frequency within the desired range by balancing load and generation in real time. In literature, three levels of control are generally used to achieve frequency controlled ancillary services, primary frequency control (5 sec to 10 sec), secondary response (10 sec to 10 mins) and tertiary frequency control requires response period of 10 mins to 30 mins. This thesis presents some improved results on LFC study of conventional and restructured power systems emphasizing on integration of FACTS devices, energy storages and Solar PV. LFC models with reheat thermal power generation have been proposed. The results are summarized in following sections.

6.1 Mathematical modeling and LFC of power systems

Mathematical modeling of the two area power system, interconnected power system with STATCOM, SMES, BESS and Solar PV are presented for LFC study. The participation of the STATCOM, SMES, BESS and Solar PV for frequency regulation in a control area is modelled as linear time invariant first order model. The mechanical input of the generating unit is governed by the Area Control Error. Genetic Algorithm has been implemented to find optimal controller gains to minimize area control error. This work also present technical concerns inherent in LFC in interconnected power systems, which have arisen because of the ongoing deregulation being experienced by electric industries around the world. Deregulation has led to the emergence of private entities such as generation companies (GENCOs) which sell energy and distributed companies (DISCOs) purchase electricity from GENCOs

competitively. An independent system operator (ISO) is responsible for providing LFC in each control area and maintain scheduled tie line power contracted from the competitive power market. Furthermore, transmission companies (TRANSCOs) in large interconnections allowed access to the transmission networks. Consequently, the number of inter area power contracts between GENCOs and DISCOs have increased.

6.2 LFC of conventional power systems

LFC of conventional two area interconnected power systems has been studied using GA based control. The non-reheat and reheat turbines are taken to demonstrate the application of STATCOM-SMES combination and Solar PV - BESS combination for LFC of interconnected power systems. The dynamic responses are obtained for two area interconnected power systems considering thermal non-reheat turbine and thermal reheat turbine generating units. The integral control is presented that uses less number of states, as feedback to calculate ACE and thereby reducing the controller cost and complexities. LFC scheme is presented for power systems with multi source power generation. The effect of GRC on dynamic response is discussed. The critical examination of dynamic responses reveals that GRC results in increased peak overshoot, however settling time remains same for this particular power system model. The controller gives satisfactory dynamic responses for turbines considering GRC. It shows that GA is able to accommodate the effect of GRC also. Investigations reveal that it is better to prefer the medium value of R i.e. 2.4 MW/Hz with corresponding optimum controller gains to provide better dynamic response of LFC for the proposed system. The dynamic responses are obtained for 10% step load perturbation. The simulation results show that proposed control strategy is very effective and guarantees good performance. In fact, this method provides a control system that satisfies the load frequency control requirements with a credible dynamic response. Similar results were obtained when the analysis was extended to multi unit multi area thermal system. A combination of Solar PV and BESS has been analysed to improve the frequency of an interconnected power system following a sudden load demand. A linear incremental model of PV and BESS has been shown to improve the performance of AGC of two area interconnected power system. The power generated from Solar PV is stochastic, BESS is used to level the output power of Solar PV. Simulation studies carried out in MATLAB validate that the proposed combination can

effectively improve the system frequency in the wake of sudden load disturbances.

6.3 LFC of power systems considering STATCOM

The role of ancillary services is to provide support for the transmission of power while maintaining reliable operation, power quality and grid safety. As per Indian electricity grid code, ancillary services are services necessary to support power system or grid operation in maintaining power quality, reliability and security of the grid. Ancillary services may include scheduling and dispatch, frequency regulation, voltage control, generation reserves etc. An attempt is made to study the the dynamic performance of LFC of the power systems considering STATCOM at tie lines. A simple but practical controller is used to improve the dynamic response of LFC system in the the new power system environment. The integral controller performs well for the power system with STATCOM and energy storage, giving better dynamic responses having relatively smaller peak overshoot and lesser settling time with zero steady state error as compared to the power system considering AC tie line only. The dynamic response of the system with STATCOM is improved significantly with the percentage reduction in the peak overshoot of Δf_1 , Δf_2 and ΔP_{tie12}. Dynamic responses are obtained for step load perturbation of 10% which satisfy the LFC requirements. The simulation results show that proposed control strategy considering STATCOM at tie line is very effective and guarantees good performance. Further, the GA based integral controller is proposed to control generating units and STATCOM which in turn controls the tie line power flow. The proposed controller for the power system with STATCOM gives better dynamic responses having relatively smaller peak overshoot and lesser settling time with zero steady state error as compared to the power system without STATCOM. The dynamic response of the system with STATCOM is improved significantly with the percentage reduction in the peak overshoot of Δf_1 , Δf_2 and ΔP_{tie12} and the settling time. Dynamic responses are obtained for load disturbance 0.1 pu MW. Simulation results show that the due to the presence of STATCOM, the dynamic performance in terms of settling time and peak overshoot is greatly improved. The system with STATCOM is capable of damping tie line power deviations more effectively under load perturbations. The simulation results show that proposed control strategy considering STATCOM is very effective and guarantees good performance.

6.4 LFC in restructured power system environment

A new model of two area interconnected power system with STATCOM-SMES in restructured power system environment is proposed. Modified LFC scheme is presented in restructured power system environment. A state space model of the proposed power system in restructured power system environment is utilized for controller design considering all the interface variables like control area frequencies, tie line power and all other possible contracts between GENCOs and DISCOs. An extensive analysis is done for LFC scheme considering bilateral contract, unilateral contract and contract violation. It is found that in all the cases, the area frequency error becomes zero in the steady state which satisfy the LFC requirements. It is found that actual values of generations and tie-line power exchanges of GENCOs obtained by MATLAB Simulink model of the power system are matching with the corresponding calculated values. Thus, the proposed LFC scheme is suitable in restructured power system environment.

6.5 Suggestions for further work

- The price based LFC mechanism for deregulated power system can be modelled using reinforcement learning.
- LFC study may be extended for various energy sources such as combined cycle gas turbine and pumped storage hydro power plants.
- Artificial Intelligence and Machine Learning based forecasting can be implemented to improve LFC.
- In the hierarchical structure, a centralized controller performs LFC by operating the local area controllers. The centralized controller does not directly control any generation resource to perform LFC functions in its area with respect to adjoining control areas, but computes the ACE of all control areas to generate a corrective signal that is given as a input signal to ISO. It would be an interesting future work to investigate LFC, where reference to local controller within a control area is given by a centralized controller considering competition in market, load forecasting and machine learning methods.

Bibliography

[1] N. Hatziargyriou, J. Milanovic, C. Rahmann, V. Ajjarapu, C. Canizares, I. Erlich, D. Hill, I. Hiskens, I. Kamwa, B. Pal, P. Pourbeik, J. Sanchez-Gasca, A. Stankovic, T. Van Cutsem, V. Vittal, and C. Vournas, "Definition and classification of power system stability – revisited amp; extended," *IEEE Transactions on Power Systems*, vol. 36, no. 4, pp. 3271–3281, 2021.

[2] A. J. Wood, B. F. Wollenberg, and G. B. Sheblé, *Power generation, operation, and control*. John Wiley & Sons, 2013.

[3] M. Beza and M. Bongiorno, "An adaptive power oscillation damping controller by statcom with energy storage," *IEEE Transactions on Power Systems*, vol. 30, no. 1, pp. 484–493, 2014.

[4] A. Yazdani and R. Iravani, *Voltage-sourced converters in power systems: modeling, control, and applications*. John Wiley & Sons, 2010.

[5] S. Tripathy and K. Juengst, "Sampled data automatic generation control with superconducting magnetic energy storage in power systems," *IEEE Transactions on Energy Conversion*, vol. 12, no. 2, pp. 187–192, 1997.

[6] K. Padiyar, *FACTS controllers in power transmission and distribution*. New Age International, 2007.

[7] J. S. Prasad, T. Bhavsar, R. Ghosh, and G. Narayanan, "Vector control of three-phase ac/dc front-end converter," *Sadhana*, vol. 33, no. 5, pp. 591–613, 2008.

[8] A. R. Al-Roomi, "Power Flow Test Systems Repository," Halifax, Nova Scotia, Canada, 2015. [Online]. Available: https://al-roomi.org/power-flow

[9] R. J. Abraham, D. Das, and A. Patra, "Automatic generation control of an interconnected hydrothermal power system considering superconducting magnetic

energy storage," *International Journal of Electrical Power & Energy Systems*, vol. 29, no. 8, pp. 571–579, 2007.

[10] Iea, "Energy efficiency – world energy outlook 2019 – analysis." [Online]. Available: https://www.iea.org/reports/world-energy-outlook-2019/energy-efficiency

[11] P. Kundur, J. Paserba, V. Ajjarapu, G. Andersson, A. Bose, C. Canizares, N. Hatziargyriou, D. Hill, A. Stankovic, C. Taylor *et al.*, "Definition and classification of power system stability IEEE/CIGRE joint task force on stability terms and definitions," *IEEE Transactions on Power Systems*, vol. 19, no. 3, pp. 1387–1401, 2004.

[12] H. Bevrani, "Decentralized robust load-frequency control synthesis in restructured power systems," 2004.

[13] N. Jaleeli, L. S. VanSlyck, D. N. Ewart, L. H. Fink, and A. G. Hoffmann, "Understanding automatic generation control," *IEEE transactions on power systems*, vol. 7, no. 3, pp. 1106–1122, 1992.

[14] H. Bevrani, "Robust power system frequency control," 2014.

[15] I. E. G. Code, "Indian electricity grid code - cercind.gov.in." [Online]. Available: https://cercind.gov.in/2010/ORDER/February2010/IEGC_Review_Proposal.pdf

[16] "Indian electricity grid code," New Delhi, Tech. Rep., 2010.

[17] P. Kundur, "Power system stability," *Power system stability and control*, pp. 7–1, 2007.

[18] B. J. Kirby, J. Dyer, C. Martinez, R. A. Shoureshi, R. Guttromson, J. Dagle *et al.*, *Frequency control concerns in the North American electric power system*. United States. Department of Energy, 2003.

[19] G. Vassell, "Northeast blackout of 1965," *IEEE Power Engineering Review*, vol. 11, no. 1, pp. 4–, 1991.

[20] R. Yan, N.-A. Masood, T. Kumar Saha, F. Bai, and H. Gu, "The anatomy of the 2016 south australia blackout: A catastrophic event in a high renewable network," *IEEE Transactions on Power Systems*, vol. 33, no. 5, pp. 5374–5388, 2018.

[21] G. Andersson, P. Donalek, R. Farmer, N. Hatziargyriou, I. Kamwa, P. Kundur, N. Martins, J. Paserba, P. Pourbeik, J. Sanchez-Gasca, R. Schulz, A. Stankovic, C. Taylor, and V. Vittal, "Causes of the 2003 major grid blackouts in north america and europe, and recommended means to improve system dynamic performance," *IEEE Transactions on Power Systems*, vol. 20, no. 4, pp. 1922–1928, 2005.

[22] V. Rampurkar, P. Pentayya, H. A. Mangalvedekar, and F. Kazi, "Cascading failure analysis for indian power grid," *IEEE Transactions on Smart Grid*, vol. 7, no. 4, pp. 1951–1960, 2016.

[23] J. W. Bialek, "Blackouts in the us/canada and continental europe in 2003: Is liberalisation to blame?" in *2005 IEEE Russia Power Tech*, 2005, pp. 1–7.

[24] Y.-K. Wu, S. M. Chang, and Y.-L. Hu, "Literature review of power system blackouts," *Energy Procedia*, vol. 141, pp. 428–431, 2017.

[25] A. Pappachen and A. P. Fathima, "Critical research areas on load frequency control issues in a deregulated power system: A state-of-the-art-of-review," *Renewable and Sustainable Energy Reviews, vol. no. 72*, pp. 163–177, 2017.

[26] P. Tielens and D. Van Hertem, "The relevance of inertia in power systems," *Renewable and Sustainable Energy Reviews*, vol. 55, pp. 999–1009, 2016.

[27] O. I. Elgerd and C. E. Fosha, "Optimum megawatt-frequency control of multiarea electric energy systems," *IEEE Transactions on Power Apparatus and Systems*, vol. PAS-89, no. 4, pp. 556–563, 1970.

[28] Ibraheem, P. Kumar, and D. Kothari, "Recent philosophies of automatic generation control strategies in power systems," *IEEE Transactions on Power Systems*, vol. 20, no. 1, pp. 346–357, 2005.

[29] J. Machowski, Z. Lubosny, J. W. Bialek, and J. R. Bumby, *Power system dynamics: stability and control*. John Wiley & Sons, 2020.

[30] V. Donde, M. Pai, and I. A. Hiskens, "Simulation and optimization in an AGC system after deregulation," *IEEE Transactions on Power Systems, vol. no. 16*, no. 3, pp. 481–489, 2001.

[31] L. Xiong, X. Liu, H. Liu, and Y. Liu, "Performance comparison of typical frequency response strategies for power systems with high penetration of renewable energy sources," *IEEE Journal on Emerging and Selected Topics in Circuits and Systems*, vol. 12, no. 1, pp. 41–47, 2022.

[32] S. Xu and W. Chen, "The reform of electricity power sector in the pr of china," *Energy policy*, vol. 34, no. 16, pp. 2455–2465, 2006.

[33] A. Tayyebi, D. Groß, A. Anta, F. Kupzog, and F. Dörfler, "Frequency stability of synchronous machines and grid-forming power converters," *IEEE Journal of Emerging and Selected Topics in Power Electronics*, vol. 8, no. 2, pp. 1004–1018, 2020.

[34] "Revealing drivers and risks for power grid frequency stability with explainable ai," *Patterns*, vol. 2, no. 11, p. 100365, 2021.

[35] F. Blaabjerg, M. Liserre, and K. Ma, "Power electronics converters for wind turbine systems," *IEEE Transactions on industry applications*, vol. 48, no. 2, pp. 708–719, 2011.

[36] M. H. Ali, B. Wu, and R. A. Dougal, "An overview of SMES applications in power and energy systems," *IEEE Transactions on Sustainable Energy*, vol. 1, no. 1, pp. 38–47, 2010.

[37] P. Breeze, *Power System Energy Storage Technologies*. Academic Press, 2018.

[38] M. Martínez, M. G. Molina, and P. E. Mercado, "Optimal sizing method of vanadium redox flow battery to provide load frequency control in power systems with intermittent renewable generation," *IET Renewable Power Generation, vol. no. 11*, no. 14, pp. 1804–1811, 2017.

[39] N. Sivakumar, D. Das, N. Padhy, A. S. Kumar, and N. Bisoyi, "Status of pumped hydro-storage schemes and its future in india," *Renewable and Sustainable Energy Reviews, vol. no. 19*, pp. 208–213, 2013.

[40] F. Faraji, A. Majazi, K. Al-Haddad *et al.*, "A comprehensive review of flywheel energy storage system technology," *Renewable and Sustainable Energy Reviews, vol. no. 67*, pp. 477–490, 2017.

[41] P. Gaur, D. Bhowmik, and N. Soren, "Utilisation of plug-in electric vehicles for frequency regulation of multi-area thermal interconnected power system," *IET Energy Systems Integration, vol. no. 1*, no. 2, pp. 88–96, 2019.

[42] J. Fang, H. Li, Y. Tang, and F. Blaabjerg, "On the inertia of future more-electronics power systems," *IEEE Journal of Emerging and Selected Topics in Power Electronics*, vol. 7, no. 4, pp. 2130–2146, 2018.

[43] V. Mallemaci, F. Mandrile, S. Rubino, A. Mazza, E. Carpaneto, and R. Bojoi, "A comprehensive comparison of virtual synchronous generators with focus on virtual inertia and frequency regulation," *Electric Power Systems Research*, vol. 201, p. 107516, 2021.

[44] B. M. Gundogdu, S. Nejad, D. T. Gladwin, M. P. Foster, and D. A. Stone, "A battery energy management strategy for uk enhanced frequency response and triad avoidance," *IEEE Transactions on Industrial Electronics*, vol. 65, no. 12, pp. 9509–9517, 2018.

[45] F. Sanchez, J. Cayenne, F. Gonzalez-Longatt, and J. L. Rueda, "Controller to enable the enhanced frequency response services from a multi-electrical energy storage system," *IET Generation, Transmission & Distribution*, vol. 13, no. 2, pp. 258–265, 2019.

[46] [Online]. Available: https://www.nationalgrid.com/sites/default/files/documents/Enhanced%20Frequency%20Response%20FAQs%20v5.0_.pdf

[47] X. Meng, J. Liu, and Z. Liu, "A generalized droop control for grid-supporting inverter based on comparison between traditional droop control and virtual synchronous generator control," *IEEE Transactions on Power Electronics*, vol. 34, no. 6, pp. 5416–5438, 2018.

[48] A. Pappachen and A. P. Fathima, "Load frequency control in deregulated power system integrated with SMES-TCPS combination using anfis controller," *International Journal of Electrical Power & Energy Systems, vol. no. 82*, pp. 519–534, 2016.

[49] D. Guha, P. K. Roy, and S. Banerjee, "Oppositional biogeography-based optimisation applied to SMES and TCSC-based load frequency control with gen-

eration rate constraints and time delay," *International Journal of Power and Energy Conversion, vol. no. 7*, no. 4, pp. 391–423, 2016.

[50] J. de Dieu Nguimfack-Ndongmo, G. Kenné, R. Kuate-Fochie, A. Cheukem, H. B. Fotsin, and F. Lamnabhi-Lagarrigue, "A simplified nonlinear controller for transient stability enhancement of multimachine power systems using SSSC device," *International Journal of Electrical Power & Energy Systems, vol. no. 54*, pp. 650–657, 2014.

[51] M. G. Jolfaei, A. M. Sharaf, S. M. Shariatmadar, and M. B. Poudeh, "A hybrid PSS-SSSC GA-stabilization scheme for damping power system small signal oscillations," *International Journal of Electrical Power & Energy Systems, vol. no. 75*, pp. 337–344, 2016.

[52] H. Shayeghi, H. Shayanfar, and A. Jalili, "LFC design of a deregulated power system with tcps using pso," *International Journal of Electrical and Electronics Engineering*, vol. 3, no. 10, pp. 632–640, 2009.

[53] J. M. Ramirez and J. L. Murillo-Perez, "Steady-state voltage stability with statcom," *IEEE Transactions on Power Systems, vol. no. 21*, no. 3, pp. 1453–1454, 2006.

[54] A. Prakash, K. Kumar, and S. K. Parida, "PIDF (1+ FOD) controller for load frequency control with SSSC and AC-DC tie-line in deregulated environment," *IET Generation, Transmission & Distribution, vol. no. 14*, no. 14, pp. 2751–2762, 2020.

[55] R. Shankar, S. Pradhan, K. Chatterjee, and R. Mandal, "A comprehensive state of the art literature survey on LFC mechanism for power system," *Renewable and Sustainable Energy Reviews*, vol. 76, pp. 1185–1207, 2017.

[56] S. K. Pandey, S. R. Mohanty, and N. Kishor, "A literature survey on load–frequency control for conventional and distribution generation power systems," *Renewable and Sustainable Energy Reviews, vol. no. 25*, pp. 318–334, 2013.

[57] S. Musunuri and G. Dehnavi, "Comparison of STATCOM, SVC, TCSC, and SSSC performance in steady state voltage stability improvement," in *North American Power Symposium 2010*. IEEE, 2010, pp. 1–7.

[58] M. A. Kamarposhti and H. Lesani, “Effects of STATCOM, TCSC, SSSC and UPFC on static voltage stability,” *Electrical Engineering, vol. no. 93*, no. 1, pp. 33–42, 2011.

[59] U. Mhaskar and A. Kulkarni, “Power oscillation damping using facts devices: modal controllability, observability in local signals, and location of transfer function zeros,” *IEEE Transactions on Power Systems, vol. no. 21*, no. 1, pp. 285–294, 2006.

[60] H. Nguyen-Duc, L.-A. Dessaint, A. F. Okou, and I. Kamwa, “A power oscillation damping control scheme based on bang-bang modulation of FACTS signals,” *IEEE Transactions on Power Systems, vol. no. 25*, no. 4, pp. 1918–1927, 2010.

[61] M. Haque, “Damping improvement by FACTS devices: A comparison between STATCOM and SSSC,” *Electric Power Systems Research, vol. no. 76*, no. 9-10, pp. 865–872, 2006.

[62] “Analysis of load frequency control in a restructured multi-area power system with the Kalman filter and the LQR controller,” *AEU - International Journal of Electronics and Communications*, vol. 86, pp. 25–46, 2018. [Online]. Available: https://www.sciencedirect.com/science/article/pii/S1434841117321210

[63] H. Bevrani, H. Golpîra, A. R. Messina, N. Hatziargyriou, F. Milano, and T. Ise, “Power system frequency control: An updated review of current solutions and new challenges,” *Electric Power Systems Research*, vol. 194, p. 107114, 2021.

[64] D. Rerkpreedapong, A. Hasanovic, and A. Feliachi, “Robust load frequency control using genetic algorithms and linear matrix inequalities,” *IEEE Transactions on Power Systems*, vol. 18, no. 2, pp. 855–861, 2003.

[65] N. Nayak, S. Mishra, D. Sharma, and B. K. Sahu, “Application of modified sine cosine algorithm to optimally design PID/fuzzy-PID controllers to deal with agc issues in deregulated power system,” *IET Generation, Transmission & Distribution, vol. no. 13*, no. 12, pp. 2474–2487, 2019.

[66] W. Tasnin and L. C. Saikia, “Maiden application of an sine–cosine algorithm optimised fo cascade controller in automatic generation control of multi-area thermal system incorporating dish-stirling solar and geothermal power plants,” *IET Renewable Power Generation, vol. no. 12*, no. 5, pp. 585–597, 2018.

[67] N. R. Babu and L. C. Saikia, "Load frequency control of a multi-area system incorporating realistic high-voltage direct current and dish-stirling solar thermal system models under deregulated scenario," *IET Renewable Power Generation, vol. no. 15*, no. 5, pp. 1116–1132, 2021.

[68] P. Dahiya, V. Sharma, and R. Naresh, "Automatic generation control using disrupted oppositional based gravitational search algorithm optimised sliding mode controller under deregulated environment," *IET Generation, Transmission & Distribution, vol. no. 10*, no. 16, pp. 3995–4005, 2016.

[69] M. Elsisi, M. Soliman, M. A. Aboelela, and W. Mansour, "Model predictive control of plug-in hybrid electric vehicles for frequency regulation in a smart grid," *IET Generation, Transmission & Distribution, vol. no. 11*, no. 16, pp. 3974–3983, 2017.

[70] A. Abazari, H. Monsef, and B. Wu, "Load frequency control by de-loaded wind farm using the optimal fuzzy-based PID droop controller," *IET Renewable Power Generation, vol. no. 13*, no. 1, pp. 180–190, 2019.

[71] A. Abou El Ela, R. A. El-Sehiemy, A. Shaheen, and A. Shalaby, "Application of the crow search algorithm for economic environmental dispatch," in *2017 Nineteenth International Middle East Power Systems Conference (MEPCON)*, 2017, pp. 78–83.

[72] A. B. Rehiara, N. Yorino, Y. Sasaki, and Y. Zoka, "A novel adaptive LFC based on mpc method," *IEEJ Transactions on Electrical and Electronic Engineering*, vol. 14, no. 8, pp. 1145–1152, 2019.

[73] P. Hota and B. Mohanty, "Automatic generation control of multi source power generation under deregulated environment," *International Journal of Electrical Power & Energy Systems*, vol. 75, pp. 205–214, 2016.

[74] E. Olle, "ELECTRIC ENERGY SYSTEMS THEORY : AN INTRODUCTION," 1971.

[75] A. Z. A. Shaqsi, K. Sopian, and A. Al-Hinai, "Review of energy storage services, applications, limitations, and benefits," *Energy Reports*, vol. 6, pp. 288–306, 2020.

[76] S. S. Abelson, M. G. Wise, and M. J. Molitor, "Method and system for controlling a reheat turbine-generator," Mar. 18 2008, us Patent 7,343,744.

[77] D. Das, J. Nanda, M. Kothari, and D. Kothari, "Automatic generation control of a hydrothermal system with new area control error considering generation rate constraint," *Electric Machines & Power Systems*, vol. 18, no. 6, pp. 461–471, 1990.

[78] A. Demiroren and E. Yesil, "Automatic generation control with fuzzy logic controllers in the power system including SMES units," *International journal of electrical power & energy systems*, vol. 26, no. 4, pp. 291–305, 2004.

[79] Y. Wang, X. Wang, Z. Chen, and F. Blaabjerg, "Small-signal stability analysis of inverter-fed power systems using component connection method," *IEEE Transactions on Smart Grid*, vol. 9, no. 5, pp. 5301–5310, 2018.

[80] N. G. Hingorani, L. Gyugyi, and M. El-Hawary, *Understanding FACTS: concepts and technology of flexible AC transmission systems*. IEEE press New York, 2000, vol. 1.

[81] J. A. Momoh, *Electric power system applications of optimization*. CRC press, 2017.

[82] R. K. Sahu, S. Panda, and P. C. Pradhan, "Design and analysis of hybrid firefly algorithm-pattern search based fuzzy PID controller for LFC of multi area power systems," *International Journal of Electrical Power & Energy Systems*, vol. 69, pp. 200–212, 2015.

[83] M. Elsisi, M. Soliman, M. A. Aboelela, and W. Mansour, "Bat inspired algorithm based optimal design of model predictive load frequency control," *International Journal of Electrical Power & Energy Systems*, vol. 83, pp. 426–433, 2016.

[84] B. Sonker, D. Kumar, and P. Samuel, "Dual loop IMC structure for load frequency control issue of multi-area multi-sources power systems," *International Journal of Electrical Power & Energy Systems*, vol. 112, pp. 476–494, 2019.

[85] P. Kumar, D. P. Kothari *et al.*, "Recent philosophies of automatic generation control strategies in power systems," *IEEE Transactions on Power Systems, vol. no. 20*, no. 1, pp. 346–357, 2005.

[86] M. Eslami, H. Shareef, M. R. Taha, and M. Khajehzadeh, "Adaptive particle swarm optimization for simultaneous design of upfc damping controllers," *International Journal of Electrical Power & Energy Systems*, vol. 57, pp. 116–128, 2014.

[87] A. Phadke, M. Fozdar, and K. Niazi, "A new multi-objective fuzzy-GA formulation for optimal placement and sizing of shunt FACTS controller," *International Journal of Electrical Power & Energy Systems*, vol. 40, no. 1, pp. 46–53, 2012.

[88] S. P. Dash, K. Subhashini, and J. Satapathy, "Optimal location and parametric settings of facts devices based on jaya blended moth flame optimization for transmission loss minimization in power systems," *Microsystem Technologies*, vol. 26, no. 5, pp. 1543–1552, 2020.

[89] A. Khazali and M. Kalantar, "Optimal reactive power dispatch based on harmony search algorithm," *International Journal of Electrical Power & Energy Systems*, vol. 33, no. 3, pp. 684–692, 2011.

[90] D. E. Goldberg, *Genetic algorithms*. Pearson Education India, 2006.

[91] H. Bevrani and T. Hiyama, *Intelligent automatic generation control*. CRC press, 2016.

[92] C. K. Shiva and V. Mukherjee, "Comparative performance assessment of a novel quasi-oppositional harmony search algorithm and internal model control method for automatic generation control of power systems," *IET Generation, Transmission & Distribution*, vol. 9, no. 11, pp. 1137–1150, 2015.

[93] B. Mohanty and P. K. Hota, "Comparative performance analysis of fruit fly optimisation algorithm for multi-area multi-source automatic generation control under deregulated environment," *IET Generation, Transmission & Distribution*, vol. 9, no. 14, pp. 1845–1855, 2015.

[94] A. Barisal, "Comparative performance analysis of teaching learning based optimization for automatic load frequency control of multi-source power systems," *International Journal of Electrical Power & Energy Systems*, vol. 66, pp. 67–77, 2015.

[95] Y. Sharma and L. C. Saikia, "Automatic generation control of a multi-area st–thermal power system using grey wolf optimizer algorithm based classical controllers," *International Journal of Electrical Power & Energy Systems*, vol. 73, pp. 853–862, 2015.

[96] S. Panda and N. K. Yegireddy, "Automatic generation control of multi-area power system using multi-objective non-dominated sorting genetic algorithm-ii," *International Journal of Electrical Power & Energy Systems*, vol. 53, pp. 54–63, 2013.

[97] G. Papazoglou and P. Biskas, "Review and comparison of genetic algorithm and particle swarm optimization in the optimal power flow problem," *Energies*, vol. 16, no. 3, p. 1152, 2023.

[98] N. Campion, H. Nami, P. R. Swisher, P. Vang Hendriksen, and M. Münster, "Techno-economic assessment of green ammonia production with different wind and solar potentials," *Renewable and Sustainable Energy Reviews*, vol. 173, p. 113057, 2023.

[99] G. A. Chown and R. C. Hartman, "Design and experience with a fuzzy logic controller for automatic generation control (AGC)," *IEEE Transactions on power systems*, vol. 13, no. 3, pp. 965–970, 1998.

[100] M. Datta, T. Senjyu, A. Yona, T. Funabashi, and C.-H. Kim, "A frequency-control approach by photovoltaic generator in a PV-diesel hybrid power system," *IEEE Transactions on Energy Conversion*, vol. 26, no. 2, pp. 559–571, 2010.

[101] S. You, G. Kou, Y. Liu, X. Zhang, Y. Cui, M. J. Till, W. Yao, and Y. Liu, "Impact of high PV penetration on the inter-area oscillations in the us eastern interconnection," *IEEE Access*, vol. 5, pp. 4361–4369, 2017.

[102] K. Vidyanandan and N. Senroy, "Improved frequency regulation in wind-PV-DG hybrid microgrid using wind turbines," in *2016 IEEE 6th International Conference on Power Systems (ICPS)*. IEEE, 2016, pp. 1–6.

[103] M. Datta, T. Senjyu, A. Yona, T. Funabashi, and C.-H. Kim, "A coordinated control method for leveling pv output power fluctuations of PV-diesel hybrid

systems connected to isolated power utility," *IEEE Transactions on Energy Conversion*, vol. 24, no. 1, pp. 153–162, 2009.

[104] M. D. Tabone and D. S. Callaway, "Modeling variability and uncertainty of photovoltaic generation: A hidden state spatial statistical approach," *IEEE Transactions on Power Systems*, vol. 30, no. 6, pp. 2965–2973, 2014.

[105] Y. Jia and C. Sun, "Distributed mpc with application to agc of power system with wind-photovoltaic hybrid generation," in *2017 36th Chinese Control Conference (CCC)*. IEEE, 2017, pp. 4676–4681.

[106] S. Sen, S. Sengupta, and A. Chakrabarti, *Electricity Pricing: Regulated, Deregulated and Smart Grid Systems*. CRC Press, 2018.

[107] E. R. S. Task Force, "Concept paper on ERS that characterize bulk power system reliability," 2014.

[108] N. R. B. Sanjeev Kumar Bhagat, Lalit Chandra Saikia and D. Saha, "Impact of PLL and virtual inertia on deregulated AGC system integrated with parallel AC/HVDC," *IETE Journal of Research*, vol. 69, no. 5, pp. 2514–2527, 2023. [Online]. Available: https://doi.org/10.1080/03772063.2021.1894249

[109] H. H. Ali, A. M. Kassem, M. Al-Dhaifallah, and A. Fathy, "Multi-verse optimizer for model predictive load frequency control of hybrid multi-interconnected plants comprising renewable energy," *IEEE Access*, vol. 8, pp. 114 623–114 642, 2020.

[110] I. C. Report, "Dynamic models for steam and hydro turbines in power system studies," *IEEE Transactions on Power Apparatus and Systems*, no. 6, pp. 1904–1915, 1973.

[111] K. Sudha and R. V. Santhi, "Robust decentralized load frequency control of interconnected power system with generation rate constraint using type-2 fuzzy approach," *International Journal of Electrical Power & Energy Systems*, vol. 33, no. 3, pp. 699–707, 2011.

[112] Littlefuse, "G4000ef450 - gate turn off thyristor - capsule type series." [Online]. Available: https://www.littelfuse.com/products/power-semiconductors/discrete-thyristors/gto-thyristors/gate-turn-off-thyristor-capsule-type/g4000ef450.aspx

[113] S.-H. Kim, "Chapter 7 - pulse width modulation inverters," in *Electric Motor Control*, S.-H. Kim, Ed. Elsevier, 2017, pp. 265–340. [Online]. Available: https://www.sciencedirect.com/science/article/pii/B9780128121382000076

[114] R. W. Erickson and D. Maksimovic, *Fundamentals of power electronics*. Springer Science & Business Media, 2007.

[115] J. Siva Prasad, T. Bhavsar, R. Ghosh, and G. Narayanan, "Vector control of three-phase ac/dc front-end converter," *Sadhana*, vol. 33, no. 5, pp. 591–613, 2008.

[116] L. Zhang, Y. Pu, M. Chen, T. Wei, and X. Peng, "Novel na0. 5bi0. 5tio3 based, lead-free energy storage ceramics with high power and energy density and excellent high-temperature stability," *Chemical Engineering Journal*, vol. 383, p. 123154, 2020.

[117] D. M. Rosewater, D. A. Copp, T. A. Nguyen, R. H. Byrne, and S. Santoso, "Battery energy storage models for optimal control," *IEEE Access*, vol. 7, pp. 178 357–178 391, 2019.

[118] C. S. Solanki, *Solar photovoltaics: fundamentals, technologies and applications*. PHI Learning Pvt. Ltd., 2015.

[119] D.-J. Lee and L. Wang, "Small-signal stability analysis of an autonomous hybrid renewable energy power generation/energy storage system part i: Time-domain simulations," *IEEE Transactions on Energy Conversion*, vol. 23, no. 1, pp. 311–320, 2008.

[120] S. Rahman, S. Saha, S. N. Islam, M. T. Arif, M. Mosadeghy, M. E. Haque, and A. M. T. Oo, "Analysis of power grid voltage stability with high penetration of solar pv systems," *IEEE Transactions on Industry Applications*, vol. 57, no. 3, pp. 2245–2257, 2021.

[121] M. Paramasivam, S. Dasgupta, V. Ajjarapu, and U. Vaidya, "Contingency analysis and identification of dynamic voltage control areas," *IEEE Transactions on Power Systems*, vol. 30, no. 6, pp. 2974–2983, 2015.

[122] A. Pillay, S. P. Karthikeyan, and D. Kothari, "Congestion management in power systems–a review," *International Journal of Electrical Power & Energy Systems*, vol. 70, pp. 83–90, 2015.

[123] L. Thurner, A. Scheidler, F. Schäfer, J. Menke, J. Dollichon, F. Meier, S. Meinecke, and M. Braun, "pandapower — an open-source python tool for convenient modeling, analysis, and optimization of electric power systems," *IEEE Transactions on Power Systems*, vol. 33, no. 6, pp. 6510–6521, Nov 2018.

[124] M. R. Narimani, H. Huang, A. Umunnakwe, Z. Mao, A. Sahu, S. Zonouz, and K. Davis, "Generalized contingency analysis based on graph theory and line outage distribution factor," *IEEE Systems Journal*, vol. 16, no. 1, pp. 626–636, 2022.

[125] H. Zhang, C. Zhai, G. Xiao, and T.-C. Pan, "Identifying critical risks of cascading failures in power systems," *IET Generation, Transmission & Distribution*, vol. 13, no. 12, pp. 2438–2445, 2019.

[126] H. Jalalat and S. Liasi, "Optimal location of voltage sags monitoring buses, based on the correlation rate between network buses with considering the probability distribution of variables," *Electrical Engineering*, vol. 105, no. 1, pp. 509–518, 2023.

[127] M. R. Zaidan and S. I. Toos, "Optimal location of static var compensator to regulate voltage in power system," *IETE Journal of Research*, vol. 69, no. 4, pp. 2177–2185, 2023.

List of Publications

Journals

1. Rachakonda SR Akshay, Rajesh Joseph Abraham "Load-frequency regulation with solar PV and battery energy storage system". International Journal of Power and Energy Systems, ACTA Press, 2019, 39(1).

2. Rachakonda SR Akshay and Rajesh J. Abraham "Load following performance in a deregulated power system with static synchronous compensator and super magnetic energy storage". Energy Systems. 2022 May 13:1-20.

Refereed Conferences

1. Akshay, Rachakonda Shri Rama, and Rajesh Joseph Abraham. "Bilateral Load Following with a STATCOM and Battery Energy Storage." 2020 IEEE International Conference on Power Electronics, Smart Grid and Renewable Energy (PESGRE2020). IEEE, 2020.

2. Akshay, Rachakonda Shri Rama, and Rajesh Joseph Abraham. "Eigen Value Analysis of AGC with Solar PV and BESS." In 2020 21st National Power Systems Conference (NPSC), pp. 1-5. IEEE, 2020.

Book Chapter

Akshay, R.S.R., Abraham, R.J. (2022). "AGC in a Deregulated Interconnected Power System with STATCOM and Energy Storage System". Lecture Notes in Electrical Engineering, vol 847. Springer, Singapore. https://doi.org/10.1007/978-981-16-9008-$2_2$6